Modelling Enhanced Gas Recovery by CO$_2$ Injection in Partially-Depleted Reservoirs.

GOUDARZI, SALIM

Modelling Enhanced Gas Recovery by CO_2 Injection in Partially-Depleted Reservoirs

by
Salim Goudarzi

A thesis submitted for the degree of
Doctor of Philosophy
in the Department of Earth Sciences
Durham University

January 31, 2017

ABSTRACT

Carbon Capture and Storage (CCS) is considered as an important potential solution for CO_2 emission reduction. Yet, the CO_2 capture process is highly costly. Thus, combining Enhanced Gas Recovery (EGR) with CCS could potentially offset the costs via additional production of natural gas. The objective of this P.hD. is to build a numerical model to simulate CO_2-EGR in partially-depleted gas reservoirs; in particular Centrica Plc's North Morecame gas field.

Our numerical model is based on the so-called Method of Lines (MOL) approach. MOL requires selecting a set of persistent Primary Dependent Variables (PDVs) to solve for. In this case, we chose to solve for pressure, temperature and component mass fractions. Additionally, MOL requires recasting of the governing equations in terms of the PDVs, which often requires the evaluation of partial derivative terms of the flow properties with respect to the PDVs. In this work, a method of analytical evaluation of these partial derivative terms is introduced. Furthermore, in a new approach, the mutual solubility correlations for mixtures of CO_2-H_2O and CH_4-H_2O, available in the literature, are joined together using straight lines as a ternary diagram, to form a ternary CO_2-CH_4-H_2O equilibrium model; the equilibrium-model's predictions matched well with the available experimental solubility data.

1D and 2D numerical simulations of CO_2-EGR were carried out. Overall, the 1D results were found to match very well with an existing analytical solution, predicting accumulation of a CH_4 bank ahead of the CO_2 plume and accurately locating the associated shock fronts while considering the partial miscibility of both CO_2 and CH_4 in H_2O. Taking into account the simulated incremental gas recovery potential, global wellhead CH_4 prices, offshore drilling costs, CO_2 supply cost and UK's Carbon Price Floor (CPF), it was concluded that, based on the current gas prices, recovery of 0.7% of the Gas Initially In Place (GIIP), equivalent to 0.22 billion standard cubic meters (BSCM), breaks even. Assuming an average CO_2 supply cost of 50 US$/tonne, by 2020, CO_2-EGR in the North Morecambe field can generate a revenue of over 13 million US$. However, if the future CO_2/CH_4 markets involve payments to operators willing to store the CO_2, an upwards shift in CH_4 prices, and/or a reduction in CO_2 supply cost due to advancements in capture technologies, etc., the economics of CO_2-EGR will improve dramatically, leading to an economically viable incremental EGR potential of 5% of the GIIP, equivalent to over 2 BSCM of CH_4 volume in this field.

CONTENTS

LIST OF FIGURES

LIST OF TABLES

DECLARATION

I declare that this thesis, presented for the degree of Doctor of Philosophy at Durham University, is the result of my own original research and has not been previously submitted to Durham University or any other institution.

Salim Goudarzi
Durham University
January 31, 2017

ACKNOWLEDGMENTS

I acknowledge the financial support from Centrica Plc.

I would like to express my gratitude to my two supervisors, Dr. Simon Mathias and Prof. Jon Gluyas for their invaluable guidance and support. Simon and Jon have provided me with insightful suggestions, many academic and self-development opportunities.

I also appreciate the support of the faculty members and staff in the Durham University Department of Earth Sciences.

I would like to thank fellow researchers/friends during my time as Ph.D. student in Durham, for help with my work and general chat about related and unrelated topics: Jack, Lena, Tore, Fran, Ayo and Charlotte.

Friends outside the section also provided encouragement and relief at the times of need. Special thanks to: Valentina, Anna, Stephan, Bansri, Ines, Gabri, Ceci, Paolo, Brunella, Juliet, Virgilio, Mickaele, Marie, Dimitris, Roberto, Christina, Blanca, Lisa, Jose, Arya, Ehsan, Albert, Nuno, Gabriella, Sim, Therese and Alex.

Last but not least, I would like to thank Mum, my three sisters and three brothers, for everything you have done for me during my studies and beyond. None of this would have been possible without your continuous love and support.

DEDICATION

To Dad.

Greek Symbols

α_b Bulk-flow compressibility. [LT^2M^{-1}]. p.21

$\bar{\psi}_k$ Cell-average value of ϕ_k. [-]. p.65

β_j Thermal expansion coefficient of phase j. [K^{-1}]. p.18

β_b Bulk-flow thermal expansion coefficient. [K^{-1}]. p.22

χ Discontinuous part of the flux function F. [-]. p.67

γ_i Activity coefficient of component i. [-]. p.139

γ_{bi} Change of bulk-flow density with mass of component i. [-]. p.22

κ_j Thermal conductivity of phase j. [$MLT^{-3}K^{-1}$]. p.17

λ_j Mobility of phase j. [MLT^{-1}]. p.15

μ_i^0 Chemical potential of component i at reference pressure, $P = P_{ref}$. [$ML^2T^{-2}N^{-1}$]. p.136

μ_i Chemical potential of component i. [$ML^2T^{-2}N^{-1}$]. p.132

μ_{ij} Chemical potential of component i in phase j. [$ML^2T^{-2}N^{-1}$]. p.134

μ_i^* Chemical potential of pure component i. [$ML^2T^{-2}N^{-1}$]. p.138

μ_j Viscosity of phase j. [$MT^{-1}L^{-1}$]. p.15

∇ Differential operator. [-]. p.13

ω Coefficient of of the temperature equation. [-]. p.22

ϕ Porosity. [-]. p.12

ϕ_i Fugacity coefficient of component i. [-]. p.137

ψ Variable of the first order system of PDEs. [-]. p.59

ψ_0 Initial condition for the system of PDEs. [-]. p.59

ρ_j Density of phase j. [ML^{-3}]. p.12

ρ_b Bulk-flow density per unit volume of rock. [ML^{-3}]. p.14

ρ_{ij} Density of component i in phase j. [ML^{-3}]. p.12

θ Power exponent for the logarithmic grid spacing. [-]. p.70

ξ Smooth part of the flux function F. [-]. p.67

Latin Symbols

$\mathbf{J}$ Jacobian matrix. [-]. p.59

$\overline{g}_i$ Molar Gibbs free energy of component i. [$\mathrm{ML}^2\mathrm{T}^{-2}\mathrm{N}^{-1}$]. p.131

$\overline{h}_i$ Molar enthalpy. [$\mathrm{ML}^2\mathrm{T}^{-2}\mathrm{N}^{-1}$]. p.135

$\overline{R}$ Molar universal gas constant. [$\mathrm{L}^2\mathrm{T}^{-2}\mathrm{K}^{-1}\mathrm{N}^{-1}$]. p.136

$\overline{s}_i$ Molar entropy. [$\mathrm{ML}^2\mathrm{T}^{-2}\mathrm{K}^{-1}\mathrm{N}^{-1}$]. p.135

a_i Activity of component i. [-]. p.139

c_{p_j} Specific heat capacity of phase j. [$\mathrm{ML}^2\mathrm{T}^{-2}\mathrm{K}^{-1}$]. p.18

dV Differential element of the control volume. [L^3]. p.12

E_j Total energy of phase j per unit volume. [$\mathrm{ML}^{-1}\mathrm{T}^{-2}$]. p.16

F Flux function of the first order system of PDEs. [-]. p.59

f_i Fugacity of component i. [$\mathrm{ML}^{-1}\mathrm{T}^{-2}$]. p.137

G Gibbs free energy. [$\mathrm{ML}^2\mathrm{T}^{-2}$]. p.131

g Gravitational constant. [LT^{-2}]. p.14

G_i Mass of component i per unit volume of rock. [ML^{-3}]. p.13

H_f Formation thickness. [L]. p.70

H_i Flux of component i. [$\mathrm{MT}^{-1}\mathrm{L}^{-2}$]. p.13

H_j Enthalpy of phase j per unit volume. [$\mathrm{ML}^{-1}\mathrm{T}^{-2}$]. p.17

h_j Enthalpy of phase j per unit mass. [$\mathrm{L}^2\mathrm{T}^{-2}$]. p.18

k Absolute permeability. [L^2]. p.15

K_i Equilibrium constant of component i. [-]. p.140

k_{r_j} Relative permeability of phase j. [-]. p.15

$k_{r_{j_0}}$ End-point relative permeability of phase j. [-]. p.15

l_k Length of the grid cell k. [L]. p.64

M_0 Mass injection rate. [MT^{-1}]. p.70

m_v Empirical constant in capillary pressure equation. [-]. p.16

N_c Number of components present. [-]. p.12

N_i Number of moles of component i. [N]. p.131

n_i Mole fraction of component i. [-]. p.137

n_j Power-law exponent of the relative permeability curve for phase j. [-]. p.15

N_p Number of phases present. [-]. p.12

N_r Number of grid cells. [-]. p.70

n_v Empirical constant in capillary pressure equation. [-]. p.16

n_{ij} Equilibrium mole fraction of component i in phase j. [-]. p.141

P Pressure. [$ML^{-1}T^{-2}$]. p.14

P_c Capillary pressure. [$ML^{-1}T^{-2}$]. p.16

P_i Partial pressure of component i. [$ML^{-1}T^{-2}$]. p.136

P_i^* Vapour pressure of the pure component i. [$ML^{-1}T^{-2}$]. p.138

P_j Phase Pressure. [$ML^{-1}T^{-2}$]. p.16

P_j Pressure of phase j. [$ML^{-1}T^{-2}$]. p.15

P_w Pressure of the wetting phase. [$ML^{-1}T^{-2}$]. p.16

P_{c_0} Empirical constant in capillary pressure equation. [$ML^{-1}T^{-2}$]. p.16

P_{nw} Pressure of the non-wetting phase. [$ML^{-1}T^{-2}$]. p.16

P_{ref} Reference pressure. [$ML^{-1}T^{-2}$]. p.136

Q Heat added to the system. [ML^2T^{-2}]. p.132

r Radial distance from the injection well. [L]. p.70

r_E Radial extent of the reservoir. [L]. p.70

r_k Distance of the cell-k's centre from a reference point. [L]. p.64

r_W Injection well-radius. [L]. p.70

S Entropy. [L^2T^{-2}]. p.132

S Surface area of the control volume. [L^2]. p.13

S^I Thermodynamic state number one. [-]. p.130

S^{II} Thermodynamic state number two. [-]. p.130

S_j Saturation of phase j. [-]. p.12

S_{j_c} Critical saturation of phase j. [-]. p.15

t Time. [T]. p.13

T_j Temperature of phase j. [K]. p.18

U Total internal energy. [ML^2T^{-2}]. p.132

U_j Phase internal energy per unit volume. [$ML^{-1}T^{-2}$]. p.16

V Control volume. [L^3]. p.12

v_i Molar volume of component i. [L^3N^{-1}]. p.136

v_j Velocity of phase j. [LT^{-1}]. p.13

v_b Bulk-flow velocity. [LT^{-1}]. p.14

X_{ij} Mass fraction of component i in phase j. [-]. p.12

z Height. [L]. p.16

z_i Overall mass fraction of component i. [-]. p.20

1

INTRODUCTION

1.1 PROBLEM STATEMENT

Atmospheric concentrations of greenhouse gases, such as carbon dioxide (CO_2) and methane (CH_4), have increased to the point that significant adverse climate changes have been attributed to anthropogenic activity (Bryant, 1997, Jepma & Munasinghe, 1998). Of all greenhouse gases, CO_2 is said to be responsible for 64% of the global warming, making it the main target for mitigation of adverse greenhouse effect (Bryant, 1997). Atmospheric concentrations of CO_2 have risen from pre-industrial levels of 280 to 370 ppm (Bryant, 1997), primarily as a consequence of fossil fuel combustion for energy production. Fossil fuels, which today provide about 85% of the world's energy (David & Herzog, 2000), are likely to remain a major component of the global energy supply for a foreseeable future, due to their availability, competitive cost, storage safety and ease of transport (Bajura, 2001, Jepma & Munasinghe, 1998). Thus, the major challenge in mitigating anthropogenic effects on climate change is reducing CO_2 emissions within the framework of the Kyoto Protocol.

1.2 POTENTIAL SOLUTION

Carbon Capture and Storage (CCS) is the injection and storage of CO_2 in geological formations and is considered as an important potential solution for CO_2 emission reduction. Although oceanic storage provides much higher storage capacity, there remain uncertainties with regard to retention time and the associated environmental impacts (Metz et al., 2005). Geological storage is therefore deemed more reliable

and realistic. The, main targets for storage are coalbeds, abandoned mines, saline aquifers and depleted oil/gas reservoirs.

Saline aquifers have the advantage of being ubiquitous across the world (Bentham & Kirby, 2005). Hydrocarbon reservoirs on the other hand, have advantages associated with better levels of characterization due to available production history data. Additionally, reduced uncertainty related to cap rock integrity is demonstrated through containment of hydrocarbon products originally deposited millions of years ago (Loizzo et al., 2010). Depleted gas reservoirs have the added benefit of having a much more compressible reservoir fluid (methane+water as opposed to oil+water) along with significantly lower abandonment pressure (less than 1 MPa (Mathias et al., 2014)). CO_2 storage capacities of natural gas reservoirs around the world have been estimated to be up to 13 times higher than that of saline aquifers of comparable sizes (Barrufet et al., 2010).

Yet, CCS requires CO_2 to be stripped off the flue gas right before it is released into the atmosphere i.e. at the power plants. Separation of CO_2 from the flue gas is highly costly and is believed to consume more than 10% of the electricity generated by the power plant (David & Herzog, 2000). Therefore, it can be understood that capture and injection of CO_2 into hydrocarbon reservoirs will be more attractive if the process can provide economic incentives in the form of additional oil/gas production (which would otherwise be deemed as unrecoverable hydrocarbons) to offset the high costs associated with carbon capture.

The process of injecting a fluid into an oil reservoir to obtain an improved, more efficient oil production is called Enhanced Oil Recovery (EOR). The implications of using CO_2 for EOR have been broadly investigated in both academia and industry (Metz et al., 2005, Quintella et al., 2010, Sweatman et al., 2011). Injection of CO_2 for Enhanced Gas Recovery (EGR) however, despite being attractive to many countries with gas reserves, has not been investigated as extensively. Indeed there are only a few EGR demonstration projects in practice until now (Martens et al., 2012, Kuhn

et al., 2012). This could be attributed to the high recovery factor of gas reservoirs by natural pressure drive and concerns about degradation of natural gas due to excessive mixing between the injected and in situ fluids (Oldenburg, 2003).

1.3 CARBON STORAGE-ENHANCED GAS RECOVERY

The idea behind Carbon Storage-Enhanced Gas Recovery (CS-EGR) is that as gas is produced, reservoir pressure will decrease to the point that production rates by natural depletion are no longer economic, even though there could still be significant amounts of gas in place. CO_2 can then be injected to enhance the gas recovery process by providing the necessary pressure support to prevent subsidence and water intrusion (in the case of volumetric reservoirs) also to sweep the CH_4 from the injection well towards the production well where it can be recovered. Furthurmore, the CO_2-CH_4 system has some interesting characteristics that makes it more favourable for CS-EGR (Oldenburg et al., 2001):

- Gravity stabilised displacements can be achieved due to the fact that the CO_2 density is up to 6 times higher than that of CH_4 at reservoir conditions.
- The higher viscosity of CO_2 results in a lower mobility ratio (of CO_2 to CH_4) which in turn leads to a more stable displacement process e.g. no viscous fingering.
- CO_2 breakthrough is delayed due to the higher solubility limit of CO_2 in reservoir water compared to that of CH_4.

Finally, it is believed that once underground, a variety of mechanism can keep the CO_2 securely stored (Metz et al., 2005):

1. Residual trapping: As CO_2 is injected into the formation, it displaces water as it moves through the porous medium. As it continues to move, it is replaced

by formation water. During this process, some of the CO_2 is left behind as disconnected (residual) droplets in the pore space which are immobile.

2. Stratigraphic/structural trapping :

   CO_2 is more buoyant than most reservoir fluids, therefore it will percolate up through the porous rock until it is trapped under the cap rock, which has already demonstrated the capability of retaining buoyant fluids for millions of years.

3. Solubility trapping:

   CO_2 is partially miscible in formation water and the resulting mixture is denser than pure brine and therefore sinks to the bottom of the formation over time, ensuring that it cannot then migrate upwards and to the surface through faults and leaks.

4. Mineral trapping:

   Over a long time, the weakly acidic mixture of water and CO_2 reacts with the minerals in the surrounding rock to form solid carbonate minerals securely and permanently stored.

1.4 ROLE OF NUMERICAL MODELLING

To date, there have been only a handful of CS and no commercial scale EGR projects worldwide, primarily due to concerns about degradation of the quality of the produced gas due to mixing with the injection fluid. As a result, our fundamental understanding of the technical and practical risks posed by CO_2 injection and uncertainties associated with CO_2+CH_4 mixture remains rudimentary (Damen et al., 2006).

Increasing reservoir pressure as a consequence of CO_2 injection, prompts deformation and mechanical stresses in the reservoir and cap rocks, which in turn cause changes in hydraulic properties and further the multiphase flow and storage behavior of the reservoir. Fault slip may occur when the reservoir pressure rises to a critical level. This could lead to CO_2 leakage to drinking water sources or even land surface which could result in catastrophic environmental consequences.

Low pore-pressures (<1MPa) characteristic of depleted reservoirs, could lead to significant Joule-Thomson cooling (JTC) when large pressure gradients are developed around the injection well. JTC is the drop in temperature that occurs during adiabatic expansion of a real gas, i.e., going from high pressure to low pressure at constant enthalpy. Of particular concern is the severe loss of injectivity that may develop due to freezing of pore fluids (e.g., brine). Furthermore, salt precipitation may occur around the injection well, where all the resident water has been evaporated by the injection gas, which could further reduce the injectivity.

In this context, it is crucial that all the relevant aspects of CS-EGR processes are taken into consideration which requires development of suitable performance assessment tools describing the behavior of the reservoir during these processes. Consequently, significant efforts have been made in developing numerical models to represent the geological reservoir.

Rutqvist & Tsang (2002) and Rutqvist et al. (2002) investigate, using TOUGH2 (a simulator for multiphase flow and transport in fractured porous media), the stress changes and potential fault slip due to CO_2 injection in saline aquifers. Khanet al. (2002) integrated VISAGE (a visual analysis tool designed for all facets of production operations) and ECLIPSE (commercial reservoir simulator) to investigate the caprock integrity of a potential carbon storage site and Ouellet et al. (2011) used this coupled code to simulate the CO_2 injection in saline aquifer at Ketzin, Germany.

Li & Li (2011) linked FLAC (an explicit finite difference program for engineering mechanics computation) to GEM (commercial reservoir simulator) to study the CO_2

enhanced coal bed methane (ECBM) recovery. Enhanced coal bed methane recovery was also studied in Connell & Detournay (2011). However, thermal responses of reservoir and caprock formations to CO_2 injection into gas reservoirs have been minimally explored (Taron et al. (2009), Rutqvist et al. (2008)).

A number of recent simulation studies have discussed the thermal effects that develop as a consequence of CO_2 injection into oil and gas reservoirs. These include heating due to compression, cooling due to expansion, heating and cooling due to dissolution and vaporization, respectively, differences in temperature associated with injection and reservoir fluids, and heating due to viscous heat dissipation (Han et al., 2010, Oldenburg, 2007, Andre et al., 2010).

Owing to the Joule-Thomson coefficient of CO_2 being larger at lower pressures, these processes are likely to be of more significance in low-pressure depleted gas reservoirs (Mathias et al., 2010). Most previous simulation works have concentrated on pressures greater than 10 MPa such as work done by Mathias et al. (2013) and Andre et al. (2010). Exceptions to these include Han et al. (2012), who considered a minimum initial pressure of 6.89 MPa, Ziabakhsh-Ganji & Kooi (2014), who assumed an initial pressure of 6 MPa Afanasyev (2013), who assumed a minimum initial pressure of 4.5 MPa, and Singh et al. (2011) and Singh et al. (2012), who considered an initial pressure of 4 MPa.

However, depleted gas reservoirs are often abandoned at pressures lower than 1 MPa and therefore, for CSEGR, it is pertinent to consider the thermal effects in the context of low pressure reservoirs. Mukhopadhyay et al. (2012) presented numerical simulations concerning CO_2 injection into a depleted gas reservoir at 0.5 MPa, however, they ignored thermal effects.

Mathias et al. (2014) developed a two-layer vertical-equilibrium model for the injection of carbon dioxide into a low-pressure porous reservoir containing methane and water. In contrast to previous two-layer vertical equilibrium models, the compressibility of all material components was fully accounted for and non-Darcy effects

were also considered using the Forchheimer equation. However, they ignored the effects of compositional change and mixing between phases which could potentially affect the temperature profile due to evaporation/dissolution cooling/heating. Thus, the objective of this article is as follows.

1.5 OBJECTIVE

This study seeks to build a numerical model capable of modelling heat transport, pressure build-up and compositional changes in a multi-component multi-phase flow system in porous media, in the context of CO_2 injection in very low-pressure partially-depleted gas reservoirs. This Ph.D. is sponsored by Centrica Plc, and aims to simulate CO_2 injection in the North Morecambe gas field located in the Irish Sea basin and to estimate the gas recovery potential associated with CS-EGR in this field.

1.6 THESIS OUTLINE

This thesis describes the numerical modelling undertaken to better understand the processes associated with injection of CO_2 into gas reservoirs for the purpose of Enhanced Gas Recovery (EGR). EGR is a complex problem that requires knowledge of porous media flow mechanisms, multiphase flow dynamics/thermodynamics and compositional effects along with a good understanding of the Computational Fluid Dynamics (CFD) theories. Within this thesis, a numerical model has been developed based on the so-called Method of Lines (MOL) approach, in which all but one dimension are discretised and the resulting set of ODEs are solved using an ode-solver of choice. The outline of the thesis is as follows:

In Chapter 2, starting with mass, momentum and energy conservation statements, we focus on deriving the governing equations of multi-component multi-phase

(MCMP) flow systems. Due to the complexity of MCMP problems and multiple variables involved, it is necessary to make a decision early-on as to which set of the variables we will solve for in our MOL framework. Various choices can be made, therefore, this chapter further discusses our choice of, what we refer to as, Primary Dependent Variables (PDVs) to solve for. Finally, as a requirement for MOL implementation, it is shown how the governing equations can be re-casted in terms of the chosen set of PDVs.

The governing equations of the MCMP problem require evaluation of the component equilibrium mass fractions in each of the phases present. Thus, Chapter 3 focuses on developing a semi-analytical ternary equilibrium-model capable of calculating the equilibrium mass fractions for the CO_2-CH_4-H_2O system.

In the MOL framework, re-casting of the equations in terms of the PDVs often involves a combination of product- chain-rule differentiation, leading to the appearance of partial derivative terms of some of the flow properties with respect to the PDVs. Consequently, Chapter 4 introduces a method of analytical differentiation for evaluation of the aforementioned partial derivative terms.

Generally, when building numerical models, it is necessary to somehow verify the numerical results e.g. by comparison to an analytical solutions if possible. To this end, Chapter 5 briefly introduces the existing Method of Characteristics (MOC) solution by Hosseini et al. (2012) for CO_2 injection into brine aquifers who extended the analytical solution of Mathias et al. (2011b), by incorporating dissolved and/or residual CH_4. This analytical solution is then used in Chapter 6 to verify our numerical model.

Chapter 6 puts everything together into a radial 1D isothermal compositional flow simulator and compares the results to the analytical solution. The model is then extended to 2D and made non-isothermal to study the effects of gravity and temperature respectively.

Chapter 7 applies the numerical model to the study CO_2-EGR in the North Morecambe gas field (located in the east Irish Sea) and provides an estimation for the EGR potential in this field.

Finally, Chapter 8 summarises and concludes the thesis as a whole.

2

GOVERNING EQUATIONS

This chapter describes the governing equations of multi-component multi-phase (MCMP) flow in porous media and the appropriate choice of persistent primary-variables to solve for. The novelty of this chapter is the choice of the persistent primary variables and recasting of the governing equations in terms of the chosen set of variables.

2.1 INTRODUCTION

Typically, the governing equations of fluid dynamics, are expressed in the form of a set of conservation statements of mass, momentum and energy. For an isolated system, or a system in equilibrium with its surroundings, conservation requires that these three fundamental quantities are neither created nor destroyed, but only redistributed or, in the case of energy and momentum, converted from one form to another (Laney, 1998).

Consider a gas mixture being injected into a porous medium containing say, water or oil. As local chemical-equilibrium[1] is established, components in the gas dissolve in the liquid and components in the liquid transfer to the gas. Both phases move under the imposed pressure gradient at flow velocities that depend (nonlinearly) on the saturations (volume fractions) of the phases and their properties (density and viscosity). As phases encounter fresh reservoir liquid or more injected gas, new mixtures form and come to equilibrium. The result is a set of component separations

[1] Will be defined rigorously in Chapter 3.

that occur during flow, with light components propagating more rapidly than heavy ones (Orr, 2007, p. 1). This chapter describes the mathematical representation of these processes and the resulting compositional changes in the form of conservation statements.

Furthermore, in developing numerical models for complex flow systems, such as Enhanced Gas Recovery (EGR), more often than not there are more than just one set of variables that one can solve for, and still be able to obtain the entire flow field; another focus of this chapter is therefore, the choice of this set of variables and how to obtain the Partial Differential Equations (PDEs) describing them, from the building blocks of the model, which are the conservation statements of mass, momentum and energy.

2.2 CONSERVATION OF MASS

Consider an arbitrary control volume V of a porous medium, bounded by the surface S. Continuity of mass requires that:

$$\begin{array}{ccccc} \textit{Rate of change} & & \textit{Net rate of} & & \textit{Net rate of} \\ \textit{of amount of} & = & \textit{flow of} & - & \textit{flow of} \\ \textit{component } i \textit{ in } V & & \textit{component } i \textit{ into } V & & \textit{component } i \textit{ out of } V \end{array}$$

Thus the amount of phase j present in a differential element of V can be defined as:

$$\phi \rho_j S_j dV \tag{2.1}$$

where ϕ [-] is the porosity which is the portion of the rock volume available to fluids, ρ_j [ML^{-3}] is the density, N_p is the number of phases present and S_j [-] is the saturation (volume fraction) of phase j such that:

$$\sum_{j=1}^{N_p} S_j = 1 \tag{2.2}$$

The amount of the i^{th} component in j^{th} phase is therefore given by:

$$\phi \rho_j X_{ij} S_j dV \tag{2.3}$$

where X_{ij} [-] is the mass fraction of component i in phase j such that:

$$\sum_{i=1}^{N_c} X_{ij} = 1 \tag{2.4}$$

where N_c is the number of components in the system. Phase densities can be calculated using the following mixing rule (Orr, 2007, p. 13):

$$\rho_j = \left(\sum_{i=1}^{N_c} \frac{X_{ij}}{\rho_{ij}} \right)^{-1} \tag{2.5}$$

where ρ_{ij} [ML^{-3}] is the density of the i^{th} component in the j^{th} phase.
The total mass of component i is therefore the summation over phases present:

$$\phi \sum_{j=1}^{N_p} \rho_j X_{ij} S_j dV \tag{2.6}$$

Integrating Eq. (2.6) gives the total amount of component i in the control volume:

$$\int_{\mathbf{V}} \phi \sum_{j=1}^{N_p} \rho_j X_{ij} S_j dV \tag{2.7}$$

Hence time rate of change of component i is :

$$\frac{d}{dt}\int_V \phi \sum_{j=1}^{N_p} \rho_j X_{ij} S_j dV \tag{2.8}$$

Neglecting molecular diffusion and hydrodynamic dispersion, change in component i can only be due to transport of materials through the surface (S) of the control volume (V). At any differential element of area (dS) the convective flux of component i in phase j through the surface is given by:

$$\rho_j X_{ij} v_j \tag{2.9}$$

where v_j [LT^{-1}] is the phase velocity and will be described in more details in the next section. The net rate of convective inflow of component i is obtained by summing the contributions for flow of each phase and integrating over the full surface, S, to obtain:

$$\int_S \sum_{j=1}^{N_p} \rho_j X_{ij} v_j dS \tag{2.10}$$

Then, the conservation of mass statement for component i in integral form, takes the form:

$$\frac{d}{dt}\int_V \phi \sum_{j=1}^{N_p} \rho_j X_{ij} S_j dV + \int_S \sum_{j=1}^{N_p} \rho_j X_{ij} v_j dS = 0 \tag{2.11}$$

and in differential form:

$$\frac{\partial G_i}{\partial t} + \nabla . H_i = 0 \qquad , \qquad i \in [1, 2, .., N_c] \tag{2.12}$$

$$G_i = \phi \sum_{j=1}^{N_p} \rho_j X_{ij} S_j \tag{2.13}$$

$$H_i = \sum_{j=1}^{N_p} \rho_j X_{ij} v_j \tag{2.14}$$

It is useful to define a bulk flow mass per unit volume of rock, ρ_b [ML^{-3}], by summing over all the components in the system:

$$\rho_b = \sum_{i=1}^{N_c} G_i = \phi \sum_{j=1}^{N_p} \rho_j S_j \tag{2.15}$$

Further, a bulk flow velocity, v_b [LT^{-1}], can be defined such that:

$$v_b = \frac{1}{\rho_b} \sum_{j=1}^{N_p} \rho_j v_j \tag{2.16}$$

By summing over the component mass conservation statements, Eq.(2.12), noting that $\sum_{i=1}^{N_c} X_{ij} = 1$, mass conservation statement of the bulk flow can be written as:

$$\frac{\partial \rho_b}{\partial t} + \nabla.(\rho_b v_b) = 0 \tag{2.17}$$

The bulk flow mass conservation statement will later be used in derivation of the energy conservation statement.

2.3 CONSERVATION OF MOMENTUM

To complete the specification of the flow problem, a number of additional functions and conditions are required. The phase velocity which is the most important part, as it controls the convective part of the flow, is yet to be determined.

Commonly, a set of balance equations for the momentum of each phase, which must also be conserved, is solved to calculate the phase velocity (Temam, 2001):

$$\frac{\partial}{\partial t}(\rho v) + \nabla.(\rho v^2) = - \overbrace{\nabla.P}^{Pressure\ losses} - \overbrace{\rho g}^{Body\ forces} \tag{2.18}$$

In porous media flow problems however, the solution of the resulting momentum conservation equations for the detailed velocity distributions within the porous medium, would be unnecessarily complex (Orr, 2007, p. 11); instead, an averaged version of the momentum equation is used. For single-phase flow, volume averaging of the momentum equation yields a form equivalent to the Darcy's law (Slattery, 1972, Hubbert, 1956), which states that the local flow velocity is proportional to the pressure gradient. Flow of more than one phase is often assumed to be similarly related to the pressure gradient (Marle, 1981), and hence, the flow velocity of a phase j is assumed to be given by Darcy's law:

$$v_j = \lambda_j \left(\frac{\partial P_j}{\partial x} + \rho_j g \right) \tag{2.19}$$

and phase mobilities are given by:

$$\lambda_j = -k \frac{k_{r_j}}{\mu_j} \tag{2.20}$$

where μ_j [$\mathrm{MT^{-1}L^{-1}}$] is the phase viscosity, P_j [$\mathrm{ML^{-1}T^{-2}}$] is the phase pressure, g [$\mathrm{LT^{-2}}$] is gravitational constant, k [$\mathrm{L^2}$] is the absolute permeability, k_{r_j} [-] is the relative permeability (fraction of the absolute permeability available to phase j) given by (Corey, 1954):

$$k_{r_j} = k_{r_{j_0}} \left(\frac{S_j - S_{j_c}}{1 - \sum_{j=1}^{N_p} S_{j_c}} \right)^{n_j} \tag{2.21}$$

where $k_{r_{j_0}}$ [-] is the end-point relative permeability, n_j power exponent and S_{j_c} [-] is the critical saturation of phase j below which k_{r_j} is zero.

As the subscript j on the pressure in the Eq. (2.19) implies, pressure is different in different phases. The relationship between the phase pressures is via capillary pressure , P_c [$\mathrm{ML^{-1}T^{-2}}$] :

$$P_{nw} - P_w = P_c \tag{2.22}$$

where P_{nw} [$\mathrm{ML^{-1}T^{-2}}$] is pressure of the non-wetting phase and P_w [$\mathrm{ML^{-1}T^{-2}}$] is the pressure of the wetting phase. The capillary pressure is assumed to be a function of the phase saturations only, and is taken to be a property of the porous medium and the fluids that can be measured in experiments. In this project the the capillary pressure function by Van Genuchten (1980) is used:

$$\left(1+\left|\frac{P_c}{P_{c_0}}\right|^{n_v}\right)^{-m_v} = \frac{S_l - S_{l_c}}{1 - S_{g_c} - S_{l_c}} \quad , \quad n_v = \frac{1}{1-m_v} \tag{2.23}$$

where subscripts g and l refer to gas and liquid phases respectively. P_{c_0} and m_v are empirical constants.

2.4 CONSERVATION OF ENERGY

Derivation of the energy conservation statement is more complicated as it requires application of some thermodynamic concepts as well as the mass and momentum conservation relations. In this section, the energy conservation statement for multi-phase multicomponent flow in porous media will be derived using the thermodynamic definition of energy, together with the mass and momentum conservation statements which were discussed in previous sections. For the sake of simplicity, here, first the energy conservation statement for fluid phase j will be derived and later the rock component will be integrated into the equation.

Total energy of phase j per unit volume, E_j [$\mathrm{ML^{-1}T^{-2}}$], of a compressible system is given by Cengel & Boles (2002)[p. , 227]:

$$E_j = \overbrace{U_j}^{Internal\ energy} + \overbrace{\frac{1}{2}\rho_j v_j^2}^{Kinetic\ energy} + \overbrace{\rho_j g z}^{Potential\ energy} \tag{2.24}$$

where U_j [$\mathrm{ML^{-1}T^{-2}}$] is the internal energy of phase j per unit volume.

However, in derivation of the Darcy's law for flow in porous media, it is often assumed that the velocity is small enough to neglect the squared velocity terms i.e. the kinetic energy (see for instance Bear, 2013, p.160). Therefore, in this case, the total energy can be reduced to:

$$E_j = U_j + \rho_j g z \tag{2.25}$$

Furthermore, Cengel & Boles (2002)[p. , 227] distinguish between the total energy of a flowing material (e.g. hydrocarbons in the system) and that of non-flowing ones (e.g. porous rock); such that the fluids entering or leaving the control volume possess an additional form of energy referred to as the flow energy, $P_j v_j$.

Thus, the conservation of energy statement for the flow in porous media (assuming heat conduction is the only external source of energy transfer) can be written as:

$$\frac{\partial E_j}{\partial t} + \nabla.(E_j v_j) + \overbrace{\nabla.(P_j v_j)}^{Flow\ energy} = \overbrace{\nabla.(\kappa_j \nabla.T_j)}^{Conduction} \tag{2.26}$$

In the following order, substituting Eq. (2.25) in Eq. (2.26), applying product rule differentiation, substituting Eq. (2.17) in Eq. (2.26), and noting that that enthalpy, H_j [$\mathrm{ML^{-1}T^{-2}}$], is defined as $H_j = U_j + P_j$, then the conservation of total energy of the bulk flow reduces to:

$$\frac{\partial U_j}{\partial t} + \nabla.(H_j v_j) = \nabla.(\kappa_j \nabla T_j) \tag{2.27}$$

Internal energy and enthalpy have units of energy per volume; units that carry much less physical information for most people than do pressure and temperature for instance. As a result, it is useful to relate these quantities to more fundamental

properties. This can be achieved through the use of the Maxwell relations (Cengel & Boles, 2002, p. 662):

$$dh_j = c_{p_j} dT_j + \frac{(1-\beta_j T_j)}{\rho_j} dP_j \tag{2.28}$$

where h_j [L^2 T^{-2}] is the enthalpy of phase j per unit mass, β_j [K^{-1}] is the thermal expansion coefficient of phase $j$and c_{p_j} [M L^2 T^{-2} K^{-1}] is the specific heat capacity of phase j.

Using product rule differentiation and noting that $H_j = \rho_j h_j$, it can then be understood that:

$$dH_j = \rho_j c_{p_j} dT_j + (1-\beta_j T_j) dP_j + h_j d\rho_j \tag{2.29}$$

$$d(H_j v_j) = \rho_j c_{p_j} v_j dT_j + v_j (1-\beta_j T_j) dP_j + h_j d(\rho_j v_j) \tag{2.30}$$

and since $U_j = H_j - P_j$:

$$dU_j = dH_j - dP_j \tag{2.31}$$

Note that the dependency of enthalpy and internal energy on the composition is tied-up in the total derivative of the density, $d\rho_j$, since density is a function of pressure, temperature and compositions. However, after substituting Eqs.(2.30) and (2.31) into Eq. (2.27), due to conservation of mass statement, Eq.(2.17), the terms that include the enthalpy h_j and $d\rho_j$, will disappear. Thus, the over all energy conservation statement for multicomponent multiphase system reduces to:

$$\rho_j C_{p_j} \frac{\partial T_j}{\partial t} - \beta_j T_j \frac{\partial P_j}{\partial t} = \nabla.(\kappa_j \nabla.T_j) + v_j(\beta_j T_j - 1)\nabla.P_j - \rho_j C_{p_j} v_j \nabla.T_j \tag{2.32}$$

Summing Eq.(2.32) over the fluid phase and the solid rock phase, assuming that the fluids and the rock are in thermal and pressure equilibrium, i.e., $T_j = T_r = T$ and $P_j = P_r = P$, and noting that the rock is static, i.e., $v_r = 0$, leads to:

$$(\rho C_p)_e \frac{\partial T}{\partial t} - \beta_e T \frac{\partial P}{\partial t} = R_e \tag{2.33}$$

where:

$$R_e = \nabla.(\kappa_e \nabla.T) + \sum_{j=1}^{N_p} \left[v_j (\beta_j T - 1) \nabla.P - \rho_j C_{p_j} v_j \nabla.T \right] \tag{2.34}$$

$$\beta_e = (1-\phi)\beta_r + \phi \sum_{j=1}^{N_p} \beta_j S_j \tag{2.35}$$

$$(\rho C_p)_e = (1-\phi)\rho_r C_{p_r} + \phi \sum_{j=1}^{N_p} \rho_j S_j c_{p_j} \tag{2.36}$$

Recall that N_p is the number of fluid phases and subscript r denotes the rock properties.

2.5 CHOICE OF PRIMARY DEPENDANT VARIABLES (PDVS)

Often when dealing with partial differential equations, it is useful to distinguish between dependent and independent variables (Stroud & Booth, 2007, p. 122). In this case, time and space are independent variables. All other variables are dependent variables.

Consider N_c [-] components residing in N_p [-] phases. The problem will be defined by N_c [-] mass conservation equations. However, considering the various values of S_j [-] and X_{ij} [-], it can be understood that there will be at least $(N_c + 1) \times N_p$ dependent variables. It is therefore necessary to choose N_c [-] dependent variables to solve for, for the mathematical problem to be well-posed.

Special care should be taken to ensure that the selected dependent variables are persistent (Amaziane et al., 2012, Bourgeat et al., 2013). This selected set of dependent variables are hereafter referred to as the primary dependent variables (PDVs).

An appropriate choice of PDVs to solve for, are temperature, T [K], and global fluid pressure, P [$\mathrm{ML^{-1}T^{-2}}$] , defined in this case by (Chen et al., 2006):

$$P = \sum_{j=1}^{N_p} S_j P_j \tag{2.37}$$

and the overall mass fraction of each component, z_i [-] , defined by:

$$z_i = G_i \Big/ \sum_{i=1}^{N_c} G_i = \frac{G_i}{\rho_b} \tag{2.38}$$

Such that:

$$\sum_{i=1}^{N_c} z_i = 1 \tag{2.39}$$

In some previous studies, the mass of each component per volume of rock, G_i [M $\mathrm{L^{-3}}$], have also proven effective as PDVs in this context (Amaziane et al., 2012, Bourgeat et al., 2013). However, an advantage of using z_i (for $i = 1, 2, \ldots N_c - 1$) as PDVs (as opposed to say G_i) is that z_i are independent of P and T; because for a given volume of fluid mixture, the mass fractions of each component, z_i, will not change with pressure and temperature, making the selected set of PDVs truly independent of one another. However, the associated mass of each component per volume of rock, G_i, may change with pressure and temperature, depending on how the individual component mass densities, ρ_{ij} [M $\mathrm{L^{-3}}$] (density of component i in phase j), vary with P and T. Furthermore, z_i are the variables used in the phase diagram (discussed further in Chapter 3), which determine the equilibrium properties of the multicomponent fluid mixture.

2.6 RECASTING OF THE EQUATIONS IN TERMS OF PDVS

Since PDVs are the variables of choice to solve for, we need to obtain the Partial Differential Equations (PDEs) that give the time rate of change of these PDVs. This section will describe how this can be achieved.

Using quotient rule, differentiating Eq. (2.38) with respect to time leads to:

$$\frac{\partial z_i}{\partial t} = \frac{1}{\rho_b}\left(\frac{\partial G_i}{\partial t} - z_i \frac{\partial \rho_b}{\partial t}\right) \tag{2.40}$$

where $\frac{\partial G_i}{\partial t}$ and $\frac{\partial \rho_b}{\partial t}$ are given by Eqs.(2.12) and (2.17) respectively.

Because of the chosen set of PDVs, for N_c number of components, ρ_b [M L^{-3}] (or any other variable that is not a PDV) is only a function of pressure, temperature, and $N_c - 1$ of the mass fractions (this is because $\sum_{i=1}^{N_c} z_i = 1$). Therefore, it can be said that:

$$\rho_b = f(P,\ T,\ z_1, ..., z_{N_c-1}) \tag{2.41}$$

Application of the chain-rule differentiation to Eq. (2.41) yields:

$$\frac{d\rho_b}{\rho_b} = \alpha_b dP - \beta_b dT + \sum_{i=1}^{N_c-1} \gamma_{bi} dz_i \tag{2.42}$$

where α_b[LT^{2}M^{-1}] is the change of bulk density with pressure i.e. bulk compressibility:

$$\alpha_b = \frac{1}{\rho_b}\frac{\partial \rho_b}{\partial P} \tag{2.43}$$

β_b[K^{-1}] is the change of bulk density with temperature i.e. bulk thermal expansion coefficient:

$$\beta_b = -\frac{1}{\rho_b}\frac{\partial \rho_b}{\partial T} \tag{2.44}$$

and γ_{bi}[-] is the change of bulk density with mass of component i:

$$\gamma_{bi} = \frac{1}{\rho_b}\frac{\partial \rho_b}{\partial z_i} \tag{2.45}$$

Eqs. (2.32) and (2.42) provide the two equations sufficient to obtain the two remaining unknowns $\frac{\partial P}{\partial t}$ and $\frac{\partial T}{\partial t}$. It follows that:

$$\frac{\partial P}{\partial t} = \frac{1}{\alpha_b}\left(\frac{1}{\rho_b}\frac{\partial \rho_b}{\partial t} - \sum_{i=1}^{N_c-1}\gamma_{bi}\frac{\partial z_i}{\partial t} + \beta_b\frac{\partial T}{\partial t}\right) \tag{2.46}$$

$$\frac{\partial T}{\partial t} = \frac{1}{\omega}\left(\frac{1}{\rho_b}\frac{\partial \rho_b}{\partial t} - \sum_{i=1}^{N_c-1}\gamma_{bi}\frac{\partial z_i}{\partial t} + \frac{\alpha_b R_e}{\beta_e T}\right) \tag{2.47}$$

where:

$$\omega = \frac{\alpha_b(\rho C_p)_e}{\beta_e T} - \beta_b \tag{2.48}$$

Thus, Eqs. (2.40), (2.46) and (2.47) are the system of PDE that describe the dynamics and thermal behavior of the system casted in terms of PDVs.

The remaining challenge is the derivation and application of formulae for the relationships defining α_b, β_b and γ_{bi}, which will be described in Chapter 4. Before that, the description of fluid phase equilibrium and how to evaluate the X_{ij} terms is required, which will be addressed first in Chapter 3.

3

TERNARY PHASE EQUILIBRIUM

This chapter describes a novel approach to developing a ternary phase equilibrium model, by joining together the two existing binary mixture models of CO_2-H_2O and CH_4-H_2O, proposed by Spycher et al. (2003) and Duan & Mao (2006) respectively, to form a ternary CO_2-CH_4-H_2O equilibrium model. For more information on the thermodynamics of phase equilibrium and the derivation of the binary models of Spycher et al. (2003) and Duan & Mao (2006), refer to Chapter 9 - Appendix(1).

3.1 INTRODUCTION

In multicomponent fluid systems, such as those encountered in petroleum production and carbon sequestration, for a given pressure and temperature, there exists an equilibrium composition for each component, that defines the maximum concentration of each component and controls the appearance/disappearance of a multiphase state. Consequently, in the study of multicomponent systems, concentration threshold values are often required, and typically obtained using thermodynamic principles.

Thermodynamically, the state of a mixture of N_c number of components is known, for a given set of overall component mass fractions, z_i [-] (such that $\sum_{i=1}^{N_c} z_i = 1$), pressure, P [$ML^{-1}T^{-2}$] and temperature, T [K] (Cengel & Boles, 2002, p. 794). Difficulties may arise if at the given P and T the mixture partitions into N_p number of phases, as each phase will then have a separate set of mass fractions different from the overall mixture mass fractions, which may need to be determined. This gives rise to the so-called “flash calculation" problem (Orr, 2007, p. 31). Consider

for instance, a two-phase mixture consisting of a gas-phase of volume fraction, S_g [-], and gas-phase mass fractions, x_{ig} [-], and a liquid-phase of volume fraction, S_l [-], and liquid-phase mass fractions, x_{il} [-], such that $\sum_{j=1}^{N_P} S_j = 1$ and $\sum_{i=1}^{N_c} x_{ij} = 1$. The purpose of flash calculation is therefore, to obtain the mass fraction of component i in phase j, x_{ij}, at the given P and T.

Although in the case of a binary mixture, x_{ij} values are independent of the overall mixture mass fractions, z_i, and only vary with P and T. However, in ternary mixtures (or any mixture involving more than two components), the problem becomes much more challenging, because equilibrium mass fractions, x_{ij}, will vary with z_i in addition to P and T. Consequently, x_{ij} values must be determined using an iterative flash-calculation for each composition, P and T combination. The need for iterative flash-calculators is explained as follows. Conventional flash-calculation procedures typically employ the concept of Gibbs free energy. Gibbs free energy, G [M L^2 T^{-2}], has units of Joules and is a thermodynamic potential. The molar Gibbs free energy is often referred to as chemical potential and symbolised by μ [$\mathrm{ML}^2\mathrm{T}^{-2}\mathrm{N}^{-1}$]. Equilibrium mass fractions are commonly obtained by setting the chemical potential of the present phases to be equal to one another, which must be true if the phases are to be in equilibrium (Cengel & Boles, 2002, p. 810). This often results in a set of highly nonlinear equations (owing to nonlinearity of the Equation of State (EOS) being used to couple the mixture composition to PVT data) to be solved simultaneously and in an iterative fashion, while extra care must be taken to avoid converging to non-physical roots. Such a procedure can impose a significant computational burden when implemented into an already computationally intensive fluid flow/transport model (Spycher et al., 2003), such as those used in reservoir simulators.

In some special cases of multicomponent systems however, it is possible to eliminate the need for iterations. To be able to describe those system, it is useful to

introduce the concept of "equilibrium ratio". For a two-phase gas(g)-liquid(l) system, let R_i be the equilibrium ratio for component i, defined as:

$$R_i = \frac{x_{ig}}{x_{il}} \tag{3.1}$$

note that the R_i values are generally not constant and vary with composition (at a given P and T). However, in some multicomponent systems, such as hydrocarbon systems, the R_i values are only weakly dependent on composition and therefore it is often reasonable to assume that all the equilibrium ratios are constant with composition (Orr, 2007, p. 38). Such an assumption is often referred to as the "constant equilibrium" assumption. Indeed, many researchers have made use of the constant equilibrium assumption for multicomponent systems, such as Juanes (2008,b), Li et al. (2012), Yan & Stenby (2014a), Yan et al. (2014b) and references therein. The advantage is that once the R_i values have been determined for a given P and T, the associated x_{ij} values can be determined non-iteratively for any composition using a set of simple quadratic equations (Juanes , 2008).

However, a problem with the constant equilibrium assumption is as follows. Consider for instance, the schematic of ternary system CH_4-CO_2-H_2O shown in Fig. 1, which has applications in areas such as petroleum production, ground water management and carbon sequestration. Writing out Eq. (3.1) on the bounding tie-lines of the two-phase region (where the mixture is in binary form) to obtain the equilibrium ratio for the H_2O component. On the bounding tie-line connecting CO_2 to H_2O:

$$R_{H_2O} = \frac{1-\tilde{x}_{CO_2(g)}}{1-\tilde{x}_{CO_2(l)}} \tag{3.2}$$

and on the bounding tie-line connecting CH_4 to H_2O:

$$R_{H_2O} = \frac{1-\tilde{x}_{CH_4(g)}}{1-\tilde{x}_{CH_4(l)}} \tag{3.3}$$

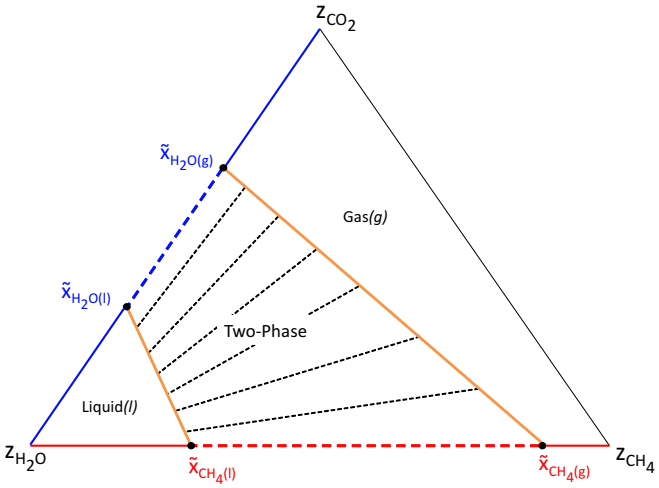

Figure 1: Schematic of the ternary CH_4-CO_2-H_2O phase diagram, at a given pressure and temperature, constructed from two binary mixture models, CH_4-H_2O and CO_2-H_2O (red and blue lines respectively), by connecting the two models using straight lines (orange lines) and linearly interpolate on these lines to obtain equilibrium mass fractions for the ternary system. Straight-line characteristic of the two phase region is a common assumption for hydrocarbon systems. Tie-Lines are shown as dashed lines. The barycentric coordinates of points of the ternary diagram correspond to the overall mass fractions, z_i [-], of the fluid mixture.

It can be seen that, when moving between the bounding tie-lines, R_{H_2O} is not constant and in fact it varies according to:

$$R_{H_2O} = \frac{1 - x_{CH_4(g)} - x_{CO_2(g)}}{1 - x_{CH_4(l)} - x_{CO_2(l)}} \tag{3.4}$$

where the x_{ij} [-] term (without the tilda) denotes the mass fraction of component i in phase j in the ternary system (as opposed to $\tilde{x}_{ij}$ which denotes the mass fraction of component i in phase j of binary mixtures, forming the bounding tie-lines). Therefore, only $N_c - 1$ number of R_i values can be constant for a given system.

Realising the above, Goudarzi et al. (2016) built a non-iterative method, which involves assuming that only R_{CO_2} and R_{CH_4} are held constant. The advantage of such an approach is that the straight bounding lines of the two-phase region on the Ternary diagram, still enables a non-iterative expression for x_{ij} to be developed, in a similar way to as proposed by Juanes (2008). But at the same time, it is possible to

honour EOSs for the CO_2-H_2O and CH_4-H_2O binary mixtures (as will be shown in the next section of this article).

The objective of this chapter is therefore, to evaluate the aforementioned proposed non-iterative method by comparing the model predictions to relevant experimental data for a CH_4-CO_2-H_2O system, previously published by Qin et al. (2008).

3.2 METHODOLOGY

Consider once again Figure 1. Here we take the equilibrium ratios, R_{CO_2} and R_{CH_4}, to be constant and the R_{H_2O} ratio to found from Eq. (3.4). In this case, the two-phase region, for a given temperature and pressure, is defined by two straight lines on a ternary diagram. Using the work of Juanes (2008), it can then be shown that values of x_{ij} for the ternary system can be related back to values obtained from the binary mixtures, $\tilde{x}_{ij}$, by the set of linear equations:

$$x_{CO_2(j)} = A\tilde{x}_{CO_2(j)} \quad \text{and} \quad x_{CH_4(j)} = (1-A)\tilde{x}_{CH_4(j)} \tag{3.5}$$

where $\tilde{x}_{CO_2(j)} = x_{CO_2(j)}$ when $z_{CH_4} = 0$, $\tilde{x}_{CH_4(j)} = x_{CH_4(j)}$ when $z_{CO_2} = 0$. z_i [-] are the overall component mass fractions, and A [-] is a weighting parameter that linearly interpolates between the bounding tie-lines that coincide with the z_{CH_4} and z_{H_2O} axes of the ternary diagram. Writing out Eq. (3.5) for components CO_2 and CH_4 and eliminating A leads to:

$$\tilde{x}_{ig}x_{il} = \tilde{x}_{il}x_{ig} \quad \text{and} \quad x_{CH_4(j)} = (\tilde{x}_{CO_2(j)} - x_{CO_2(j)})\frac{\tilde{x}_{CH_4(j)}}{\tilde{x}_{CO_2(j)}} \tag{3.6}$$

Similarly, it can be said that, on a given tie-line in the two-phase region:

$$z_i = Bx_{ig} + (1-B)x_{il} \tag{3.7}$$

where B [-] is a weighting parameter that linearly interpolates on tie-lines in the two-phase region of the ternary diagram. Writing out Eq. (3.7) for CO_2 and CH_4 and then eliminating B leads to:

$$(z_{CO_2} - x_{CO_2(l)})(x_{CH_4(g)} - x_{CH_4(l)}) = (z_{CH_4} - x_{CH_4(l)})(x_{CO_2(g)} - x_{CO_2(l)}) \tag{3.8}$$

Using Eq. (3.6) to eliminate the x_{il} and $x_{CH_4(j)}$ terms yields the quadratic equation:

$$T_2 x_{CO_2(g)}^2 + T_1 x_{CO_2(g)} + T_0 = 0 \tag{3.9}$$

where:

$$T_0 = (\tilde{x}_{CH_4(g)} - \tilde{x}_{CH_4(l)})\tilde{x}_{CO_2(g)} z_{CO_2} \tag{3.10}$$

$$T_1 = (\tilde{x}_{CO_2(g)} - \tilde{x}_{CO_2(l)})(\tilde{x}_{CH_4(l)} - z_{CH_4}) - (\tilde{x}_{CH_4(g)} - \tilde{x}_{CH_4(l)})(\tilde{x}_{CO_2(l)} + z_{CO_2}) \tag{3.11}$$

$$T_2 = (\tilde{x}_{CO_2(l)}\tilde{x}_{CH_4(g)} - \tilde{x}_{CO_2(g)}\tilde{x}_{CH_4(l)})/\tilde{x}_{CO_2(g)} \tag{3.12}$$

which has the solutions:

$$x_{CO_2(g)} = \frac{-T_1 \pm \sqrt{T_1^2 - 4T_0T_2}}{2T_2} \tag{3.13}$$

Only the solution with the $-$ sign is applicable as the other solution produces mass fractions greater than one or smaller than zero, which are unphysical. Eq. (3.13) provides an explicit expression for $x_{CO_2(g)}$ with respect to z_{CO_2} and z_{CH_4}. From Eqs. (3.5) the rest of the equilibrium mass fractions can be calculated.

Qin et al. (2008) reported some experimental measurements on vapour-liquid equilibrium in the CO_2-CH_4-H_2O ternary system at temperatures of 51 ^oC and 101 ^oC and pressures from 10 MPa to 50 MPa. Figures 2 and 3 show the comparison of the numerical phase equilibrium calculation, using the method described in the previous section, to the experimental data.

There is generally a good agreement between the two sets of values, in particular, for the mass fractions in the gas phase, x_{ig}. There is a some deviation in the results of x_{il} values, but considering the magnitude of the mass fractions (order of 10^{-2}), this should be acceptable for looking at the enhanced gas recovery problem of concern to this thesis.

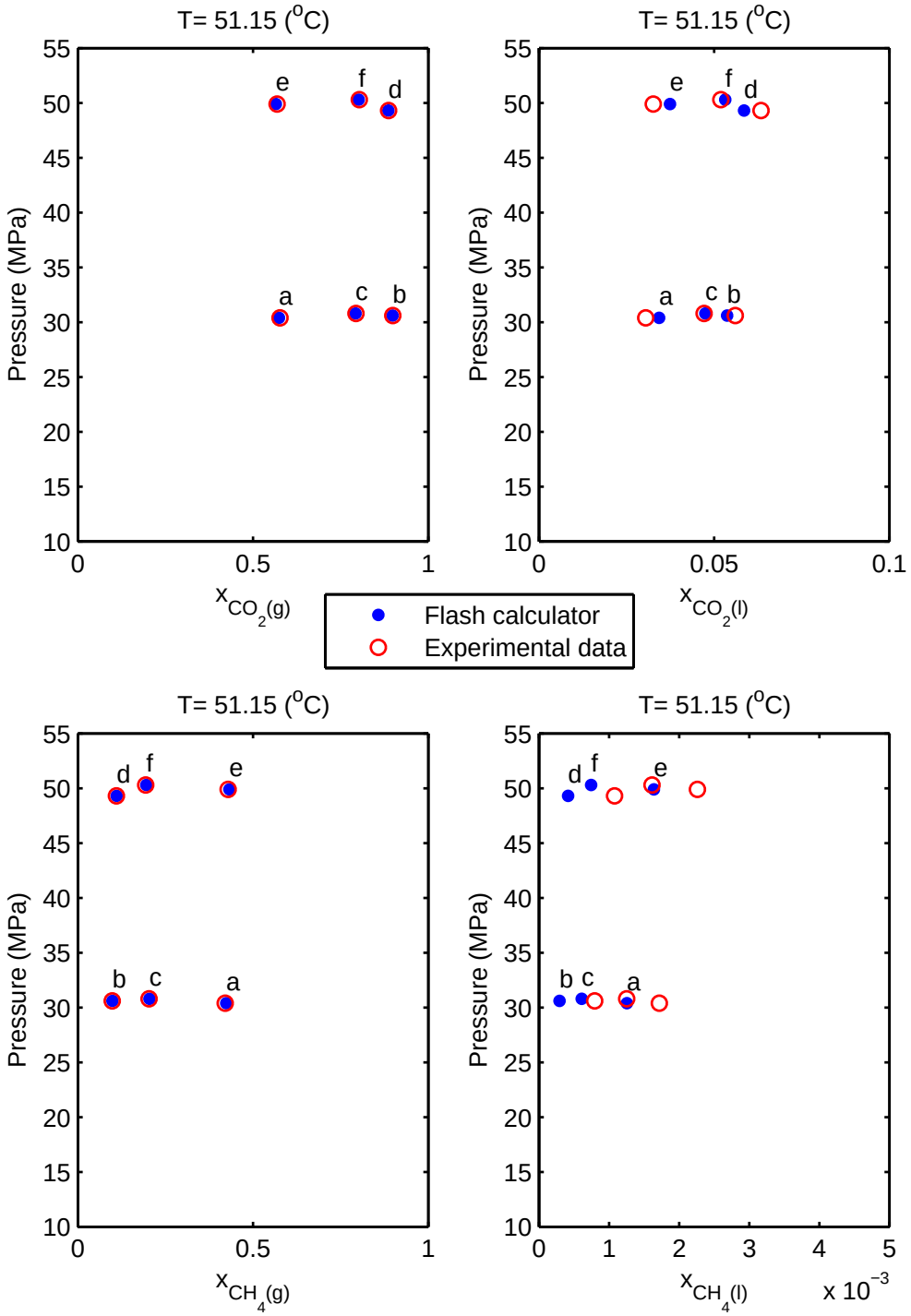

Figure 2: Comparison of the equilibrium mass fractions between the experimental measurements and numerical flash calculation for the specified pressure and T=51 (^{o}C). Mixture compositions for each point, in the form of (z_{CO_2}(%) , z_{CH_4}(%)), are as follows: a(35%, 25%), b(62%, 7%), c(52%, 13%), d(61%, 7%), e(34%, 25%), f(53%, 13%)

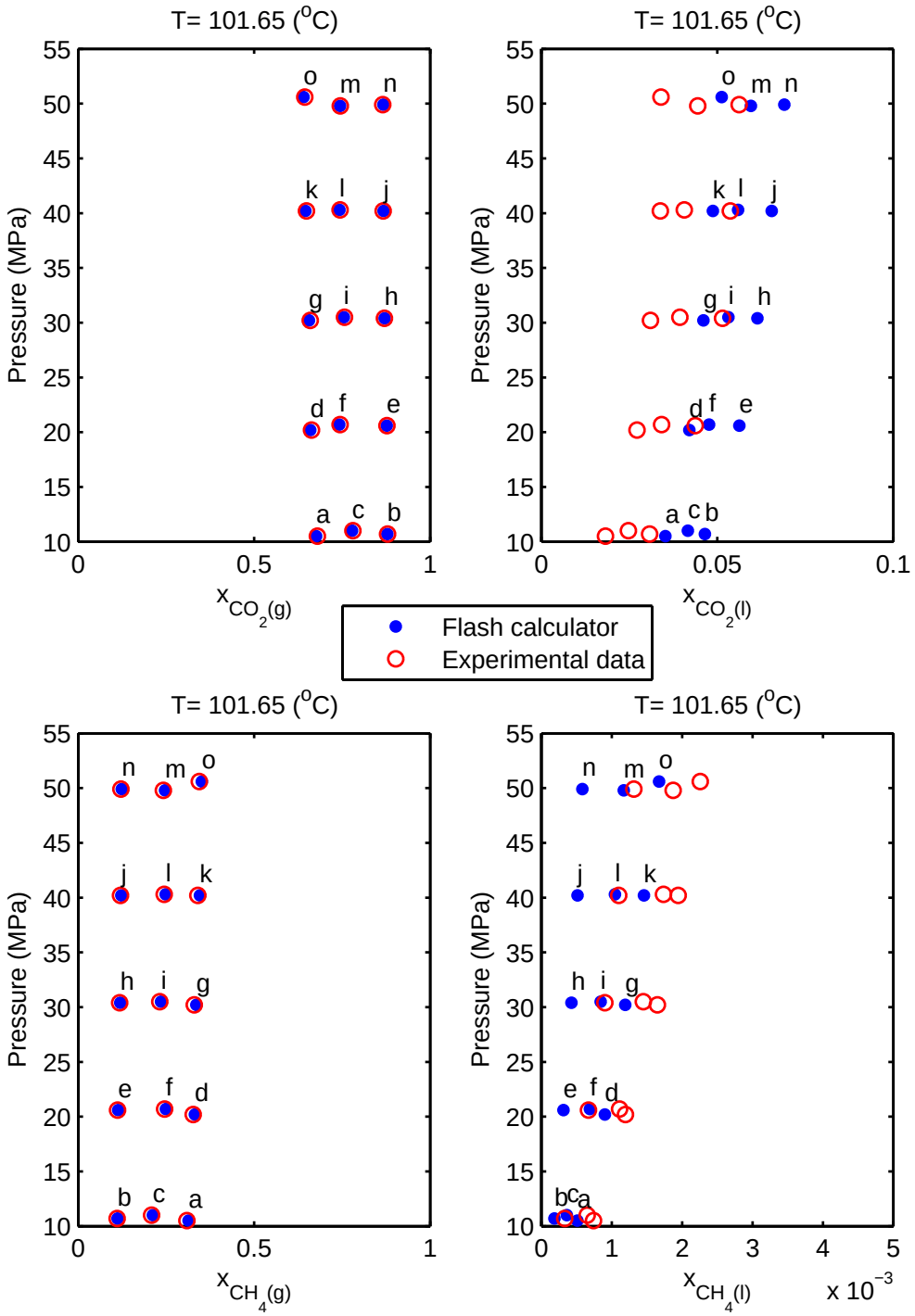

Figure 3: Comparison of the equilibrium mass fractions between the experimental measurements and numerical flash calculation for the specified pressure and T=101 (^{o}C). Mixture compositions for each point, in the form of (z_{CO_2}(%) , z_{CH_4}(%)), are as follows: a(42%, 19%), b(60%, 8%), c(50%, 13%), d(41%, 20%), e(60%, 7%), f(48%, 15%), g(41%, 20%), h(59%, 8%), i(49%, 15%), j(59%, 8%), k(40%, 21%), l(48%, 15%), m(48%, 15%), n(59%, 8%), o(40%, 21%)

4

ANALYTICAL DIFFERENTIATION

In a novel approach, this chapter introduces a method of analytical differentiation for evaluation of the partial derivatives terms of the flow properties with respect to the primary variables, in a three-component two-phase flow system.

4.1 INTRODUCTION

In Chapter 2, we first derived the governing equations of multicomponent multiphase (MCMP) flow in porous media. Then we discussed the choice of Primary Dependent Variables (PDVs) to solve for and derived the Partial Differential Equations (PDEs) describing the time rate of change of these PDVs.

When using an Ordinary Differential Equation (ODE) solver and the Method of Lines (MOL) (will be discussed in detail in Chapter 6) to solve for the aforementioned PDVs, the user must construct an ODE function. Within this function, a vector of time values is provided as an input along with an associated vector of the PDVs. The user must define the ODE function such that it calculates the derivatives of the PDVs with respect to time, which generally involves using a combination of the chain rule and the product rule for differentiation.

In our case, this results in the need to evaluate the partial derivatives of the bulk fluid mass per unit volume of rock, ρ_b, with respect to each of the PDVs, as was shown in Section 2.6. For conventional first-order time-stepping, it is arguably acceptable to evaluate these derivatives using first or second order finite differencing. However, given the high accuracy associated with the use of MATLAB's ODE solvers

(our solver of choice), it is pertinent to obtain these derivatives as accurately as possible.

There are some detailed works concerning applications of the MOL for immiscible two-phase flow and two-component two-phase flow problems (e.g. Amaziane et al., 2012, Vohralik, 2013, Bourgeat et al., 2013). Mallison et al. (2005) present a numerical simulation of an MCMP problem using the MOL in conjunction with a 3rd and 4th order Runge-Kutta time integration method. However, Mallison et al. (2005) provides no discussion concerning the casting of equations in terms of PDVs.

Indeed, little information is available as to how to obtain exact equations describing the necessary partial derivatives, $\partial\rho_b/\partial z_i$, $\partial\rho_b/\partial P$ and $\partial\rho_b/\partial T$ (Eqs. (2.43), (2.44) and (2.45) respectively), needed to solve MCMP problems for situations concerning more than two components.

This chapter focuses on obtaining such expressions for three-component and two-phase problem, making use of the semi-closed form expressions derived for the equilibrium mass fractions, x_{ij}, discussed in Section 2.5.

A version of this chapter is presented in the following article:

Goudarzi S., Mathias S.A. & Gluyas J.G. (2016). Simulation of three-component two-phase flow in porous media using method of lines. Transport in Porous Media, 112(1), 1-19.

4.2 DERIVATIVE OF BULK FLOW DENSITY

Considering the identity in Eq. (2.15), the total derivative of ρ_b (mass of fluid per unit volume of rock) can be written as:

$$d\rho_b = \rho_b \frac{d\phi}{\phi} + \phi \sum_{j=1}^{N_p} S_j \rho_j \left(\frac{d\rho_j}{\rho_j} + \frac{dS_j}{S_j} \right) \tag{4.1}$$

For two phase flow, where gas (g) and liquid (l) are the only phases such that $S_l = 1 - S_g$. From Eqs. (2.13), (2.38) and (2.15), it can then be understood that:

$$S_g = \left[1 - \frac{\rho_g(z_i - X_{ig})}{\rho_l(z_i - X_{il})}\right]^{-1} \quad , \quad S_l = \left[1 - \frac{\rho_l(z_i - X_{il})}{\rho_g(z_i - X_{ig})}\right]^{-1} \tag{4.2}$$

which on differentiation leads to:

$$\frac{dS_j}{S_g S_l} = \sum_{j=1}^{2} (-1)^j \left[\frac{d\rho_j}{\rho_j} + \left(\frac{dz_i - dX_{ij}}{z_i - X_{ij}}\right)\right] \tag{4.3}$$

Invoking Eq. (2.5), it can also be shown that:

$$\frac{d\rho_j}{\rho_j} = \rho_j \sum_{i=1}^{N_c} \frac{X_{ij}}{\rho_{ij}} \left(\frac{d\rho_{ij}}{\rho_{ij}} - \frac{dX_{ij}}{X_{ij}}\right) \tag{4.4}$$

It is now assumed that component densities are unaffected by composition such that $\partial \rho_{ij} / \partial z_i = 0$. Additionally noting that:

$$\frac{\partial z_i}{\partial z_k} = 0, \quad i \neq k \tag{4.5}$$

This is because of the way the PDVs were chosen in Section 2.5 i.e. PDVs are independent of each other and only vary with space and time.

The remaining challenge is to define the dX_{ij} terms. The terms X_{ij} can be further defined by:

$$X_{ij} = \begin{cases} z_i, & S_g = 0, 1 \\ \\ x_{ij}, & 0 < S_g < 1 \end{cases} \tag{4.6}$$

where x_{ij} [-] are the equilibrium mass fractions of the i^{th} component in the j^{th} phase within the two-phase region and were discussed in previous chapter. Then dX_{ij} is then given by:

$$\frac{\partial X_{ij}}{\partial P} = \begin{cases} 0, & S_g = 0, 1 \\ \\ \dfrac{\partial x_{ij}}{\partial P}, & 0 < S_g < 1 \end{cases} \tag{4.7}$$

$$\frac{\partial X_{ij}}{\partial T} = \begin{cases} 0, & S_g = 0, 1 \\ \\ \dfrac{\partial x_{ij}}{\partial T}, & 0 < S_g < 1 \end{cases} \tag{4.8}$$

$$\frac{\partial X_{ij}}{\partial z_i} = \begin{cases} 1, & S_g = 0, 1 \\ \\ \dfrac{\partial x_{ij}}{\partial z_i}, & 0 < S_g < 1 \end{cases} \tag{4.9}$$

It is important to note that for two-component two-phase problems, x_{ij} only varies with pressure and temperature. However, for three component two phase systems, the problem is much more complicated because the equilibrium values, x_{ij}, are no longer constant with composition (i.e. z_{CO_2} and z_{CH_4}).
Furthermore, from Eq. (3.9) we have the total derivative of $x_{CO_2(g)}$:

$$dx_{CO_2(g)} = -\frac{x^2_{CO_2(g)} dT_2 + x_{CO_2(g)} dT_1 + dT_0}{2T_2 x_{CO_2(g)} + T_1} \tag{4.10}$$

where:

$$dT_0 = (d\tilde{x}_{CH_4(g)} - d\tilde{x}_{CH_4(l)})\tilde{x}_{CO_2(g)} z_{CO_2} + (\tilde{x}_{CH_4(g)} - \tilde{x}_{CH_4(l)})(\tilde{x}_{CO_2(g)} dz_{CO_2} + d\tilde{x}_{CO_2(g)} z_{CO_2}) \tag{4.11}$$

$$dT_1 = (d\tilde{x}_{CO_2(g)} - d\tilde{x}_{CO_2(l)})(\tilde{x}_{CH_4(l)} - z_{CH_4}) + (\tilde{x}_{CO_2(g)} - \tilde{x}_{CO_2(l)})(d\tilde{x}_{CH_4(l)} - dz_{CH_4})$$

$$-(d\tilde{x}_{CH_4(g)} - d\tilde{x}_{CH_4(l)})(\tilde{x}_{CO_2(l)} + z_{CO_2}) - (\tilde{x}_{CH_4(g)} - \tilde{x}_{CH_4(l)})(d\tilde{x}_{CO_2(l)} + dz_{CO_2}) \quad (4.12)$$

$$dT_2 = d\tilde{x}_{CO_2(l)} \frac{\tilde{x}_{CH_4(g)}}{\tilde{x}_{CO_2(g)}} + d\tilde{x}_{CH_4(g)} \frac{\tilde{x}_{CO_2(l)}}{\tilde{x}_{CO_2(g)}} - d\tilde{x}_{CO_2(g)} \frac{\tilde{x}_{CO_2(l)}\tilde{x}_{CH_4(g)}}{\tilde{x}^2_{CO_2(g)}} - d\tilde{x}_{CH_4(l)} \quad (4.13)$$

which, in conjunction with Eq. (3.6), provides expressions for all the other derivatives, dx_{ij}. Now we only need expressions for $d\tilde{x}_{ij}$ terms.

$\tilde{x}_{ij}$ terms are the binary mixture mass fractions which were calculated in the previous chapter. For binary mixtures, the equilibrium mass fractions are independent of composition, therefore it can be said that:

$$\tilde{x}_{ij} = f(P,\ T) \quad (4.14)$$

To obtain the total derivative $d\tilde{x}_{ij}$, we calculate the $\tilde{x}_{ij}$ terms at a range of pressures and temperatures and use the following finite-difference stencil (note that the chosen range of pressures and temperatures are discretised on an finely-spaced grid of values to ensure accuracy of the finite difference approximations):

$$d\tilde{x}_{ij}|_k = \left.\frac{\partial \tilde{x}_{ij}}{\partial P}\right|_k dP + \left.\frac{\partial \tilde{x}_{ij}}{\partial T}\right|_k dT \quad (4.15)$$

where:

$$\left.\frac{\partial \tilde{x}_{ij}}{\partial P}\right|_k = \frac{\tilde{x}_{ij(k+1)} - \tilde{x}_{ij(k-1)}}{P_{k+1} - P_{k-1}} \quad (4.16)$$

$$\left.\frac{\partial \tilde{x}_{ij}}{\partial T}\right|_k = \frac{\tilde{x}_{ij(k+1)} - \tilde{x}_{ij(k-1)}}{T_{k+1} - T_{k-1}} \quad (4.17)$$

This will then form a look-up table which will be used for interpolation based on the numerical values of pressure and temperature during the simulation.
Thus, expressions for dX_{ij} can then be obtained from Eqs. (4.7) to (4.9).

4.3 NON-ZERO CAPILLARY PRESSURE

For non-negligible capillary pressure, the fluid properties x_{ij} and ρ_{ij} should be calculated from the phase pressure, P_j, as opposed to the global pressure, P. An equation of state can provide derivatives of these variables with respect to P_j. But to obtain derivatives with respect to P, the following transformations must be applied:

$$\frac{\partial x_{ij}}{\partial P} = \frac{\partial P_j}{\partial P}\frac{\partial x_{ij}}{\partial P_j} \tag{4.18}$$

$$\frac{\partial \rho_{ij}}{\partial P} = \frac{\partial P_j}{\partial P}\frac{\partial \rho_{ij}}{\partial P_j} \tag{4.19}$$

For two phase flow systems, Eq. (2.37) reduces to

$$P_j = P - (-1)^j(1-S_j)P_c \tag{4.20}$$

where $P_c = P_g - P_l$ is the capillary pressure.

Noting that P_c is generally expressed uniquely as a function of S_g, e.g., (Van Genuchten, 1980) and that $dS_g = -dS_l$, differentiating Eq. (4.20) with respect to P leads to:

$$\frac{\partial P_j}{\partial P} = 1 - \left(P_c + (-1)^j(1-S_j)\frac{\partial P_c}{\partial S_g}\right)\frac{\partial S_g}{\partial P} \tag{4.21}$$

Recalling Eq. (4.3) and that z_i are independent of P it can be said that

$$\frac{1}{S_g}\frac{\partial S_g}{\partial P} = S_l \sum_{j=1}^{2} Y_j \frac{\partial P_j}{\partial P} \tag{4.22}$$

where:

$$Y_j = (-1)^j \left[\frac{1}{\rho_j} \frac{\partial \rho_j}{\partial P_j} - \frac{1}{(z_i - X_{ij})} \frac{\partial X_{ij}}{\partial P_j} \right] \tag{4.23}$$

from which we obtain:

$$\frac{\partial S_g}{\partial P} = \left[\frac{1}{S_g S_l} + \sum_{j=1}^{2} \left(P_c + (-1)^j (1 - S_j) \frac{\partial P_c}{\partial S_g} \right) Y_j \right]^{-1} \sum_{j=1}^{2} Y_j \tag{4.24}$$

4.4 CHANGE OF BULK DENSITY WITH PRESSURE

Compressibility is defined as the change in density with respect to pressure (at constant temperature and composition):

$$\alpha_b = \frac{1}{\rho_b} \left(\frac{\partial \rho_b}{\partial P} \right)_{T,\ z_i} \tag{4.25}$$

From Eq.(4.1) and assuming constant porosity ($d\phi$=0):

$$\frac{\partial \rho_b}{\partial P} = \phi \sum_{j=1}^{N_p} \rho_j S_j \left(\alpha_j + \frac{1}{S_j} \frac{\partial S_j}{\partial P} \right) \tag{4.26}$$

dS_j is given by Eq.(4.3), where because P and z_i are both PDVs and therefore independent of each other, then $\frac{\partial z_i}{\partial P} = 0$:

$$\frac{\partial S_j}{\partial P} = S_g S_l \sum_{j=1}^{2} (-1)^j \left[\alpha_j + \frac{1}{X_{ij} - z_i} \frac{\partial X_{ij}}{\partial P} \right] \tag{4.27}$$

recall that α_j [$\mathrm{LT^2M^{-1}}$] is the phase compressibility and is given by Eq. (4.4):

$$\alpha_j = \frac{1}{\rho_j} \frac{\partial \rho_j}{\partial P} = \rho_j \sum_{i=1}^{N_c} \frac{X_{ij}}{\rho_{ij}} \left(\alpha_{ij} - \frac{1}{X_{ij}} \frac{\partial X_{ij}}{\partial P} \right) \tag{4.28}$$

where α_{ij} [$\mathrm{LT^2M^{-1}}$] is the component-wise compressibility and can be obtained from the National Institute of Standard and Technology (NIST) Web book (Lemmon, 2011) in the form of look up tables for different values of pressures and temperatures.

The only remaining quantity in calculating α_b, is the $\frac{\partial X_{ij}}{\partial P}$ term which is given by Eq.(4.7).

4.5 CHANGE OF BULK DENSITY WITH TEMPERATURE

Thermal expansivity is defined as the change in density with respect to temperature (at constant pressure and composition) :

$$\beta_b = -\frac{1}{\rho_b}\left(\frac{\partial \rho_b}{\partial T}\right)_{P,\ z_i} \tag{4.29}$$

From Eq.(4.1) and assuming constant porosity ($d\phi$=0):

$$\frac{\partial \rho_b}{\partial T} = \phi \sum_{j=1}^{N_p} \rho_j S_j \left(\beta_j + \frac{1}{S_j}\frac{\partial S_j}{\partial T}\right) \tag{4.30}$$

dS_j is given by Eq.(4.3), where because T and z_i are both PDVs and therefore independent of each other, then $\frac{\partial z_i}{\partial T} = 0$:

$$\frac{\partial S_j}{\partial T} = S_g S_l \sum_{j=1}^{2} (-1)^j \left[\beta_j + \frac{1}{X_{ij} - z_i}\frac{\partial X_{ij}}{\partial T}\right] \tag{4.31}$$

β_j [K^{-1}] is the phase thermal expansion coefficient and is given by Eq. (4.4):

$$\beta_j = -\frac{1}{\rho_j}\frac{\partial \rho_j}{\partial T} = \rho_j \sum_{i=1}^{N_c} \frac{X_{ij}}{\rho_{ij}} \left(\beta_{ij} + \frac{1}{X_{ij}}\frac{\partial X_{ij}}{\partial T}\right) \tag{4.32}$$

where β_{ij} [K^{-1}] is the component-wise thermal expansioncoefficient and we obtain them from the National Institute of Standard and Technology (NIST) Web book (Lemmon, 2011) in the form of look up tables for different values of temperature and pressure.

The only remaining quantity in calculating β_b, is the $\frac{\partial X_{ij}}{\partial T}$ term which is given by Eq.(4.8).

4.6 CHANGE OF BULK DENSITY WITH COMPOSITION

The Change in fluid density with respect to composition can be stated as (at constant pressure and temperature):

$$\gamma_{b_i} = \frac{1}{\rho_b}\left(\frac{\partial \rho_b}{\partial z_i}\right)_{P,\,T} \tag{4.33}$$

From Eq.(4.1) and assuming constant porosity ($d\phi$=0):

$$\frac{\partial \rho_b}{\partial z_i} = \phi \sum_{j=1}^{N_p} \rho_j S_j \left(\gamma_{ji} + \frac{1}{S_j}\frac{\partial S_j}{\partial z_i}\right) \tag{4.34}$$

dS_j is given by Eq.(4.3):

$$\frac{\partial S_j}{\partial z_i} = S_g S_l \sum_{j=1}^{2} (-1)^j \left[\gamma_{ji} - \frac{1}{z_i - X_{ij}}\left(1 - \frac{\partial X_{ij}}{\partial z_i}\right)\right] \tag{4.35}$$

γ_{ji} [-] is given by Eq. (4.4), where ρ_{ij} [ML^{-3}] is pure component densities and therefore independent of composition i.e. $\frac{\partial \rho_{ij}}{\partial z_i} = 0$:

$$\gamma_{ji} = \frac{1}{\rho_j}\frac{\partial \rho_j}{\partial z_i} = -\rho_j \sum_{i=1}^{N_c} \frac{1}{\rho_{ij}}\frac{\partial X_{ij}}{\partial z_i} \tag{4.36}$$

The only remaining quantity in calculating γ_{bi}, is the $\frac{\partial X_{ij}}{\partial z_i}$ term which is given by Eq.(4.9).

5

ANALYTICAL SOLUTION

This chapter briefly introduces the analytical solution by Hosseini et al. (2012) for the three-component two-phase flow problem in the context of CO_2 injection into brine aquifers, which will be used in the next chapter to verify our numerical model.

5.1 INTRODUCTION

In Chapter 2, the governing equations of multi-component multi-phase (MCMP) flow problems were introduced and in Chapter 3 the phase equilibrium model for ternary system of interest was discussed. Later in Chapter 4, a method of analytical differentiation for evaluation the derivative of the bulk flow density per volume of rock, ρ_b [ML^{-3}], with respect to Primary Dependant Variables (PDV) was derived. These three chapters provide all the necessary information for building a numerical model to simulate the gas injection problem.

However, generally, any numerical model needs to be benchmarked by experimental data or verified by an existing analytical solution for the problem it is trying to simulate, before its results can be deemed valid for practical applications.

This chapter introduces an existing Method of Characteristics (MOC) solution by Hosseini et al. (2012) for CO_2 injection into a brine aquifer, who extended the analytical solution of Mathias et al. (2011b) by incorporating dissolved and/or residual CH_4. In this way, the solution additionally accounts for partial miscibility of the CO_2-CH_4-H_2O system. This analytical solution will be used in the next chapter to verify our numerical model.

5.2 METHOD OF CHARACTERISTICS

The Method of Characteristics (MOC) is a general technique for solving hyperbolic partial differential equations. Therefore, in the absence of diffusion/dispersion and under the assumption of constant fluid properties, another way to solve Eq. (2.12) is to use MOC.

The idea is to evaluate trajectories along which the mass concentrations, G_i, are constant, such that:

$$\frac{dG_i}{d\eta} = \frac{\partial G_i}{\partial \tau}\frac{d\tau}{d\eta} + \frac{\partial G_i}{\partial \xi}\frac{d\xi}{d\eta} = 0 \tag{5.1}$$

where η is a parameter defining the characteristic paths and ξ and τ are the space and time variables respectively. Assuming constant fluid properties, the term H_i in Eq. (2.12) is only a function of G_i. Therefore, Eq. (2.12) can be written as:

$$\frac{\partial G_i}{\partial \tau} + \frac{dH_i}{dG_i}\frac{\partial G_i}{\partial \xi} = 0 \tag{5.2}$$

Comparing Eqs. (5.1) and (5.2) term by term, it can be understood that:

$$\frac{dG_i}{d\eta} = 0 \tag{5.3}$$

$$\frac{d\tau}{d\eta} = 1 \tag{5.4}$$

$$\frac{d\xi}{d\eta} = \frac{dH_i}{dG_i} \tag{5.5}$$

Eqs. (5.3), (5.4) and (5.5) are known as characteristic equations and integrating them will give the expressions for G_i, ξ and τ. In other words, $\tau(\eta)$ and $\xi(\eta)$ are characteristic paths (curves) along which G_i are constant.

Since G_i is constant along the characteristic curves (with respect to parameter η), $\frac{dH_i}{dG_i}$ is also constant and therefore Eqs (5.4) and (5.5) can be easily integrated, and η eliminated to obtain relationship between τ and ξ:

$$\xi = \frac{dH_i}{dG_i}\tau + \xi_0 \tag{5.6}$$

where ξ_0 is the initial position of G_i. Eq. (5.6) is a straight line and the velocity with which the compositions propagate on these lines is:

$$\frac{d\xi}{d\tau} = \frac{dH_i}{dG_i} \tag{5.7}$$

The velocity at which a given composition propagates is often referred to as the "wave-velocity" of that composition. In the case of MCMP flow, the wave velocity of the overall composition of the multiphase mixture is different from the physical flow velocity of any of the phases. The wave velocity indicates how fast that overall composition moves, not how fast the individual phases move (Orr, 2007, p. 45).

Under an assumption of constant fluid properties, the wave velocity can be evaluated analytically for a compositional flow problem as follows.

5.3 EVALUATION OF THE WAVE VELOCITY

Consider a two-phase three-component system governed by Eq. (2.12), in radial flow coordinates, r:

$$\frac{\partial}{\partial t}\overbrace{[\phi(\rho_1 X_{i1} S_1 + \rho_2 X_{i2} S_2)]}^{G_i} + \frac{1}{r}\frac{\partial}{\partial r}[r\overbrace{(\rho_1 X_{i1} q_1 + \rho_2 X_{i2} q_2)}^{H_i}] = 0 \tag{5.8}$$

Defining the cross-sectional area, A [L^2]:

$$A = 2\pi r H_f \tag{5.9}$$

where H_f [L] is the formation thickness. Applying the fractional-flow concept (Buckley & Leverett, 1942):

$$f_j = A\frac{q_j}{q_t} \tag{5.10}$$

$$q_t = A(q_1 + q_2) \tag{5.11}$$

thus Eq.(5.8) takes the form:

$$\frac{\partial}{\partial t}[(\rho_1 X_{i1} S_1 + \rho_2 X_{i2} S_2)] + \frac{1}{2\phi\pi r H_f}\frac{\partial}{\partial r}[q_t(\rho_1 X_{i1} f_1 + \rho_2 X_{i2} f_2)] = 0 \tag{5.12}$$

further, defining a mass injection rate, M_{inj} [MT^{-1}]:

$$M_{inj} = \frac{q_{inj}}{\rho_{inj}} \tag{5.13}$$

and defining the following dimensionless variables:

$$q_D = \frac{q_t}{q_{inj}} = \frac{\rho_{inj} q_t}{M_{inj}} \tag{5.14}$$

$$\rho_{1_D} = \frac{\rho_1}{\rho_{inj}} \tag{5.15}$$

$$\rho_{2_D} = \frac{\rho_2}{\rho_{inj}} \tag{5.16}$$

where subscripts inj and D denote injection fluid properties and dimensionless variable respectively. Then the equations reduce to:

$$\frac{\partial G_{i_D}}{\partial t} + \frac{M_{inj}}{\phi\pi H_f \rho_{inj}}\frac{\partial H_{i_D}}{\partial r^2} = 0 \tag{5.17}$$

where:

$$G_{i_D} = \rho_{1_D} X_{i1} S_1 + \rho_{2_D} X_{i2} S_2 \tag{5.18}$$

$$H_{i_D} = a_{i_D} q_D \tag{5.19}$$

$$a_{i_D} = \rho_{1_D} X_{i1} f_1 + \rho_{2_D} X_{i2} f_2 \tag{5.20}$$

$$q_D = \frac{2\pi r H_f \rho_{inj} (q_1 + q_2)}{M_{inj}} \tag{5.21}$$

The assumption of constant fluid properties leads to phase densities (ρ_j) and component mass fractions (X_{ij}) being fixed, which in turn leads to G_{i_D} being a function of phase saturations (S_j) only; it follows that H_{i_D} is a function of fractional flows (f_j) only. Therefore, in the absence of gravity, fractional flow is a function of phase saturation only, which in turn leads to H_{i_D} being a function of G_{i_D} only. Using chain-rule differentiation, Eq.(5.17) can be re-written as:

$$\frac{\partial G_{i_D}}{\partial t} + \frac{M_{inj}}{\phi \pi H_f \rho_{inj}} \frac{dH_{i_D}}{dG_{i_D}} \frac{\partial G_{i_D}}{\partial r^2} = 0 \tag{5.22}$$

which leads to:

$$\frac{dr^2}{dt} = \frac{M_{inj}}{\phi \pi H_f \rho_{inj}} \frac{dH_{i_D}}{dG_{i_D}} \tag{5.23}$$

after integration:

$$z = \frac{dH_{i_D}}{dG_{i_D}} = \frac{\phi \pi r^2 H_f \rho_{inj}}{t M_{inj}} \tag{5.24}$$

which gives an expression for the velocity of propagation that appears in Eq. (5.2). Furthermore, due to self similarity, Eq.(5.24) allows Eq. (5.17) to reduce to (Hosseini et al., 2012):

$$z\frac{dG_{i_D}}{dz} + \frac{dH_{i_D}}{dz} = 0 \qquad , \qquad i \in [1,2,3] \tag{5.25}$$

where in this case $i = 1$ denotes CO_2, $i = 2$ denotes CH_4 and $i = 3$ denotes H_2O components of the flow. Phase $j = 1$ denotes the gas phase and $j = 2$ denotes the liquid phase.

5.4 A THREE REGION SYSTEM

Consider pure CO_2 injected into a reservoir containing H_2O and residually trapped CH_4. Numerical simulations of this phenomenon predict exsolution of CH_4 and its accumulation on the edges of the CO_2 plume, leading to development of a three region system (Taggart, 2010, Oldenburg & Doughty, 2011, Battistelli & Marcolini, 2009) as is shown in Figure 4. These regions, starting from the well bore and moving outward are: (1) a single-phase, dry-out region around the well-bore filled with pure CO_2. (2) a two-phase, two-component system containing CO_2 and brine. (3) a two-phase, two-component system containing CH_4 and brine. Note that accumulation of the CH_4 bank ahead of the CO_2 plume is a result of the CH_4 being the lightest component, and therefore traveling faster than CO_2 in the compositional space.

The formation of this three-region system can also be explained on a ternary diagram. Fig. 5 is a schematic of the ternary system of interest. The geometric nature of the two-phase region is controlled by vapour-liquid equilibrium ratios (K-values) of the individual components. The linear geometric the two-phase region for this system is indicative of a constant K-value system(Orr, 2007).

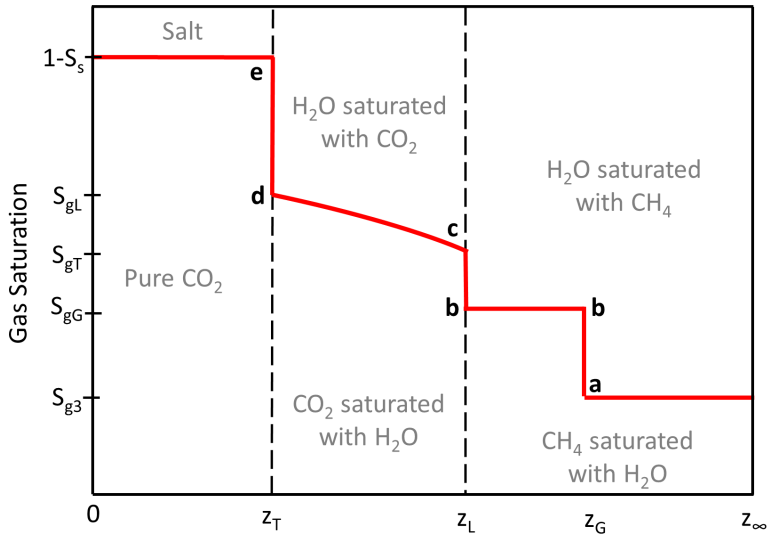

Figure 4: Schematic of the development of a three-region system after CO_2 injection into a mixture CH_4-H_2O initially in chemical equilibrium.

K-value is a measure of volatility (see chapter 3). The three components, in order of volatility, are $CH_4 > CO_2 > H_2O$. As a consequence, in this case, CO_2 is the intermediate component in terms of volatility. Furthermore, the K-value for CO_2 is > 1. Consequently, it can be deduced that this is a High Volatility Intermediate (HVI) system.

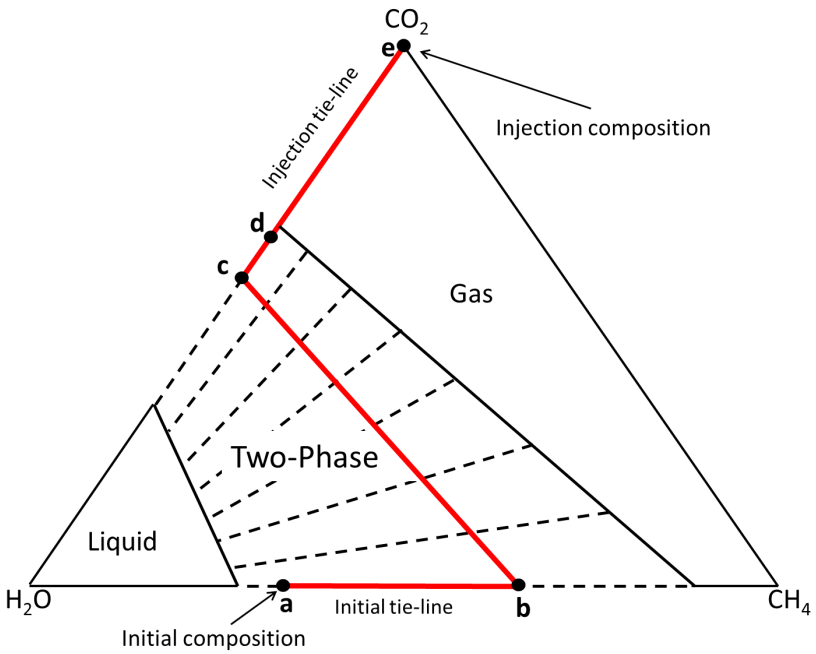

Figure 5: Schematic of composition path in ternary diagram for CO_2-CH_4-H_2O system.

The MOC solution construction requires the knowledge of the solution profile a priori. In other words, in MOC solution, we accept that the gas saturation profile is of the form depicted in Figure 4 and thus includes three shocks. The remaining challenge is then obtaining the location of these shocks by imposing the Rankine-Hugoniot (mass conservation) condition through these shocks. This will be discussed in the next section.

5.5 LOCATION OF THE SHOCKS

The first shock, located at $z = z_T$, is a trailing shock, which marks the extent of the dry-out region within the injected CO_2 plume, where all water has been evaporated. The second shock, located at $z = z_L$, is a leading shock, marking the extent of the injected CO_2 plume. The region $z_T \leq z \leq z_L$ is two-phase, where CO_2 and water are in equilibrium. The final shock, located at $z = z_G$, marks the extent of the mobilized

CH_4, which is caused by the injection of CO_2. The region between $z_L \leq z \leq z_G$ is also two-phase, but with CH_4 and H_2O in equilibrium.

The idea is to impose the mass conservation statement for any one of the components as they go through each of the shocks to find a unique value for fluid saturations and non-dimensional flow velocities.

Integrating Eqs.(5.25) from $z = 0$ tp $z \to \infty$,

$$H^0_{1_D} = G^0_{1_D} z_T + \int_{z_T}^{z_L} G_{1_D} dz \tag{5.26}$$

$$-H^\infty_{2_D} = G^G_{2_D}(z_G - z_L) - G^\infty_{2_D} z_G \tag{5.27}$$

$$-H^\infty_{3_D} = \int_{z_T}^{z_L} G_{3_D} dz + G^G_{3_D}(z_G - z_L) - G^\infty_{3_D} z_G \tag{5.28}$$

where superscripts denote the value at different locations, in the form $z = [0,\ z_T,\ z_L,\ z_G,\ z_\infty]$, as depicted in Figure 4.

Application of the chain rule followed by integration by parts leads to

$$\int_{z_T}^{z_L} G_{1_D} dz = G^L_{1_D} z_L - G^T_{1_D} z_T - \int_{z_T}^{z_L} z dG_{1_D}$$

$$= G^L_{1_D} z_L - G^T_{1_D} z_T - \int_{z_T}^{z_L} dH_{1_D}$$

$$= G^L_{1_D} z_L - H^L_{1_D} - G^T_{1_D} z_T + H^T_{1_D} \tag{5.29}$$

Applying Eq(5.29) into Eq.(5.26) and similarly in Eq.(5.28) gives

$$H^0_{1_D} = G^0_{1_D} z_T + G^L_{1_D} z_L - H^L_{1_D} - G^T_{1_D} z_T + H^T_{1_D} \tag{5.30}$$

$$-H_{3_D}^{\infty} = G_{3_D}^{L} z_L - H_{3_D}^{L} - G_{3_D}^{T} z_L + H_{3_D}^{T} + G_{3_D}^{G}(z_G - z_L) - G_{3_D}^{\infty} z_G \tag{5.31}$$

Considering the mass conservation statements for CO_2 and H_2O in the region $0 \leq z \leq z_T$, the location of the trailing front, z_T, can be derived,

$$H_{1_D}^{0} - H_{1_D}^{T} = (G_{1_D}^{0} - G_{1_D}^{T}) z_T \tag{5.32}$$

$$-H_{3_D}^{T} = -G_{3_D}^{T} z_T \tag{5.33}$$

after rearrangement

$$z_T = \frac{H_{1_D}^{0} - H_{1_D}^{T}}{G_{1_D}^{0} - G_{1_D}^{T}} = \frac{H_{3_D}^{T}}{G_{3_D}^{T}} \tag{5.34}$$

To derive an expression for location of the leading front, z_L, consider the mass conservation statements for CO_2, CH_4, and H_2O in region $0 \leq z \leq z_L$,

$$H_{1_D}^{0} = G_{1_D}^{0} z_T + G_{1_D}^{L} z_L - H_{1_D}^{L} - G_{1_D}^{T} z_T + H_{1_D}^{T} \tag{5.35}$$

$$-H_{2_D}^{G} = G_{2_D}^{G} z_L \tag{5.36}$$

$$H_{3_D}^{G} = G_{3_D}^{L} z_L - H_{3_D}^{L} - G_{3_D}^{T} z_T + H_{3_D}^{T} - G_{3_D}^{G} z_G \tag{5.37}$$

Rearrangement leads to,

$$z_L = \frac{H_{1_D}^{L}}{G_{1_D}^{L}} = \frac{H_{2_D}^{G}}{G_{2_D}^{G}} = \frac{H_{3_D}^{G} - H_{3_D}^{L}}{G_{3_D}^{G} - G_{3_D}^{L}} \tag{5.38}$$

Finally, substituting Eqs.(5.34) and (5.38) in Eq.(5.28) and Eq.(5.31) yields the location of the gas bank front,

$$z_G = \frac{H^G_{2_D} - H^\infty_{2_D}}{G^G_{2_D} - G^\infty_{2_D}} = \frac{H^G_{3_D} - H^\infty_{3_D}}{G^G_{3_D} - G^\infty_{3_D}} \tag{5.39}$$

In each region, fluids are in equilibrium. Under such conditions, q_D is piecewise constant and can be defined by,

$$q_D = \begin{cases} q_{D_1}, & 0 \le z < z_T \\ q_{D_2}, & z_T \le z \le z_L \\ q_{D_3}, & z > z_L \end{cases} \tag{5.40}$$

From Eqs.(5.34) and (5.38), by replacing the H and G terms by their definition, it can be shown that

$$\frac{q_{D_1} a^0_{1_D} - q_{D_2} a^T_{1_D}}{G^0_{1_D} - G^T_{1_D}} = \frac{q_{D_1} a^T_{3_D}}{G^T_{3_D}} \tag{5.41}$$

$$\frac{q_{D_2} a^L_{1_D}}{G^L_{1_D}} = \frac{q_{D_3} a^G_{2_D}}{G^G_{2_D}} = \frac{q_{D_3} a^G_{2_D} - q_{D_2} a^L_{3_D}}{G^G_{3_D} - G^L_{3_D}} \tag{5.42}$$

which on solving for q_{D_2} and q_{D_3}, leads to

$$q_{D_2} = q_{D_1} \left[\frac{a^0_{1_D} G^T_{2_D}}{a^T_{3_D}(G^0_{1_D} - G^T_{1_D}) + a^T_{1_D} G^T_{3_D}} \right] \tag{5.43}$$

$$q_{D_3} = \frac{q_{D_2} a^L_{1_D} G^G_{2_D}}{a^G_{2_D} G^L_{1_D}} = q_{D_2} \left[\frac{a^L_{1_D}(G^G_{3_D} - G^L_{3_D}) + a^L_{3_D} G^L_{1_D}}{a^G_{3_D} G^L_{1_D}} \right] \tag{5.44}$$

Note that in the single-phase, dry-out region ($0 \le z \le z_T$), since there is no component transfer between phases, volumetric flow rate is unchanged from that at the injection point. Therefore, $q_{D_1} = 1$ (Hosseini et al., 2012).

The region where the phase fractional flow, defined by Eq. (5.10), is a differentiable function of phase saturation, S_j, is called the spreading wave (Orr, 2007). Within the spreading wave, from Eq.(5.25), it can be shown that

$$z = q_D \frac{df_1}{dS_1} \tag{5.45}$$

from which it follows

$$z_L = q_{D_2} \frac{df_1}{dS_1}\Big|_{S_1=S_1^L} \tag{5.46}$$

$$z_T = q_{D_2} \frac{df_1}{dS_1}\Big|_{S_1=S_1^T} \tag{5.47}$$

Note that q_{D_2} and q_{D_3} need to be estimated iteratively, except for the special case in which the injection composition is free of H_2O and CH_4 and the initial brine aquifer composition is free of CO_2 (Hosseini et al., 2012). In this study, it is assumed that the injection fluid is free of water and CH_4 and that the brine aquifer is initially free of CO_2. Also, the volumetric saturation of precipitated salt is neglected(Zeidouni, 2009). As a result,

$$G_{1_D}^0 = a_{1_D}^0 = 1 \tag{5.48}$$

$$G_{3_D}^0 = a_{3_D}^0 = G_{2_D}^0 = a_{2_D}^0 = G_{1_D}^\infty = a_{1_D}^\infty = 0 \tag{5.49}$$

Therefore, S_1^T can be calculated directly from Eq.(5.34) without the knowledge of q_{D_2} and then q_{D_2} can be calculated from Eq.(5.43). Similarly, S_1^L can be calculated form Eq.(5.38)without the knowledge of q_{D_3} and then q_{D_3} can be calculated from Eq.(5.44). S_1^G should then have value to satisfy Eq.(5.43) and ,

$$\frac{a_{3_D}^G G_{2_D}^G - a_{2_D}^G G_{3_D}^G}{a_{2_D}^G} = \frac{a_{3_D}^L G_{1_D}^L - a_{1_D}^L G_{3_D}^L}{a_{1_D}^L} \tag{5.50}$$

By iterating between Eqs.(5.44) and (5.50), S_1^G can be found, from which, and using Eq.(5.39), z_G can be calculated.

5.6 FRACTIONAL FLOW

Substituting Eq.(2.19) in Eq.(5.10) and assuming Corey type relative permeability curves given by Eq.(2.21), it leads to (Hosseini et al., 2012),

$$f_1 = \left[1 + \frac{\mu_1 k_{r_{2_0}}}{\mu_2 k_{r_{1_0}}} \left(\frac{S_2 - S_{2_c}}{1 - S_{1_c} - S_{2_c}}\right)^{n_2} \left(\frac{S_1 - S_{1_c}}{1 - S_{1_c} - S_{2_c}}\right)^{-n_1}\right]^{-1} \tag{5.51}$$

and differentiating Eq.(5.51) yields(Hosseini et al., 2012)

$$\frac{df_1}{dS_1} = f_1 f_2 \left[\frac{n_1(S_2 - S_{2_c}) + n_2(S_1 - S_{1_c})}{(S_1 - S_{1_c})(1 - S_{1_c} - S_{2_c})}\right] \tag{5.52}$$

5.7 PRESSURE DISTRIBUTION

To obtain an equation for pressure, we return to Darcy's law for total fluid flow rate

$$q_t = q_1 + q_2 = -k\left(\frac{k_{r_1}}{\mu_1} + \frac{k_{r_2}}{\mu_2}\right)^{-1} \frac{dP}{dr} \tag{5.53}$$

Applying the similarity transform, z, along with the q_D identity, and then rearranging leads to

$$\frac{dP}{dz} = -\frac{M_{inj}}{4\pi h k \rho_{inj}} \left(\frac{k_{r_1}}{\mu_1} + \frac{k_{r_2}}{\mu_2}\right)^{-1} \frac{q_D}{z} \tag{5.54}$$

From our knowledge of the shock fronts, it can then be said that (Hosseini et al., 2012)

$$\frac{dP}{dz} = -\frac{M_{inj}}{4\pi hk\rho_{inj}} \begin{cases} \frac{\mu_{inj} q_{D_1}}{k_{r_{1_0}} z} & , \quad 0 \leq z < z_T \\ \left(\frac{k_{r_1}}{\mu_c} + \frac{k_{r_2}}{\mu_w}\right)^{-1} \frac{q_{D_2}}{z} & , \quad z_T \leq z \leq z_L \\ \left(\frac{k_{r_1}}{\mu_m} + \frac{k_{r_2}}{\mu_w}\right)^{-1} \frac{q_{D_3}}{z} & , \quad z_L < z \leq z_G \\ \frac{\mu_w q_{D_3}}{k_{r_{2_0}} z} & , \quad z > z_G \end{cases} \tag{5.55}$$

where μ_c, μ_m and μ_w are the dynamic viscosities of CO_2, CH_4 and H_2O respectively. Integrating with respect to z,

$$P - P_0 = \frac{M_{inj}}{4\pi hk\rho_{inj}} \begin{cases} \frac{\mu_{inj}}{k_{r_{1_0}}} \ln\left(\frac{z_T}{z}\right) + \mu_c q_{D_2} F_3(z_T) + \mu_m q_{D_3} F_2(z_L) + \frac{\mu_w q_{D_3}}{k_{r_{2_0}}} F_1(z_G) & , \quad 0 \leq z < z_T \\ \mu_c q_{D_2} F_3(z) + \mu_m q_{D_3} F_2(z_L) + \frac{\mu_w q_{D_3}}{k_{r_{2_0}}} F_1(z_G) & , \quad z_T \leq z \leq z_L \\ \mu_m q_{D_3} F_2(z) + \frac{\mu_w q_{D_3}}{k_{r_{2_0}}} F_1(z_G) & , \quad z_L < z \leq z_G \\ \frac{\mu_w q_{D_3}}{k_{r_{2_0}}} F_1(z_G) & , \quad z > z_G \end{cases} \tag{5.56}$$

where P_0 is the initial pressure of the reservoir. Following Mathias et al. (2009, 2011a,b), it can be shown that for a circular, closed reservoir of radial extent, r_E,

$$F_1(z) = \begin{cases} E_1(\alpha z) & , \quad z_E > \frac{0.5615}{\alpha} \\ \frac{1}{\alpha z_E} - \frac{3}{2}\ln\left(\frac{z_E}{z}\right) + \frac{z - z_G}{z_E} & , \quad z_E \leq \frac{0.5615}{\alpha} \end{cases} \tag{5.57}$$

$$F_2(z) = \frac{1}{\mu_m}\left[\frac{k_{r_2}}{\mu_w} + \frac{k_{r_1}}{\mu_m}\right]^{-1}_{S_1 = S_1^G} \ln\left(\frac{z_G}{z}\right) \tag{5.58}$$

$$F_3(z) = -\frac{1}{\mu_c}\int_z^{z_L} \left(\frac{k_{r_2}}{\mu_w} + \frac{k_{r_1}}{\mu_c}\right)^{-1} \frac{1}{z} dz \tag{5.59}$$

where

$$\alpha = \frac{\mu_w M_{inj}(c_r + S_2^{\infty} c_w + S_1^{\infty} c_m)}{4\pi hk\rho_{inj}} \tag{5.60}$$

E_1 is the first-order exponential integral function; c_r , c_w, and c_m are rock, water, and methane compressibilities, respectively; and S_1^∞ is the initial gas saturation in the brine aquifer. And $S_2^\infty = 1 - S_1^\infty$.

6

NUMERICAL SOLUTION USING METHOD OF LINES (MOL)

This chapter describes our numerical model that was developed to solve the two-phase three-component flow problem, in the context of CO_2 injection into a reservoir initially only containing CH_4+H_2O. The numerical model is based on the so called Method of Lines (MOL) approach in which all but one dimension are discretised and the resulting system of ODEs are solved using an ODE-solver of choice; in this case MATLAB's ode-solver ode15s.

6.1 INTRODUCTION

Simulation of multi-component multi-phase (MCMP) flow in porous media typically involves solving a coupled set of conservation equations for each component as were derived in Chapter 2. In the absence of diffusion and capillary pressure, this problem is governed by a set of coupled hyperbolic and parabolic transport equations. Hyperbolic equations frequently give rise to the formation of shocks, leading to difficulties with regard to obtaining accurate solutions. Problems associated with one dimensional transport of incompressible fluids, in the absence of capillary pressure and under isothermal conditions, can be solved exactly using the method of characteristics (see Chapter 5). However, even under these restricting conditions, great care must be taken when considering non-zero initial conditions and non-unity boundary conditions (for example, see Section 4.3 of Orr (2007)).

Alternative techniques involve the application of approximate methods. The spatial dimension is typically treated using conservative methods such as finite

volume (Chen et al., 2006). Alternatively, one can consider the use of finite elements (Chen et al., 2006) or pseudo-spectral methods (Mathias et al., 2006). Such spatial schemes give rise to either stability problems or numerical diffusion due to truncation terms associated with the Taylor's expansion, the latter of which can be reduced using flux limiters or their variants (e.g. Mallison et al., 2005).

Handling of the temporal term, which is critical to resolving the non-linear nature of the problem, generally revolves around the choice of explicit or implicit treatment. Fully explicit treatment, although easier to implement, can run into severe time-step limitations due to the well known CFL (Courant - Friedrichs - Lewy) condition. Fully implicit treatment leads to an unconditionally stable solution (as far as time-stepping is concerned), but leads to additional numerical diffusion. Furthermore, implementation of the solution is significantly more challenging.

Popular approaches for solving MCMP problems in this context are the so-called semi-implicit methods, the most common variant of which is referred to as ImPES (Implicit Pressure Explicit Saturation) (Chen et al., 2006) or ImPEM (Implicit Pressure Explicit Mass). In ImPES, the governing equations are rearranged to identify a transport equation of hyperbolic nature (or nearly hyperbolic depending on whether or not capillarity is included) and a pressure equation of parabolic or elliptic character. The pressure equation is solved implicitly which allows for larger time-steps. The transport equation is solved explicitly, allowing easier implementation and reduced computational memory requirements; hence the semi-implicitness. Both the implicit and explicit time-stepping typically employ simple first-order schemes.

Multi-step-multi-order time integration algorithms (Shampine et al., 1997) represent an alternative method, which treats the temporal term in a more accurate fashion. These techniques maintain a specific time integration error while maximizing the time-step size. Moreover, due to the wide availability (e.g. MATLAB or FORTRAN with NAG) of high quality solvers and simplicity of implementation, there is no need to redevelop the sophisticated time-integration algorithms. Rather,

the so-called method of lines (MOL) approach can be taken. In this case, the partial differential equations (PDEs) are discretised in space to form a set of coupled Ordinary Differential Equations (ODEs) (Wouwer et al., 2005). These can then be solved simultaneously using any ODE solver of choice.

For two-phase immiscible flow, where one of the phases is treated as inviscid, the MCMP problem reduces to a single PDE often referred to as Richards' equation (RE). This equation is commonly solved to better understand hydrological problems associated with unsaturated soils. Indeed, there are many recent articles (Mathias et al., 2006, 2008, Ireson, 2009) reporting MOL solutions of RE using the MATLAB ODE solver, ODE15s, which is particularly suitable for stiff systems of ODEs (Shampine et al., 1997). ODE15s has also been found to provide useful solutions to non-Darcian flow problems (Mathias et al., 2008, Wen et al., 2009) and two-phase immiscible flow problems (Mathias et al., 2009).

The focus of this thesis, however, has not been on comparing the performance of ODE solvers against other time integration methods such as IMPES, rather to provide a platform from which compositional flow problems can be solved with accuracy and stability, taking advantage of the existing libraries of ODE solvers available to public.

Thus, this chapter describes the details of numerical solution of two-phase three-component problem using MATLAB's ODE15s. In short, the system of PDEs describing our PDVs (derived in Chapter 2) will be solved. In each time step an equilibrium calculation will be perform using the model developed in Chapter 3. Furthermore, analytical technique of evaluation of the partial derivatives (Chapter 4) is applied for robustness and improved efficiency and accuracy.

A version of this chapter is presented in the following article:

Goudarzi S., Mathias S.A. & Gluyas J.G. (2016). Simulation of three-component two-phase flow in porous media using method of lines. Transport in Porous Media, 112(1), 1-19.

6.2 MATLAB'S ODE SUITE

MATLAB's ODE suite consists of five user-friendly solvers that solve initial value problems governed by first-order systems of Ordinary Differential Equations (ODEs). Consider, for instance, the following system of N number of PDEs:

$$\frac{\partial \boldsymbol{\psi}}{\partial t} + \nabla \cdot \mathbf{F} = 0 \tag{6.1}$$

where

$$\boldsymbol{\psi} = [\psi_1, \psi_2, ..., \psi_N]^T \tag{6.2}$$

$$\mathbf{F} = [F_1(\boldsymbol{\psi}), F_2(\boldsymbol{\psi}), ..., F_N(\boldsymbol{\psi})]^T \tag{6.3}$$

with initial condition:

$$\boldsymbol{\psi} = \boldsymbol{\psi_0} \qquad , \qquad t = 0 \tag{6.4}$$

This system of PDEs can be converted to a system of ODEs such that:

$$\frac{\partial \boldsymbol{\psi}}{\partial t} = \mathbf{D} \tag{6.5}$$

where

$$\mathbf{D} = \mathbf{J} \nabla \cdot \boldsymbol{\psi} \tag{6.6}$$

and is often approximated numerically using one of many possible discretisation schemes. The jacobian matrix $\mathbf{J}$ is defined as:

$$\mathbf{J} = \frac{\partial \mathbf{F}}{\partial \boldsymbol{\psi}} \tag{6.7}$$

A variety of numerical methods can then be used to solve Eq.(6.5), but they all fall into two general categories: Implicit and Explicit (or a combination of these).

The simplest explicit method is the one-step forward Euler method:

$$\boldsymbol{\psi}^{n+1} = \boldsymbol{\psi}^n + \Delta t \mathbf{D}^n \tag{6.8}$$

where Δt is the time step size and $\boldsymbol{\psi}^n$ is the numerical solution at current time step, n. The simplest implicit method is the one-step backward Euler method:

$$\boldsymbol{\psi}^{n+1} = \boldsymbol{\psi}^n + \Delta t \mathbf{D}^{n+1} \tag{6.9}$$

Eq. (6.9) is often solved using Newton's method or its variants.

Although very simple, one-step forward and backward Euler's methods are not very accurate and may require very small time-steps to maintain stability throughout the simulation. More accurate methods have been derived from Euler's method in two streams (Ashino, 2000):

- Linear multi-step methods: linearly combine values of $\boldsymbol{\psi}^{n-1}$, $\boldsymbol{\psi}^n$, $\boldsymbol{\psi}^{n+1}$, ..., and $\mathbf{D}^{n-1}$, $\mathbf{D}^n$, $\mathbf{D}^{n+1}$, ..., to obtain higher accuracy. The downside is that the method is no longer in one-step format, which makes it harder to change the time step during simulation and in accordance with stability/accuracy requirement of the system ODEs being solved.

- Runge-Kutta methods: nonlinearly combine values of $\boldsymbol{\psi}^{n-1}$, $\boldsymbol{\psi}^n$, $\boldsymbol{\psi}^{n+1}$, ..., and $\mathbf{D}^{n-1}$, $\mathbf{D}^n$, $\mathbf{D}^{n+1}$, ..., to obtain higher accuracy. Although the one-step format is maintained for ease of time-step change, but at the cost of sacrificing the linearity of the equations.

6.2.1 *Phenomenon of stiffness*

As soon as one deals with more than one first-order differential equation, the possibility of a stiff set of equations arises. Stiffness typically occurs in problems where there

are more than one different scales of dependencies on the independent-variable, e.g. space, time, etc. Consider the following set of equations where time (t) is the independent variable and u and v are the PDVs (Press, 2007, p. 931):

$$\begin{cases} \frac{\partial u}{\partial t} = \quad 998\ u(t) + 1998\ v(t) \\ \frac{\partial v}{\partial t} = -999\ u(t) - 1999\ v(t) \end{cases} \tag{6.10}$$

with initial conditions:

$$u(0) = 1 \qquad , \qquad v(0) = 0 \tag{6.11}$$

The set of ODEs can be solved using variable substitution and has the exact solution:

$$\begin{cases} u = \ 2e^{-t} - e^{-1000t} \\ v = -e^{-t} + e^{-1000t} \end{cases} \tag{6.12}$$

which has a slow decaying part and a fast decaying part. Von Neumann stability analysis reveals that, in integrating Eq.(6.10) using conventional Euler's methods, the presence of the e^{-1000t} term requires a step-size $\Delta t \ll \frac{1}{1000}$ for the method to be stable, which will result in prolonged simulation times. This is despite the fact that the e^{-1000t} term becomes completely insignificant in determining the values of u and v as soon as the solution moves away from $t = 0$.

In the case of MCMP problem, where we solve for pressure (P), temperature (T) and mass fractions (z_{CO_2} and z_{CH_4}), the stiffness primarily stems from co-existence of fast moving pressure-waves and slow moving composition and temperature fronts. Pressure-wave propagation-velocity is mainly controlled by the compressibility of the rock and fluids e.g. sound waves propagate with infinite velocity in an incompressible medium. This is often the reason why numerical simulation of complex incompressible (or nearly incompressible) flows is much more challenging.

In MATLAB's ODE suite, ode45, ode23 and ode113 are not suitable for solving stiff problems. In contrast, ode23s and ode15s have been specifically designed to

solve stiff problems. In this study we choose to use Ode15s, which is introduced in some detail below.

6.2.2 *Ode15s for stiff problems*

Ode15s is a multi-step multi-order (from 1^{st} to 5^{th} order accurate in time) stiff solver which uses the so-called Numerical Differentiation Formulas (NDFs). NDFs are a modified version of Backward Differentiation Formulae (BDFs) associated with Gear's method (Shampine et al., 1997). When using ode15s, the user is given the option of choosing between NDF or BDF methods. In our simulation we used the default setting to use the NDF, as they are said to be more efficient than BDF in the MATLAB's user manual.

6.2.3 *Time-step size properties*

Ode15s uses a variable time-stepping scheme which changes the step-size according to stability and accuracy requirement/specification of the problem being solved. It is possible to specify the size of the first step the solver tries, to potentially help it to better recognise the scale of the physical problem. Also, the user has the option of specifying an upper bound on the size of the time step if necessary (recommended by MATLAB for periodic solutions). In our simulation, we did not use any of these options.

6.2.4 *Error control properties*

The user can specify Relative and Absolute tolerance values when using ode15s, which are used by the solver as the convergence criteria in each time step.

RelTol : is a measure of the error relative to the size of each solution component.
AbsTol : is a threshold below which the value of the solution component is essentially insignificant to MATLAB.

In each time step the solver estimates the error e of each component k of the solution vector and uses the following criteria to decide whether the solution has converged or the time step needs to be reduced further:

$$e^n(k) \leq \max\Big[\ RelTol \times |\psi_k^n|\ ,\ AbsTol\Big] \tag{6.13}$$

The default values of $RelTol = 10^{-3}$ and $AbsTol = 10^{-6}$ were used in our simulations.

6.2.5 *Jaobian matrix properties*

In problems dealing with constant coefficient PDEs, the Jacobian matrix, **J**, is also constant and does not change as the solution evolves in time. It is possible to provide the ode-solver with a pre-calculated **J** to significantly reduce computational time. If no information is provided with regard to the Jacobian matrix, MATLAB will use finite difference to numerically evaluate Eq. (6.7) at every time step. In the case of MCMP problems, the coefficients of the PDEs are not constant, and therefore the Jacobian matrix needs to be evaluated at each time step.

However, it is well-known that when applying finite volume to discretise systems of PDEs, **J** will be sparse. Depending on the discretisation scheme used (e.g. one-sided, central, two points, three points, ...), the sparsity pattern of **J** can be known.

In MATLAB the user is given the option of providing a sparsity pattern ($JPat$) for the Jacobian matrix, which is essentially a matrix of zeros and ones. The solver will numerically evaluate the components of **J** where $JPat = 1$ and skips the Jacobian evaluations wherever $JPat = 0$. This can dramatically reduce computational time. This option was exploited in our simulations. More details regarding the Jacobian

pattern of our model will be provided later on in Section 6.5.1, after the finite volume discretisation scheme is discussed.

6.3 THE RIEMANN PROBLEM

Consider again the PDE in Eq. (6.1) and assume that it is discretised onto a blocked centered grid as illustrated in Figure 6. Note that the cells do not necessarily have the same size.

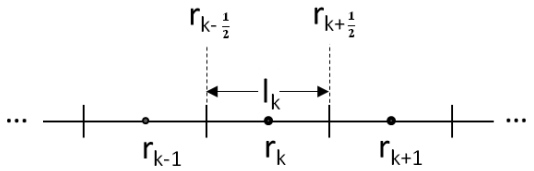

Figure 6: Schematic of the block centered gird.

Let r_k be the distance of the cell-k's centre from a reference point and l_k be the length of the cell k:

$$l_k = r_{k+\frac{1}{2}} - r_{k-\frac{1}{2}} \tag{6.14}$$

Integrating Eq. (6.1) over the interval $[r_{k-\frac{1}{2}}, r_{k+\frac{1}{2}}]$ and dividing by l_k:

$$\frac{\partial}{\partial t}\left(\frac{1}{l_k}\int_{r_{k-\frac{1}{2}}}^{r_{k+\frac{1}{2}}}\psi dr\right)+\frac{1}{l_k}\left(\int_{r_{k-\frac{1}{2}}}^{r_{k+\frac{1}{2}}}\frac{\partial}{\partial r}F(\psi)dr\right)=0 \tag{6.15}$$

which gives:

$$\frac{\partial\bar{\psi}_k}{\partial t}+\frac{1}{l_k}\left[F_{k+\frac{1}{2}}-F_{k-\frac{1}{2}}\right]=0 \tag{6.16}$$

where:

$$F_{k\pm\frac{1}{2}} = F(\psi(r_{k\pm\frac{1}{2}})) \tag{6.17}$$

and $\bar{\psi}_k$, the cell-k's average value is given by:

$$\bar{\psi}_k = \frac{1}{l_k} \int_{r_{k-\frac{1}{2}}}^{r_{k+\frac{1}{2}}} \psi dr \tag{6.18}$$

Note that Eq. (6.16) is still exact, i.e., no approximation has been introduced at this stage.

At the interface between adjacent numerical cells, the cell-averaged quantity $\bar{\psi}_k$ manifests a jump and has two values, thus generating a sequence of a so-called local Riemann problem (see Figure 7). For this reason, generally a Reimann-solver is required to evaluate the flux at the midpoints $r_{k\pm\frac{1}{2}}$. Godunov's method is one example of such a scheme which will be described further in the next sub-subsection.

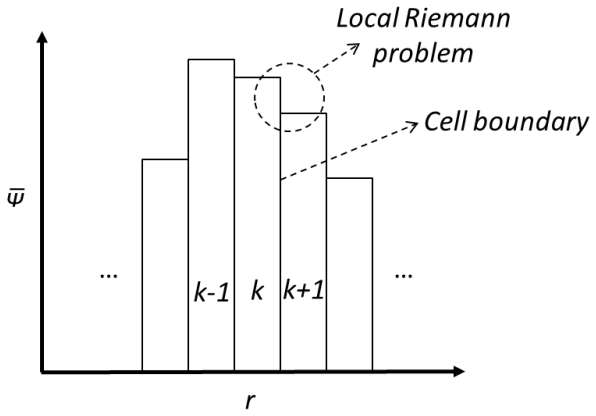

Figure 7: Schematic representation of a piece-wise constant distribution of ψ, giving rise to a sequence of local Riemann problems at the interface between adjacent cells.

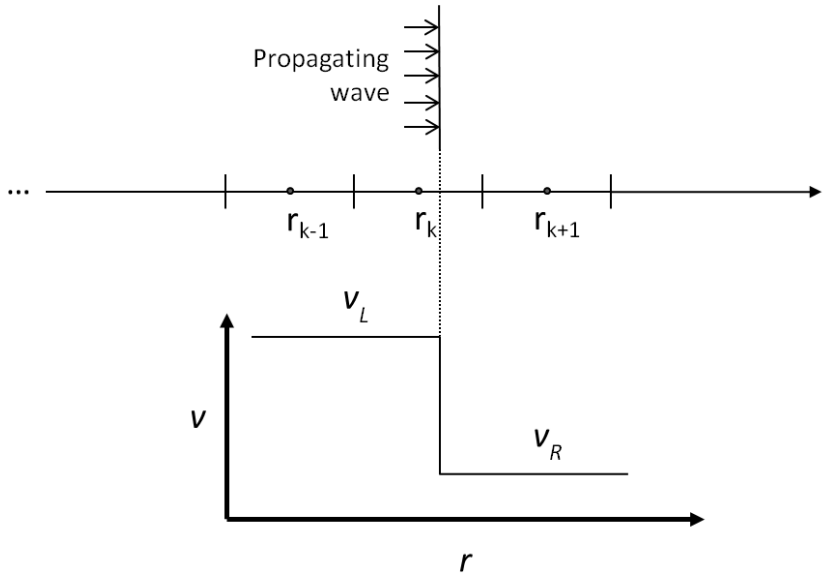

Figure 8: Propagation of a wave in the positive r direction. Sketch shows the flow field at a given instant of time.

6.3.1 *Godunov's method*

Assume that Eq. (6.1) represents a propagating wave as shown, for a fixed moment in time, in Figure 8. The velocity upstream of the wave is v_L and downstream of it is v_R. We are trying to evaluate the flux function, F, given by Eq. (6.21), at the cell interface $r_{k+\frac{1}{2}}$.

As was discussed in the previous section, due to the local Riemann problem, two possible values for variable ψ can be chosen at each interface $r_{k+\frac{1}{2}}$:

$$\psi_{k+\frac{1}{2}} = \begin{cases} \bar{\psi}_k \\ \bar{\psi}_{k+1} \end{cases} \tag{6.19}$$

However, due to the direction of propagation of the wave, point r_{k+1} has not yet felt the perturbation caused by the moving front, and thus approximating the flux using the values at this point will ignore the existence of the propagating wave all together. For this reason the flux at the interface should be approximated using $\bar{\psi}_k$. However, if the wave velocity, v, was towards the negative r direction (i.e. to the

left) then it would make sense to approximate the flux using $\bar{\psi}_{k+1}$. Therefore, it can be concluded that:

$$F_{k+\frac{1}{2}} = \begin{cases} F(\bar{\psi}_k) & , \quad v > 0 \\ F(\bar{\psi}_{k+1}) & , \quad v \leq 0 \end{cases} \tag{6.20}$$

Note that if $v = 0$, either of the approximations would be valid as there is no specific direction of propagation. Thus, inclusion of the equal sign in either of the approximations becomes arbitrary. The idea of calculating $F_{k\pm\frac{1}{2}}$ using Eq. (6.20) is often referred to as Godunov's scheme (LeVeque, 1992, p.136).

6.3.2 *Godunov-type scheme*

The flux function in the PDE, Eq. (6.1), can be assumed to take the form:

$$F(\psi) = \chi(\psi)\frac{\partial}{\partial r}\xi(\psi) \tag{6.21}$$

such that variable ξ is smooth for all values of ψ and χ is a discontinuous (and often nonlinear) function of ψ, in a such a way that it has different values on the left and right hand side of the discontinuity :

$$\chi(\psi) = \begin{cases} \chi_L & , \quad \psi > \psi^* \\ \chi_R & , \quad \psi < \psi^* \end{cases} \tag{6.22}$$

The reason for assuming this type of flux is that it directly relates to the MCMP problem of interest. In porous media flow systems, fluxes of this kind occur due to combinations of the mass conservation principle and Darcy's Law, where the relative permeability curves (e.g. Eq. (2.21)) are discontinuous and nonlinear functions of fluid saturations. This type flux functions can be observed in our governing equations Eqs. (2.17) (2.12) and (2.32).

It is worth mentioning that, the PDE in Eq.(6.1) is in the so called "conservative" form. Its non-conservative equivalent is:

$$\frac{\partial \psi}{\partial t} + \frac{\partial \chi}{\partial r}\frac{\partial \xi}{\partial r} + \chi \frac{\partial^2 \xi}{\partial r^2} = 0 \tag{6.23}$$

The use of the conservative form of the equations (LeVeque, 1992, p. 124) is particularly important when dealing with problems involving shocks or other discontinuities in the solution. A well known example is provided by Burgers' equation with discontinuous initial data, where the non-conservative representation fails dramatically in providing the correct solution (LeVeque, 1992, p. 34).

Therefore, flux function in kept at its conservative form. Note that for the approximation of the $\frac{\partial}{\partial r}\xi(\psi)\Big|_{k+\frac{1}{2}}$ term, ξ is a smooth for all values of ψ, therefore its derivatives are defined everywhere in the domain, meaning that its Taylor series expansion is valid at all locations. Hence, evaluation of this derivative can be carried out regardless of the upwind direction and purely from its Taylor series expansion. This is as opposed to the χ term, which bears a discontinuity and its Taylor series is valid on either side but not at the discontinuity; hence its requirement for upwinding. Thus the summary of our upwind scheme is as follows.

6.3.3 *Summary of the upwind scheme*

To summarise, the Godunov-type upwind scheme for evaluating the flux of the form $F(\psi) = \chi(\psi)\frac{\partial}{\partial r}\xi(\psi)$, is:

$$F_{k+\frac{1}{2}} = \left[v^u \chi^u_{k+\frac{1}{2}} + v^d \chi^d_{k+\frac{1}{2}} \right] \frac{\partial \xi}{\partial r}\bigg|_{k+\frac{1}{2}} \tag{6.24}$$

where $\frac{\partial \xi}{\partial r}\Big|_{k+\frac{1}{2}}$ is given by Eq. (**??**). $\chi^u_{k+\frac{1}{2}}$ and $\chi^d_{k+\frac{1}{2}}$ are given by Eqs. (**??**) and (**??**) respectively. v^u and v^d are given by:

$$v^u = \left(\frac{v+|v|}{2v+\epsilon}\right) \quad , \quad v^d = \left(\frac{v-|v|+\epsilon}{2v+\epsilon}\right) \tag{6.25}$$

v is the flow velocity and $\epsilon = 10^{-16}$ is the machine precision.

This scheme is of, at least, $O(l_k^2)$ accuracy, subject to conditions Eqs. (**??**) (**??**) and (**??**).

6.4 CONCEPTUAL MODEL

Our conceptual model consists of a fully penetrating well of radius r_W [L] situated at the center of a 2D, radially-symmetric reservoir of radial extent r_E [L], and formation thickness H_f [L]. The reservoir is surrounded by low permeability layers representing the cap rock. The system is initially filled with H_2O saturated with CH_4, at complete dynamic/thermodynamic equilibrium (Figure 9). CO_2 is then injected at a constant rate M_0 [LT^{-1}] for a period of time t [T]. The aim is to investigate, using numerical simulation, the thermal, pressure and compositional effects that develop as a consequence of injection of CO_2.

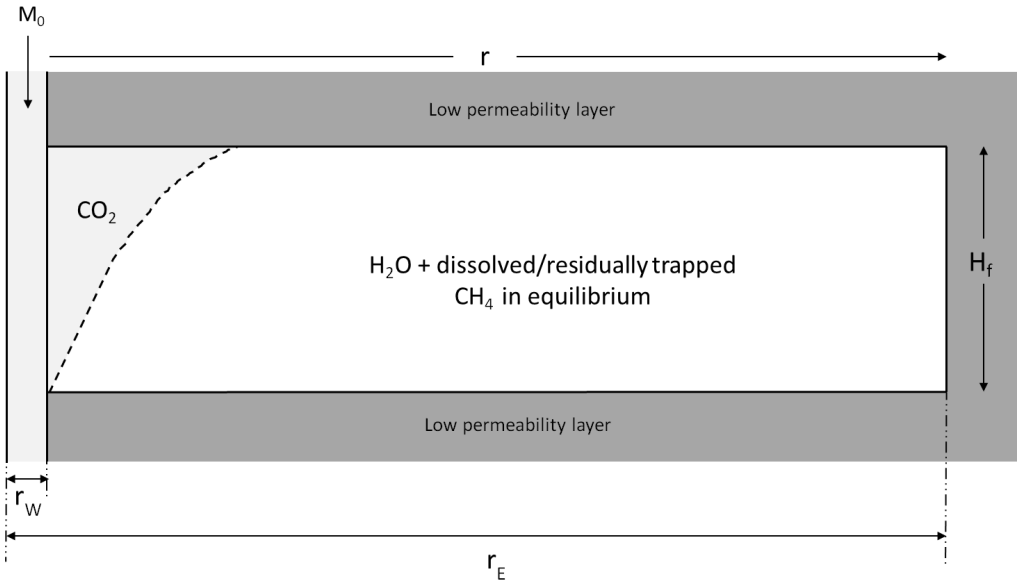

Figure 9: Schematic of our conceptual model.

6.5 NUMERICAL GRID

Since the system contains an injection well, in the horizontal direction,one would intuitively choose a numerical grid that is clustered more closely around the well, to capture the sharper flow gradients in this area, without having to refine the grid in the entire domain. We chose to use a logarithmically-spaced grid, which is also consistent with the fact that the flow being modelled is radial. The 1D numerical grid in the horizontal direction, from well-radius r_W to radial-extent r_E, is given by:

$$r_{k-\frac{1}{2}} = r_W e^{(k-1)\theta} \quad , \quad k = 1, 2, ..., N_r + 1 \tag{6.26}$$

where $r_{k-\frac{1}{2}}$ define the locations of the cell boundaries (see Figure 6), N_r is the number of cells and θ is given by:

$$\theta = \frac{1}{N_r} \ln\left(\frac{r_E}{r_W}\right) \tag{6.27}$$

The locations of the cell centers are then given by:

$$r_k = \frac{1}{2}\left(r_{k+\frac{1}{2}} + r_{k-\frac{1}{2}}\right) \tag{6.28}$$

6.5.1 *Jacobian pattern based on discretisation scheme*

Recall the definition of the Jacobian matrix from Eq. (6.7). Here, N (number of PDEs) could represent the number of discretised system of equations (i.e. number grid cells). In this context, by virtue of discretised equations, ψ_k (and therefore F_k) values could be mutually dependent on one another; for instance, conventional second-order finite volume approximation to the flux function F at cell k, will depend on three values, namely on cells $k-1$, k and $k+1$. Meaning that at any given time, the values of F will be unaffected by the perturbations outside of the range $[k-1,\ k,\ k+1]$ and therefore:

$$\mathbf{J} = \frac{\partial F_k}{\partial \psi_j} = 0 \qquad , \qquad k-1 > j > k+1$$

In this case, $\mathbf{J}$ will have dimensions $N \times N$ and is zero everywhere except at the three main diagonals of the matrix, giving rise to the well-known tridiagonal structure. In the case of three-component two-phase problem however, on the one hand, four PDVs (pressure, temperature and two out of three of the mass fractions) are solved simultaneously on N number of cells such that:

$$\mathbf{PDV} = \begin{bmatrix} \mathbf{P} \\ \mathbf{T} \\ \mathbf{z_1} \\ \mathbf{z_2} \end{bmatrix} \tag{6.29}$$

where:

$$\mathbf{P} = [P_1, P_2, ..., P_N]^T \tag{6.30}$$

$$\mathbf{T} = [T_1, T_2, ..., T_N]^T \tag{6.31}$$

$$\mathbf{z_1} = [z_{1(1)}, z_{1(2)}, ..., z_{1(N)}]^T \tag{6.32}$$

$$\mathbf{z_2} = [z_{2(1)}, z_{2(2)}, ..., z_{2(N)}]^T \tag{6.33}$$

On the other hand, due to the discretisation scheme used (see Eq. (6.24)) to evaluate the flux $F_{k\pm\frac{1}{2}}$, the range of dependency is $[k-1,\ k,\ k+1]$ and thus, the Jacobian matrix will take the from of block-tri-diagonal with dimensions $4N \times 4N$ (see Figure 10).

This Jacobian pattern was given as an input to the ode-solver at the start of the simulation for reduced simulation time, as was mentioned Section 6.2.5.

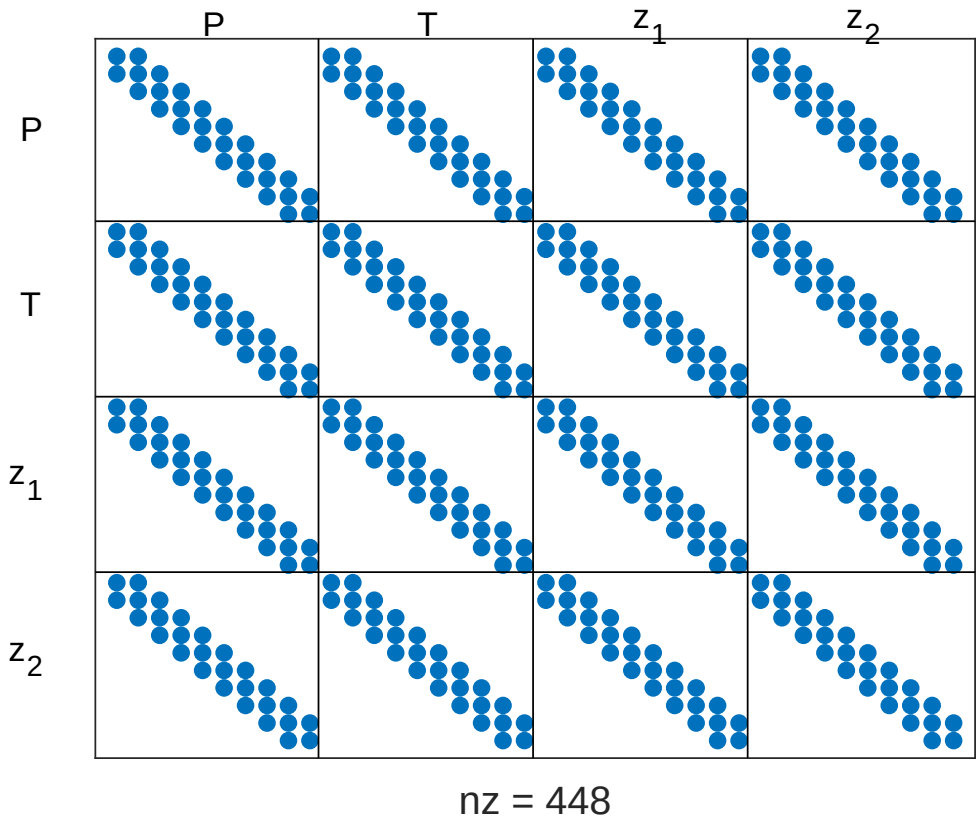

Figure 10: Block-tri-diagonal Jacobian pattern for the sparse system for N=10 cells and 4 PDVs (nz:number of nonzero elements represented by dots).

6.6 INITIAL AND BOUNDARY CONDITIONS

For three-component ($N_c = 3$) two-phase ($N_p = 2$) gas injection problem, the initial and boundary conditions are as follows:

$$
\begin{aligned}
& z_{CO_2} = 0, && r_W \le r \le r_E, && t = 0 \\
& S_1 = S_{1_0}, && r_W \le r \le r_E, && t = 0 \\
& P = P_0, && r_W \le r \le r_E, && t = 0 \\
& T = T_0, && r_W \le r \le r_E, && t = 0 \\
& T = T_0, && r = r_W, && t > 0 \\
& T = T_0, && r = r_E, && t > 0 \\
& H_{CO_2} = M_0/(2\pi r_W H_f), && r = r_W, && t > 0 \\
& H_{CH_4} = 0, && r = r_W, && t > 0 \\
& H_{H_2O} = 0, && r = r_W, && t > 0 \\
& H_{CO_2} = 0, && r = r_E, && t > 0 \\
& H_{CH_4} = 0, && r = r_E, && t > 0 \\
& H_{H_2O} = 0, && r = r_E, && t > 0
\end{aligned}
\tag{6.34}
$$

6.7 MODEL VERIFICATION

6.7.1 *Comparison to an analytical solution*

To be able to compare the numerical results with the analytical solution (described in Chapter 5), which is valid for constant temperature, here numerical simulation results will be first presented in the context of injection into the water-leg of a reservoir at constant temperature, and for two different cases of deep and shallow reservoirs. The effects of temperature will be shown in a separate section later on. The parameters used in this simulation are listed in Table 1.

Parameter (unit)	Deep	Shallow
P_0, initial pressure (MPa)	32	10
T, temperature (^{o}C)	85	45
M_0, injection rate (kg/s)	10	10
r_W, well radius (m)	0.25	0.25
r_E, radial extent (m)	20×10^3	$20\times\ 10^3$
ϕ, porosity (-)	0.2	0.2
k, permeability (m^2)	10^{-13}	10^{-13}
H_f, formation thickness (m)	100	100
k_{r1_0}, gas end-point relative permeability (-)	0.3	0.3
k_{r2_0}, liquid end-point relative permeability (-)	1	1
n_1, gas relative permeability exponent (-)	2	2
n_2, liquid relative permeability exponent (-)	2	2
S_{1_c}, critical gas saturation (-)	0.1	0.1
S_{2_c}, critical liquid saturation (-)	0.3	0.3

Table 1: Model parameters used for verification of the numerical simulation.

Figure 11 shows gas saturation profiles for CO_2 injection into shallow (Figures 11a and 11b) and deep (Figures 11c and 11d) reservoirs with 10% residual CH_4, during a simulation period of 1000 days with a constant mass injection rate of 10 (kg/s) which is equivalent to 0.315 Mt/year. The solid and the dashed lines represent results from the analytical and numerical solutions, respectively.

The high gas saturation around the injection well, often referred to as the dry-out zone (Mathias et al., 2011a), is due to the vaporization of the residual water saturation by the injected CO_2. A CH_4 bank with about 23% gas saturation in front of the CO_2 plume develops. The length of the CH_4 bank increases with time (note the logarithmic scale of the plots). Correspondence between the analytical solution and the numerical solution is very good for both gas phase saturation and pressure build-up. The numerical solution is seen to accurately locate the associated shock fronts while considering the partial miscibility of both CO_2 and CH_4 in H_2O.

Similar simulations but with different initial gas saturations are compared in Figure 12. It is found that the extent of the dry-out region is insensitive to the initial gas saturation. The extent of the dry-out region is smaller for the shallow reservoir and the volume of the gas plume is larger. The reduced dry-out region, in this case,

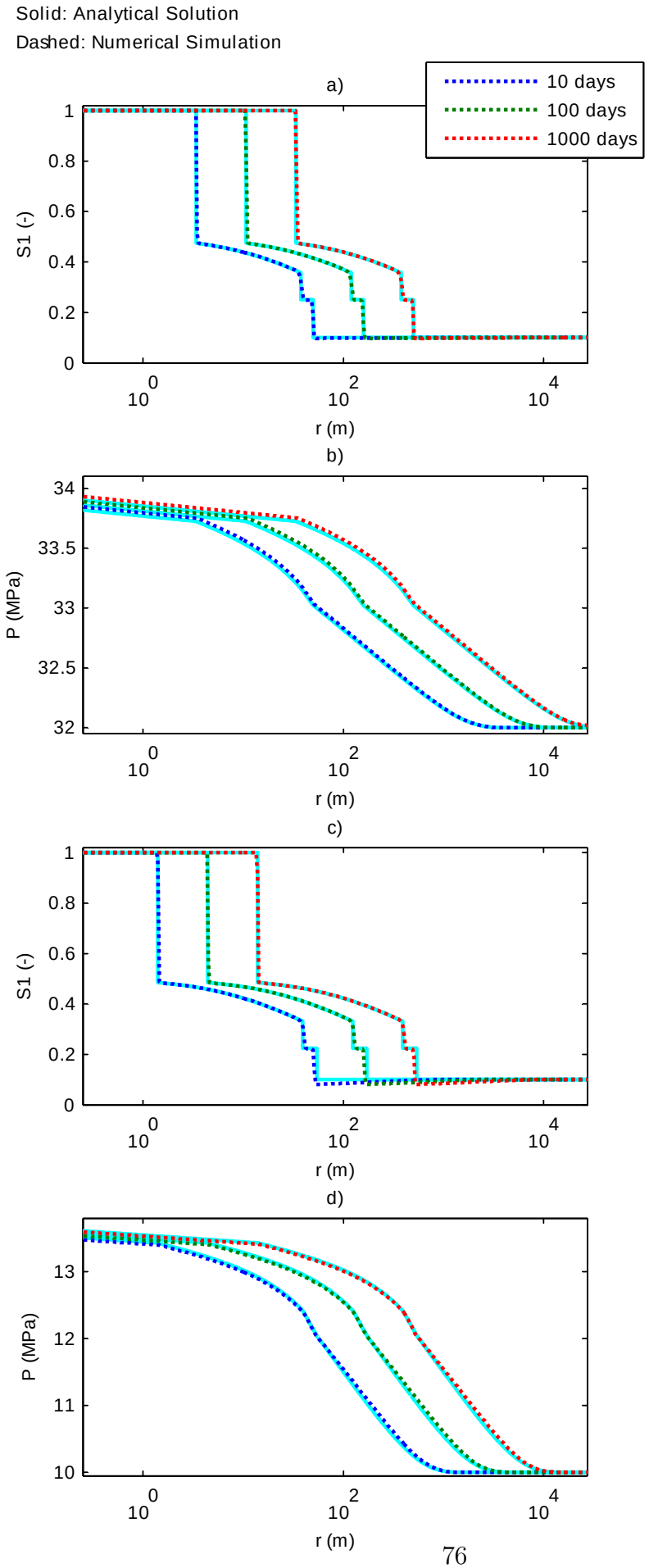

Figure 11: a) Comparison of gas saturation profiles between the analytical and numerical simulation of CO_2 injection into a deep reservoir with initial gas saturation, $S_{10} = 0.1$, after 10, 100 and 1,000 days. b) Corresponding pressure profiles for deep reservoir. c) Gas saturation profiles for a shallow reservoir. d) Corresponding pressure profiles for a shallow reservoir. A total of 600 cells were used for the numerical simulation.

is due to the reduced evaporation that occurs at cooler temperatures. The increased gas volume is due to the reduced gas density that occurs at lower pressures. Again it can be seen that the numerical solution is able to accurately predict the analytical results of Hosseini et al. (2012).

As is shown in Figures 11 and 12, numerical simulations of CO_2 injection into a reservoir containing CH_4 predict the accumulation of a CH_4 bank at the head of the CO_2 plume (Oldenburg & Doughty, 2011, Battistelli & Marcolini, 2009, Taggart, 2010). The system in discussion can be differentiated into three regions (Hosseini et al., 2012). These regions, starting from the injection point and moving outward, are:

1. a single-phase, dry-out region around the well-bore filled with pure CO_2.

2. a two-phase, two-component system containing CO_2 and H_2O.

3. a two-phase, two-component system containing CH_4 and H_2O.

Within the two-phase mixture, each phase propagates at a rate according to its mobility. The mobility of each phase varies from one region to another due to associated compositional changes. As a consequence, a trailing shock forms at the contact between regions (1) and (2) and a leading shock forms at the contact between regions (2) and (3).

The development of the CH_4 bank ahead of the CO_2 has been explained as follows (Taggart, 2010, Oldenburg & Doughty, 2011, Hosseini et al., 2012): as CO_2 is injected, it partitions into the gas phase and the aqueous phase. The initially dissolved CH_4 exsolves immediately, and is then pushed ahead of the growing CO_2 plume leading to the development of a CH_4 bank (Oldenburg & Doughty, 2011). Mathematically, the system is constrained to constantly enter and leave the two phase region along the tie-lines representing the injection and initial compositions, therefore the leading CH_4 bank is free from injected gas, CO_2 (Taggart, 2010).

Intuitively, it is expected that the amount of CH_4 initially present should affect the methane bank saturation i.e. the more the initial CH_4 saturation, the higher the

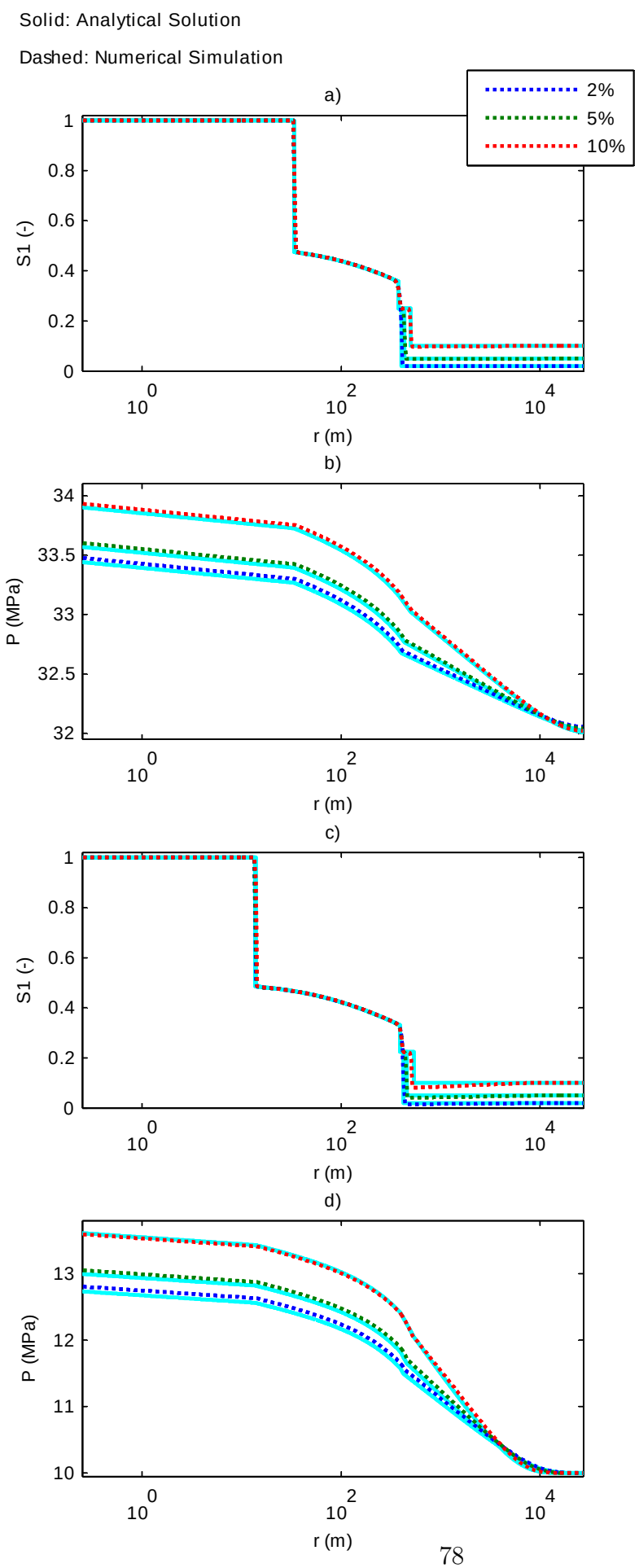

Figure 12: The same as Figure 11 but only showing profiles after 1,000 days and assuming initial gas saturations, S_{10}, of 0.02, 0.05 and 0.1.

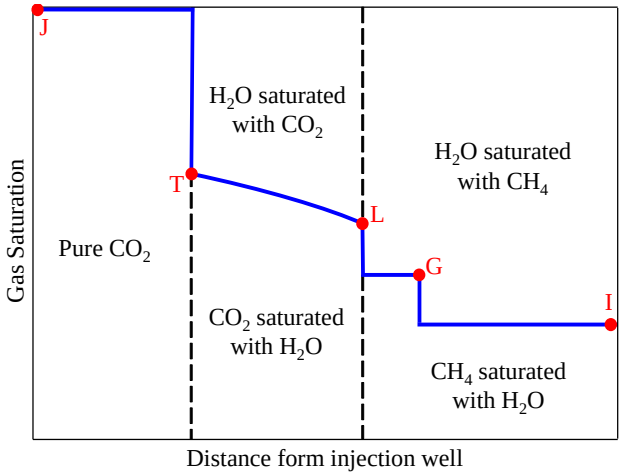

Figure 13: Schematic diagram illustrating the three-region system associated with CO_2 injection into a reservoir initially containing CH_4 and H_2O. **J**:Injection, **T**:Trailing Shock, **L**:Leading Shock, **G**:Gas Bank, **I**:Initial.

bank saturation. However, numerical simulation of CO_2 injection for different initial gas saturations (everything else being the same), show that the bank saturation is independent of the initial CH_4 saturation (see Figures 12 and 14). In fact, Hosseini et al. (2012) showed mathematically that the CH_4 bank saturation is independent of the initial gas saturation.

This can be further explained using the principles of fractional flow theory (Pope , 1980, Orr, 2007); because of the differences in phase viscosities in the two phase region (i.e. between mixtures of CO_2-H_2O and CH_4-H_2O), flow occurs on different fractional flow curves in the two phase region. Figures 14a, c and e show the fractional flow curves (plots of H_i/ρ_{i1} against G_i/ρ_{i1}) for CO_2 and CH_4 along with the locations of the shock fronts for different initial gas saturations.

The partial derivative $\partial H_i/\partial G_i$ represents the wave-velocity [1] of the system. The wave-velocities of the shock fronts are found from the gradients of straight lines that link the two conditions on either side of the shock. Fractional flow theory dictates that valid solutions should satisfy both the velocity constraint and the so-called entropy constraint (Orr, 2007, p. 51). The velocity constraint implies that wave velocity should always decrease with increasing distance from the injection boundary.

[1] Introduced in Sections 5.2 and 5.3.

The entropy constraint implies that the wave-velocity should be equal to the gradient of the fractional flow curve immediately upstream of the shock.

Therefore, on the one hand, due to the zero initial condition for G_1, the only valid path on the CO_2 fractional flow curve is a tangent (i.e., (0,0) to L). On the other hand, velocities must be equal at the contact between a pair of different fluids (Pope , 1980) (i.e. points G and L in Figure 13). This means that the gas bank saturation (point G) is dictated by the intersection of the tangent to the CO_2 curve with the CH_4 curve.

Figures 14b, d and f show the corresponding saturation profiles for different initial gas saturations. The level of saturation at point G is always determined by the tangent from (0,0) to point L. Physically, this implies that the bank saturation is only dependent on how fast the injected gas propagates. The solid and dashed lines in Figures 14b, d and f are from the analytical solution and numerical solution, respectively. There is an excellent correspondence between the two. The analytical solution was developed on the basis of the fractional theory described above. The numerical solution therefore further confirms the finding of Hosseini et al. (2012), that the CH_4 bank saturation is independent of the initial gas saturation.

6.7.2 *Grid convergence test*

The exact mass of injected CO_2 over the period of injection can be calculated using:

$$m = M_0 t \tag{6.35}$$

The mass in the domain can be calculated numerically using the following integral at a fixed time:

$$\bar{m} = 2\pi H_f \int_{r_W}^{r_E} r G_{CO_2} dr \tag{6.36}$$

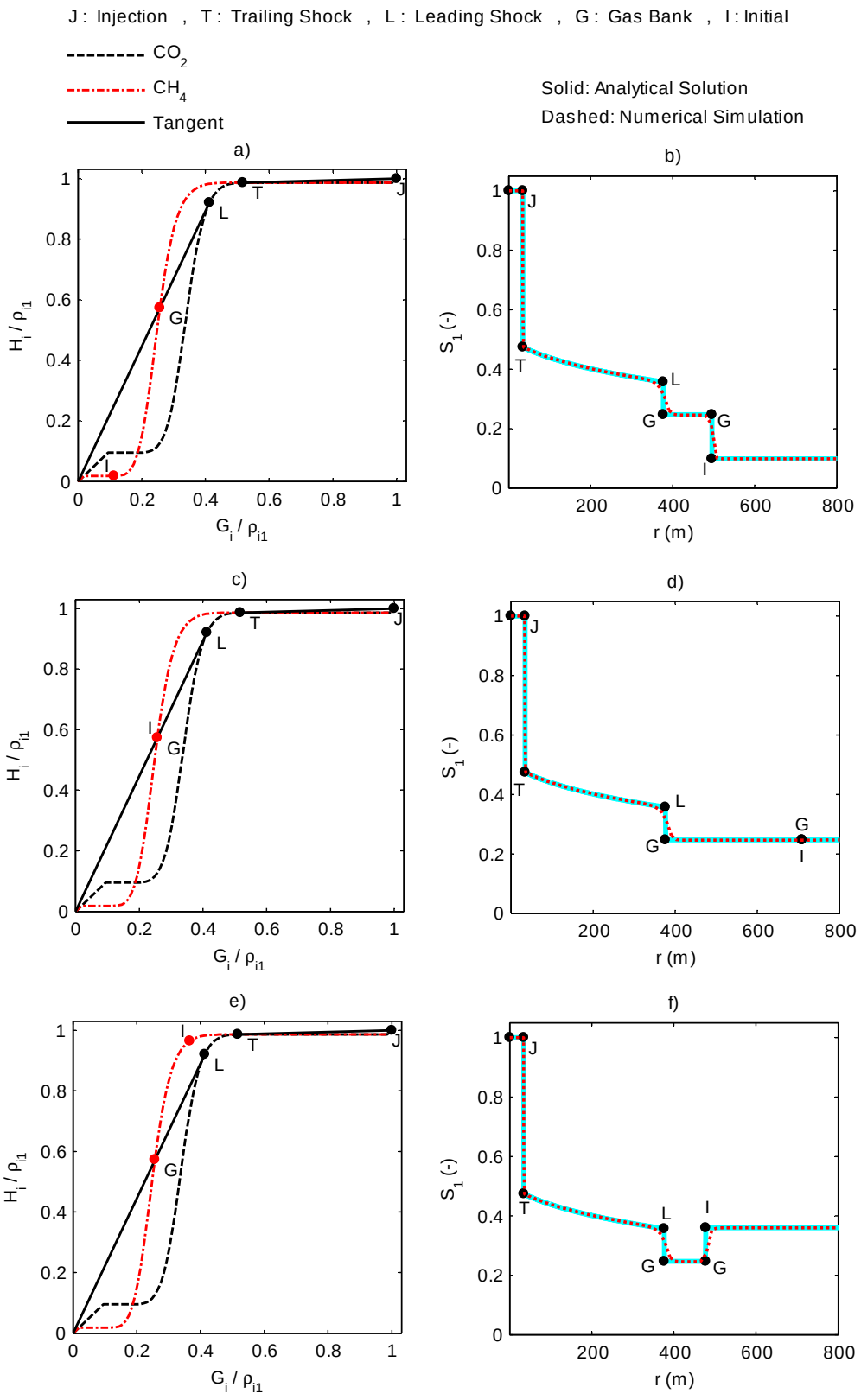

Figure 14: Illustration of CH_4 bank saturation independence of initial CH_4 mass fraction for the deep reservoir scenario after 1000 days of injection (with parameters as set in Table 1): a) and b) $S_{1_I} < S_{1_G}$, c) and d) $S_{1_I} = S_{1_G}$, e) and f) $S_{1_I} > S_{1_G}$.

It follows that the domain mass imbalance can be expressed using the following, to give an indication of mass conservativeness of the model:

$$Error = \frac{\bar{m} - m}{m} \times 100 \tag{6.37}$$

Mass error was monitored for each time. The mass error increases with time as is shown in Figure 15, however, as the grid is refined this error seems to converge to an acceptable value for all times. This is the reason why $N_r = 600$ cells was used in the numerical simulations in this chapter.

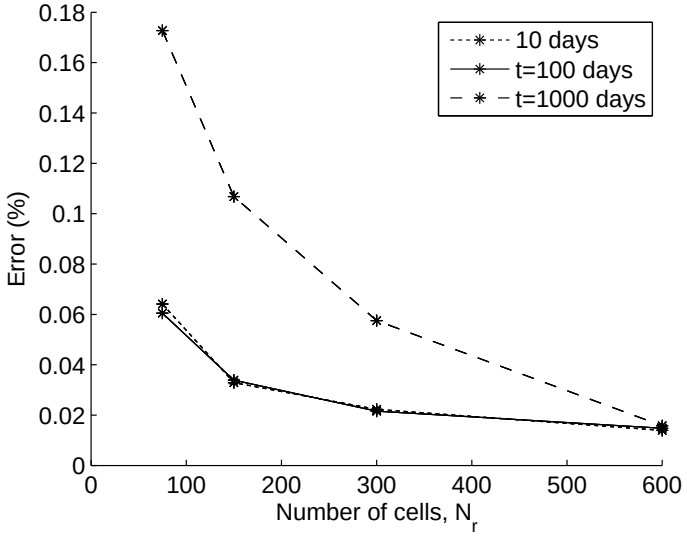

Figure 15: Percentage mass imbalance of CO_2 in the domain against the number of cells, N_r, at different times t=[10, 100,1000] days.

6.8 EFFECTS OF TEMPERATURE

Non-isothermal numerical simulations for injection into the water-leg of a shallow and deep reservoir were carried out using the parameters in Table 1 with constant injection temperature equal to initial reservoir temperature. Figure 16 shows temperature distributions at different times for both cases of shallow and deep reservoirs. The saturation and pressure profiles were identical to the isothermal cases (Figure 11) and therefore are not shown here.

Note that the thermal front is generally behind the CO_2 plume as a result of heat retardation associated with the high specific heat capacity of the host rock and resident water. In both cases, near the injection point, temperature declines with increasing distance and some distance away it recovers back to its initial value. The temperature decline occurs due to the expansion of the CO_2 as it migrates away from the injection well and experiences continuously decreasing pressures.

Given the magnitude of the temperature change (<1 ^oC) in both cases, it can be understood why the isothermal and non-isothermal pressure and gas saturation profiles were identical. It can therefore be concluded that for this pressure range (> 10 MPa) the temperature effects are negligible.

6.9 EFFECTS OF GRAVITY

All the numerical simulations so far have been in 1D radial coordinate. However, to investigate the significance of gravity in this context, a 2D radial model was developed. Figure 17 is a schematic of the 2D numerical grid where the dots represent the cell centers and the solid lines are the cell boundaries. In the horizontal direction, the cells are clustered logarithmically around injection point. In the vertical direction, uniform spacing was used.

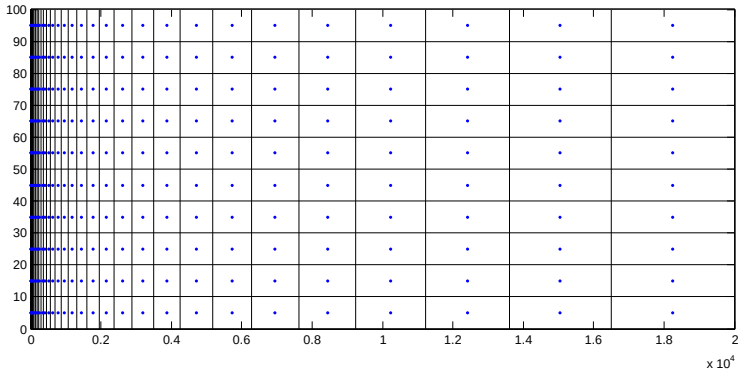

Figure 17: Schematic of 2D numerical grid. Dots represent the location of the cell centers and solid lines define the boundary of each cell.

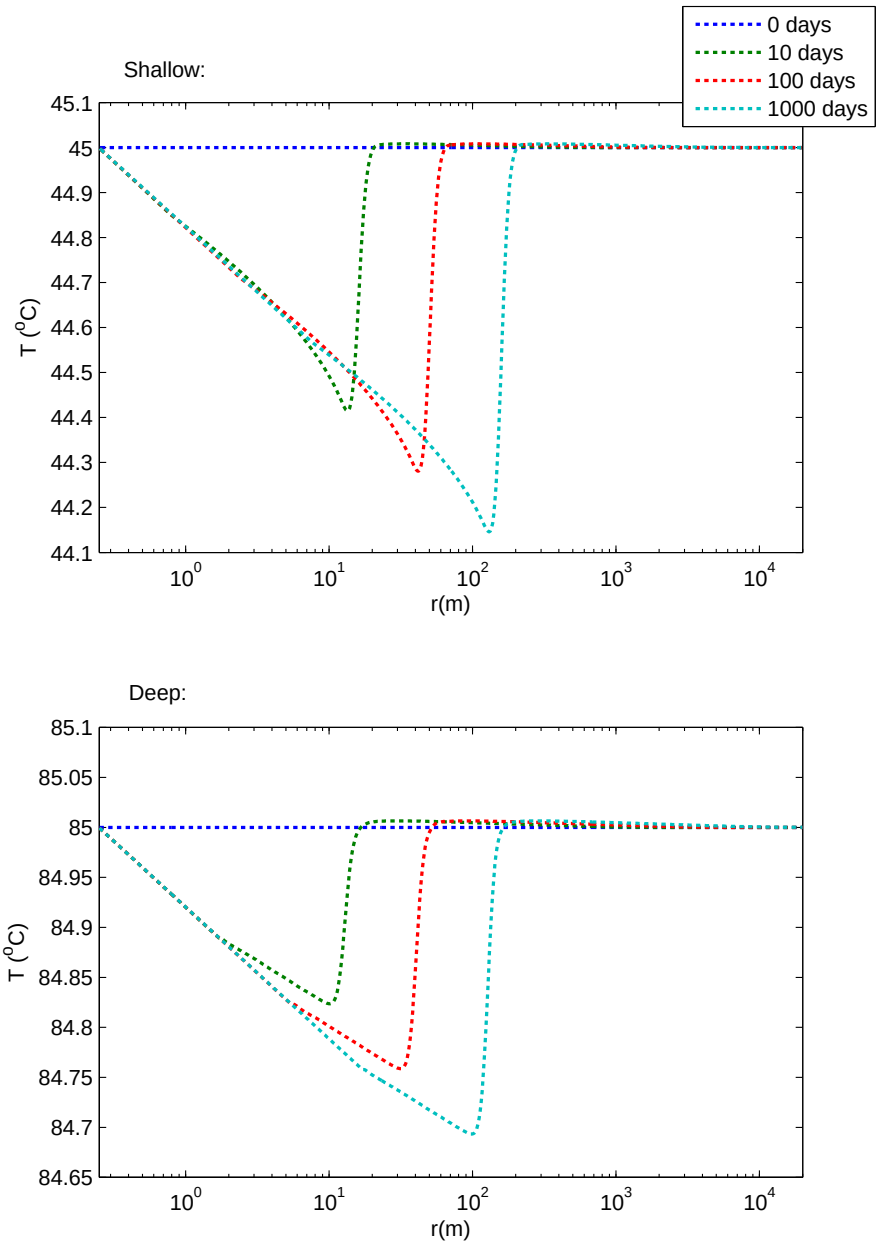

Figure 16: Temperature profiles for the shallow and deep reservoirs at different times t=[0, 10, 100,1000] days.

As in the previous section, numerical simulations were conducted for both cases of shallow and deep reservoirs using the parameters in Table 1. $N_z = 20$ cells in vertical direction and $N_r = 600$ cells in the horizontal direction were used. The results of simulation of CO_2 injection into the shallow and deep water-leg of a reservoir are presented in Figures 18 and 19 respectively. For both scenarios, gas saturation and pressure profiles are shown at different times.

From the pressure plots, it can be seen how the injection process is pressuring up the reservoir in time. After 1000 days, the plume seems to have spread considerably more in the shallow case than the deep case. This can be attributed to the higher pressure in deep-reservoir case which tend to compress the plume and limit its spreading. Contrary to plume spreading, the extent of the dry-out zone is larger in the deep case than in the shallow case. This is due to solubility-limit of water in the CO_2 phase being higher at higher pressures, meaning that the injected gas can evaporate more of the resident brine around the well.

The CO_2 plume is still almost vertical after 10 days, but it starts rising to the top of the formation as the buoyancy forces begin to dominate. The mobilised methane bank can be observed ahead of the plume, accumulated in the lowest-pressure part of the domain, and is shrinking in size with time as the pressure increases (since brine is almost incompressible).

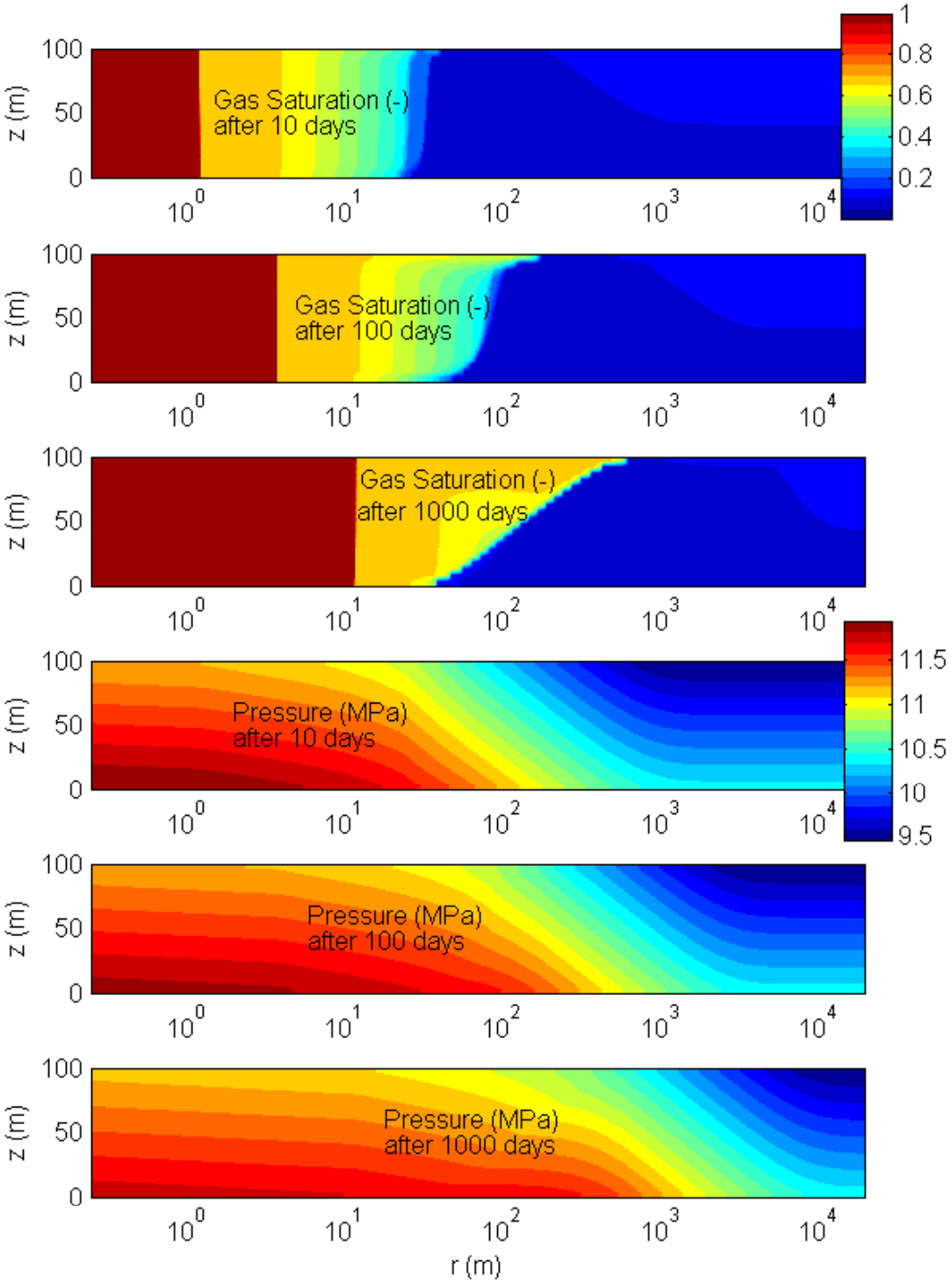

Figure 18: Results of 2D radial numerical simulation of CO_2 injection into the water leg of a shallow reservoir with initial gas saturation $S_{10} = 0.1$, for different times.

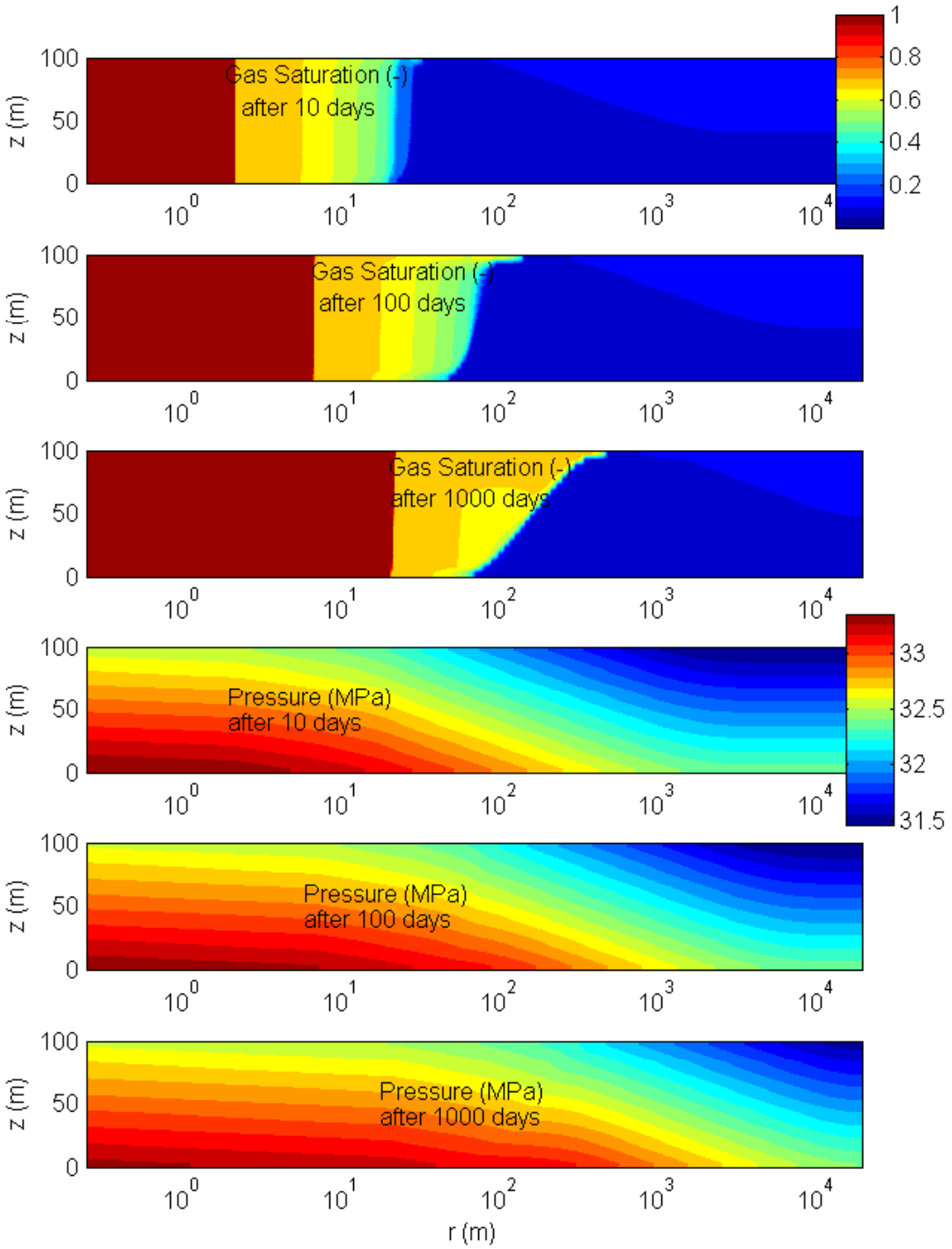

Figure 19: Results of 2D radial numerical simulation of CO_2 injection into the water leg of a deep reservoir with initial gas saturation $S_{10} = 0.1$, for different times.

There are no analytical solutions in the literature for the 2D case. However, if we were to vertically average the 2D results, we could then compare them to that of the analytical solution described in Chapter 5. Thus, the 2D results were vertically-averaged and plotted against the 1D analytical solution (see Figure 20), which is essentially a vertically-averaged model with the assumption of zero-gravity. The vertically-averaged pressure plots generally match closely with the analytical solution. The gas saturation plots on the other hand, only match the analytical solution for early times, i.e., before the onset of significant buoyancy flow.

For further investigation, numerically integrating the area under both vertically-averaged and analytical saturation curves, revealed that the amount of gas in the domain is exactly the same, as is expected due to conservation of mass principle on which both models are based. However, Figure 20 suggests that the gravity tends to smear-out the sharp fronts in a diffusion-like manner. In fact Nordbotten & Celia (2006) showed that vertical-averaging in presence of gravitational forces, introduces an additional diffusive term to the Darcy's flux of each of the phases, which is the cause of the deviation from the analytical solution (as it assumes zero gravity).

Furthermore, to investigate the effect of gravity on CH_4 recovery, 2D plots of CH_4 mass fraction in the mobile gas phase (where $S_1 > S_{1c}$), X_{21}, are shown for shallow and deep cases in Figures 21 and 22 respectively. The red arrows represent velocity vectors of the gas phase and the white arrows are velocity vectors of the liquid phase. The regions of high CH_4 concentration are colored in dark red where the gas phase is almost pure methane. In both cases, the methane bank is almost vertical at early times, then it starts rising due to buoyancy effects. It seems that the methane bank ahead of the CO_2 plume is fading over time.

The evolution of the CH_4 bank can be explained as follows: as CO_2 is injected, it evaporates all the water around the well, thus mobilising the initially dissolved and residually-trapped methane. Owing to it being the lightest component, CH_4 then travels faster and accumulates ahead of the CO_2. However, due to significant density

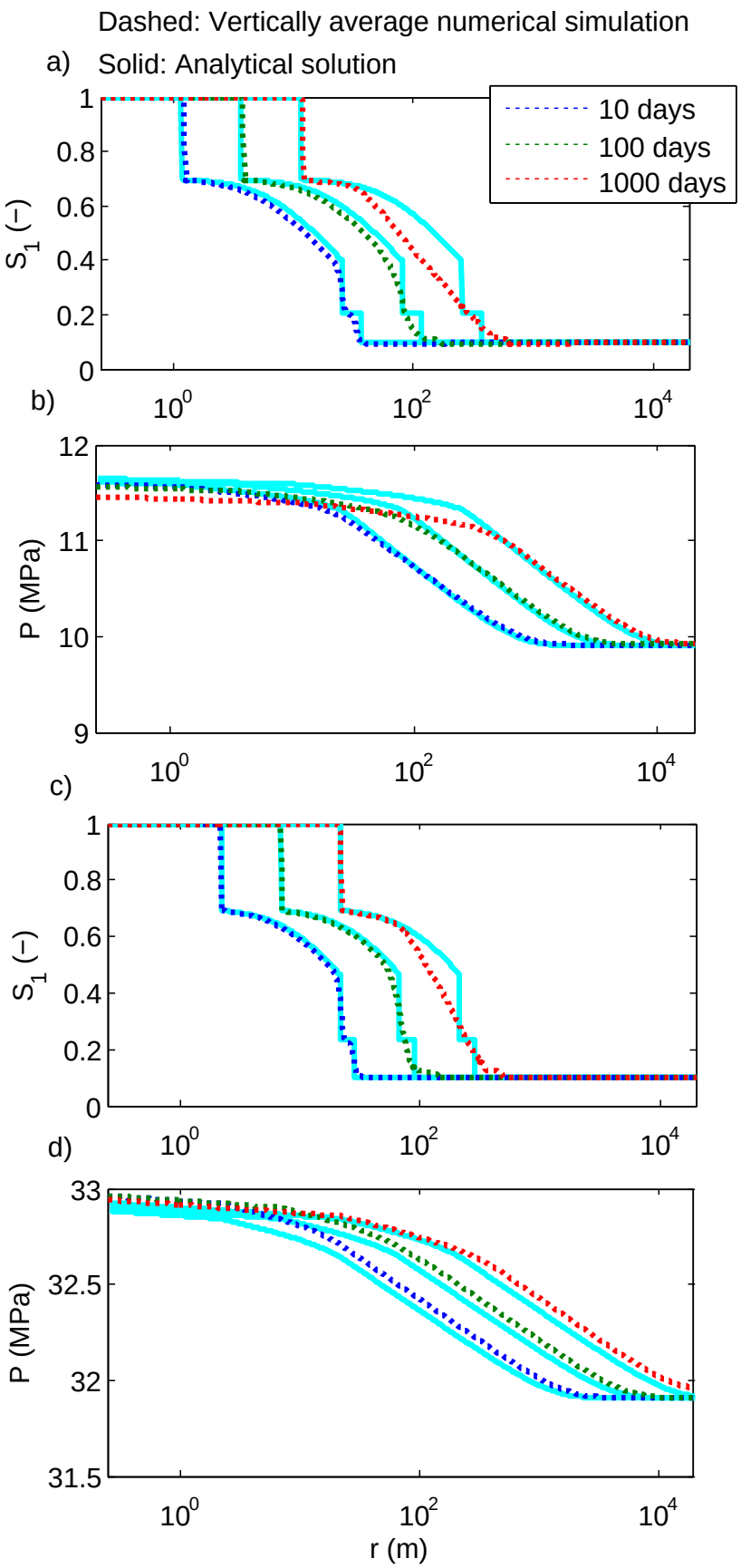

Figure 20: Comparison between the 1D analytical and 2D vertically-averaged numerical gas saturation and pressure profiles after [10, 100, 1000] days and assuming initial gas saturations, S_{10}, of 0.1.

differences, CH_4 quickly rises to the top of the formation. During this process, it is replaced by the fresh reservoir water from below, which will residually trap some of the mobilised gas. In other words, CH_4 is being mobilised due to injection of CO_2, and at the same time being trapped due to upward/downward motion of the gas/liquid phases.

Furthermore, mass of mobilised methane can be numerically calculated using:

$$m_{_{CH_4}} = 2\pi\phi \int_0^{H_f} \int_{r_W}^{r_E} r\rho_1 X_{21} S_1^* \, drdz \tag{6.38}$$

$$S_1^* \approx S_1 \qquad \text{where} \qquad S_1 > S_{1c} \tag{6.39}$$

Figures 21(d) and 22(d) show the amount of mobile methane in the domain in mega tonnes (Mt). It confirms that the mass of mobile methane initially increases, and then it starts decreasing, as a result of residual entrapment of the gas, driven by buoyancy induced flow.

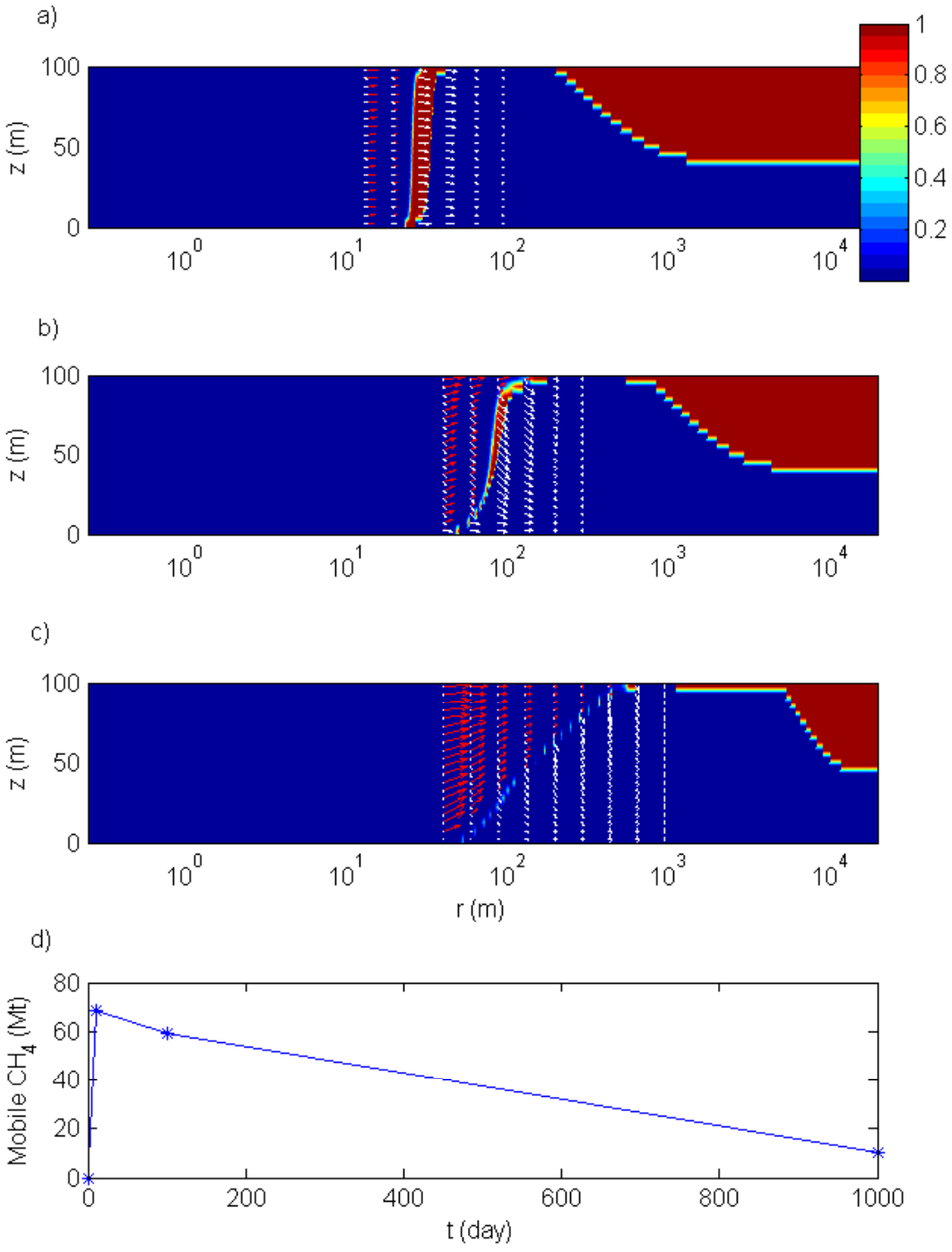

Figure 21: a) b) and c) are the mass fraction of CH_4 in the mobile gas phase ($S_1 > S_{1c}$). d) is the mass of mobile methane in the domain in mega tonnes. Red arrows are the velocity vectors of the gas phase and the white arrows are the velocity vectors of the liquid phase. These results are for the case of shallow reservoir.

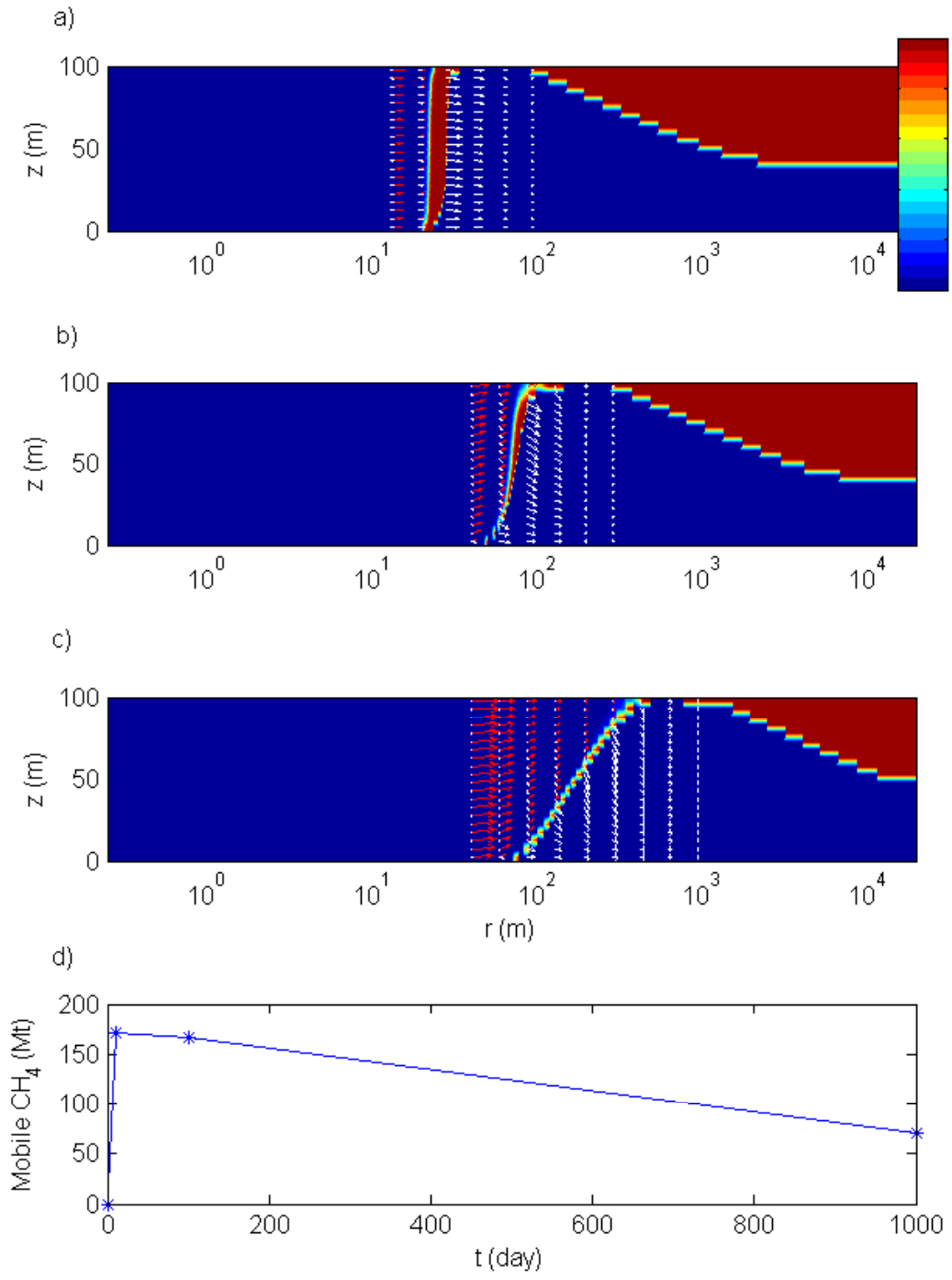

Figure 22: a) b) and c) are the mass fraction of CH_4 in the mobile gas phase ($S_1 > S_{1c}$). d) is the mass of mobile methane in the domain in mega tonnes. Red arrows are the velocity vectors of the gas phase and the white arrows are the velocity vectors of the liquid phase. These results are for the case of deep reservoir.

In short, buoyancy seems to have a significant adverse effect on the gas recovery potential for injection into the water-leg of a gas reservoir and should not be neglected in this case.

It is worth mentioning that, for injection into the gas-leg of a reservoir, where water is present only as a residual phase, the buoyancy effects could potentially be much less significant, as the contact between water and CH_4 is minimal (or zero in the case of a dry-gas reservoir), thus avoiding excessive buoyancy-induced residual-entrapment of the mobile methane. This will be tested in the next chapter.

6.10 SUMMARY OF THE FINDINGS

In this chapter, we have developed a numerical model based on the so called Method of Lines (MOL) technique, to model the two-phase three-component flow problem in the context of CO_2 injection into deep (P=32 MPa, T=85 ^oC) and shallow (P=10 MPa, T=45 ^oC) water-leg of a reservoir initially only containing CH_4+H_2O.

Numerical simulation results predict accumulation of a CH_4 bank ahead of the CO_2 plume which confirms the findings of Oldenburg & Doughty (2011), Battistelli & Marcolini (2009) and Taggart (2010). The numerical solution is seen to accurately locate the associated shock fronts while considering the partial miscibility of both CO_2 and CH_4 in H_2O.

As CO_2 is injected, it partitions into the gas phase and the aqueous phase. The initially dissolved CH_4 exsolves immediately, and is then pushed ahead of the growing CO_2 plume leading to the development of a CH_4 bank. Mathematically, the system is constrained to constantly enter and leave the two phase region along the tie-lines representing the injection and initial compositions, therefore the leading CH_4 bank is free from the injected gas, CO_2.

Counter-intuitively, numerical simulation of CO_2 injection for different initial gas saturations (everything else being the same), show that the level of bank-saturation

is independent of the initial CH_4 saturation, which also confirms the findings of Hosseini et al. (2012).

Non-isothermal simulations show that the thermal front is generally behind the CO_2 plume as a result of heat retardation associated with the high specific heat capacity of the host rock and resident water. In both cases of deep and shallow reservoirs, near the injection point, temperature declines with increasing distance and some distance away it recovers back to its initial value. The temperature decline occurs due to expansion of the CO_2 as it migrates away from the injection well and experiences continuously decreasing pressures. However, the very small magnitude of the temperature change suggests that, at least for the pressure ranges considered here, temperature can safely be assumed constant in future simulations.

Moreover, to investigate the significance of gravity in this context, a 2D radial model was developed. The 2D results show that as CO_2 is injected, it evaporates all the water around the well, thus mobilising the initially dissolved and residually-trapped methane. Owing to it being the lightest component, CH_4 then travels faster and accumulates ahead of the CO_2. However, due to significant density differences, CH_4 quickly rises to the top of the formation. During this process, it is replaced by the fresh reservoir water from below, which will residually trap some of the mobilised gas. In other words, CH_4 is being mobilised due to injection of CO_2, and at the same time being trapped due to upward/downward motion of the gas/liquid phases.

Furthermore, comparison of the vertically-averaged 2D results to the 1D analytical solution suggests that gravity tends to smear out the sharp fronts in a diffusion-like manner, confirming the findings of Nordbotten & Celia (2006) who show that vertical averaging in presence of gravitational forces, introduces an additional diffusive term to the Darcy's flux of each of the phases.

7

EGR IN THE NORTH MORECAMBE FIELD

In this chapter, the numerical model described in Chapter 6, will be used to simulate CO_2 injection into the very low-pressure (0.82 MPa) North Morecambe gas field, in east Irish Sea, to provide an estimation of the Enhanced Gas Recovery (EGR) potential in this field.

7.1 INTRODUCTION

Carbon Capture and Storage (CCS) is considered as an important potential solution for CO_2 emission reduction within the framework of the Kyoto Protocol (Haszeldine, 2009). Yet, CCS requires CO_2 to be stripped off the flue gas at the power plant. Separation of CO_2 from the flue gas is highly costly, consuming at least 10% of the electricity generated by a power plant (David & Herzog, 2000). Furthermore, additional costs are associated with injection of a highly corrosive gas such as CO_2 (Bergman et al., 1997). Capture and injection of CO_2 into geological formations will therefore be more attractive if the process could provide economic incentives, such as additional hydrocarbon production, to offset the high costs associated with CCS, which leads to the idea of injecting the CO_2 into depleted hydrocarbon reservoirs.

Hydrocarbon reservoirs, compared with other geological formations suitable for CO_2 storage, have advantages associated with better levels of characterization, due to available static geological and dynamic production history data. Additionally, reduced uncertainty related to cap rock integrity is demonstrated through containment of hydrocarbon products over geological time scales (Loizzo et al., 2010). Depleted gas

reservoirs have the added benefit of having a much more compressible reservoir fluid (methane+water as opposed to oil+water) along with significantly lower abandonment pressures (less than 1 MPa) (Mathias et al., 2014), such that, CO_2 storage capacities of natural gas reservoirs around the world have been estimated to be up to 13 times higher than that of saline aquifers of comparable sizes (Barrufet et al., 2010). Thus, in order to offset the high cost of CCS, enhanced oil/gas recovery (EOR/EGR) can be considered in various fields around the world.

The implications of injecting CO_2 into oil reservoirs for Enhanced Oil Recovery (EOR), have been broadly investigated in both academia and industry (Metz et al., 2005, Quintella et al., 2010, Sweatman et al., 2011). Injection of CO_2 for Enhanced Gas Recovery (EGR) however, despite being attractive to many countries with gas reserves, has not been investigated in any depth (Blok et al., 1997, Oldenburg et al., 2001). This is attributed to the high recovery factor of gas reservoirs by natural pressure drive and concerns regarding degradation of the natural gas due excessive mixing with the injection fluid (Stevens et al., 2001). Indeed, there are no commercial scale projects and only a few demonstration EGR projects in practice until now, the most well-known of which are the K12-B project in the Netherlands (Van der Meer et al., 2005), the CLEAN project in Germany (Kuhn et al., 2012) and the Alberta project for coal-bed methane recovery in Canada (Mavor et al., 2004). As a result, numerical simulation remains one of the main tools for studying the EGR processes. Accordingly, in this chapter, the compositional reservoir simulator discussed in Chapter 6 is used to simulate CO_2-EGR in the Centrica Plc's North Morecambe gas field (located in the Irish Sea Basin), and to provide an estimation of the incremental gas recovery potential in this field as a consequence of CO_2-EGR. Incremental gas recovery here is referred to as the amount of additional gas recovered, which would not have been, had it not been for CO_2 injection.

Structure of this chapter is as follows. The case study reservoir is introduced. A literature review of the previous numerical simulation work concerning the application

of CO_2-EGR to various gas fields is presented. Our previously published reservoir simulator that was used to simulate the case study reservoir is introduced. The model calibration procedure that was undertaken to better fit the simulator to the available production history data is discussed. Numerical simulations are then performed and the results discussed, in the context of CO_2 injection into the North Morecambe field. Finally, an economic feasibility study is performed based on the simulated gas recovery potential, global CH_4 prices, offshore drilling costs, CO_2 supply cost and UK's Carbon Price Floor (CPF), followed by summary and conclusions.

7.2 THE NORTH MORECAMBE GAS FIELD

The North Morecambe gas field is located in the East Irish Sea basin (see Figure 23). It initially contained 36.5 BSCM (billion standard cubic meters) of natural gas. The structure is fault closed on three sides and dip closed to the north, as is shown schematically in Figure 24. Development was by ten conventionally drilled wells (see Fig. 25). Thin Sherwood Sandstone dominates flow into the well bore. Platy illite reduces the permeability by two to three orders of magnitude in the lower illite-affected zone of the reservoir. The maximum gas column is about 975 feet (298 m). Around 56% of the Gas Initially In Place (GIIP) was estimated to be contained in the high permeability illite-free zone. Table 2 is a summary of the North Morecambe field properties (obtained from Cowan & Brown (2003)) and Figure 26 shows the production history over the course of 21 years, starting from October 1995.

Based on the mean monthly production rate, i.e., 114.3 (MSCM/month), spanning over 21 years, the volume of gas produced from this reservoir can be estimated as:

$$V_{Prod.} \approx 114.3 \times 12 \times 21 \approx 28.8 \text{ (BSCM)} \tag{7.1}$$

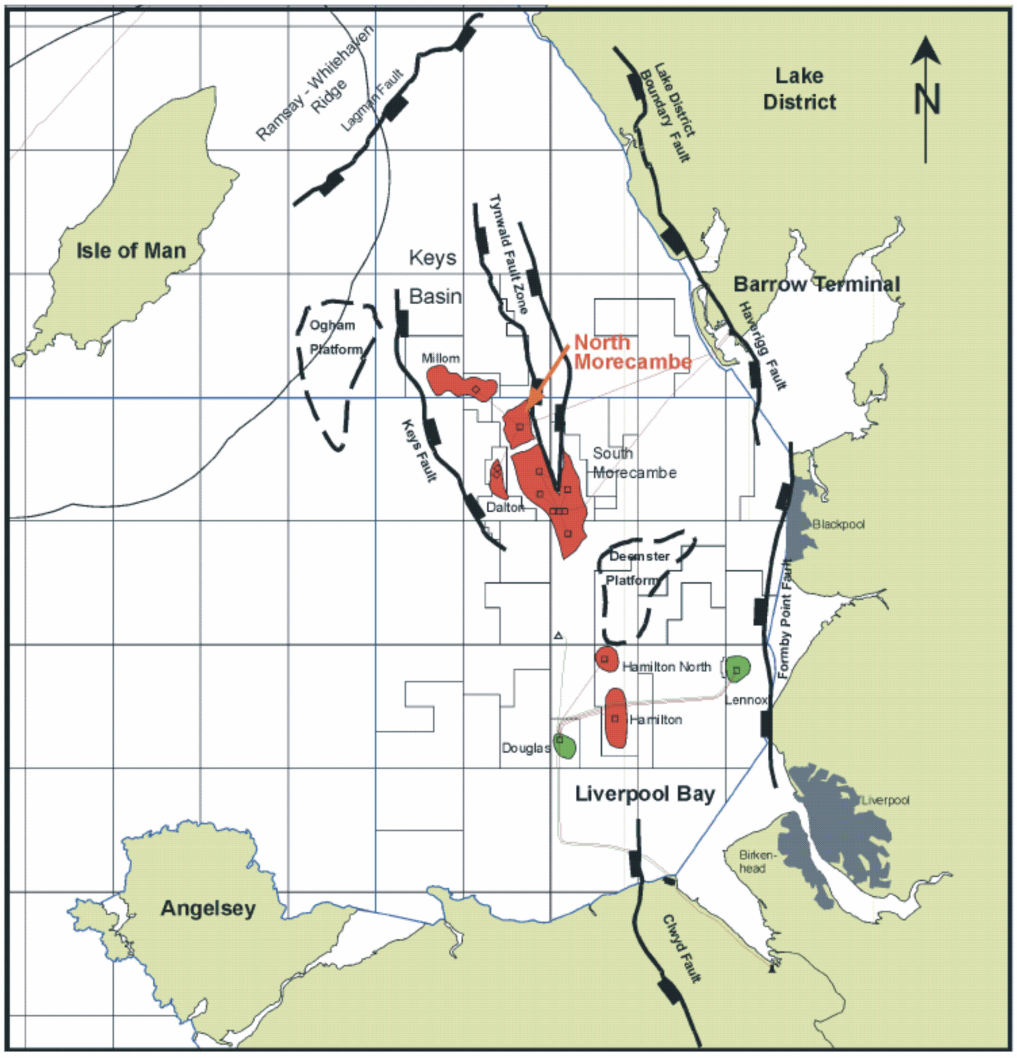

Figure 23: Location of north Morecambe gas field and its structural elements (taken from Cowan & Brown (2003)).

Given the estimated Gas Initially in Place (GIIP) of 36.5 BSCM, upon cessation of production the remaining gas in the reservoir would be as follows:

$$V_{Res.} \approx 36.5 - 28.8 \approx 7.7 \text{ (BSCM)} \tag{7.2}$$

Despite very low permeability of the illite-affected layer, over time some of the gas in this layer will have migrated upwards to the permeable layer due to the pressure difference between them. Whether or not the amount of leaked gas is significant, would be interesting to further investigate. However, in this study, only the worst case scenario is considered, where the amount of leaked gas from the impermeable

layer is assumed insignificant. In this way our estimations provide a lower bound for the EGR potential in this field.

Nevertheless, most of the remaining gas is expected to reside in the illite-affected layer, and therefore not recoverable due to very low absolute permeability. However, even a modest portion of the remaining gas residing in the illite-free layer (i.e. recoverable), could still be a significant contribution to the field's reserves. Yet, due to reservoir the pressure being as low as 0.82 MPa, it has not been possible to produce the recoverable portion of the remaining gas by means of primary recovery techniques and at an economic rate. Therefore, secondary recovery techniques such as EGR are worth considering for this field, in order to obtain incremental gas recovery, while extending the field's life and deferring the high costs associated with abandonment.

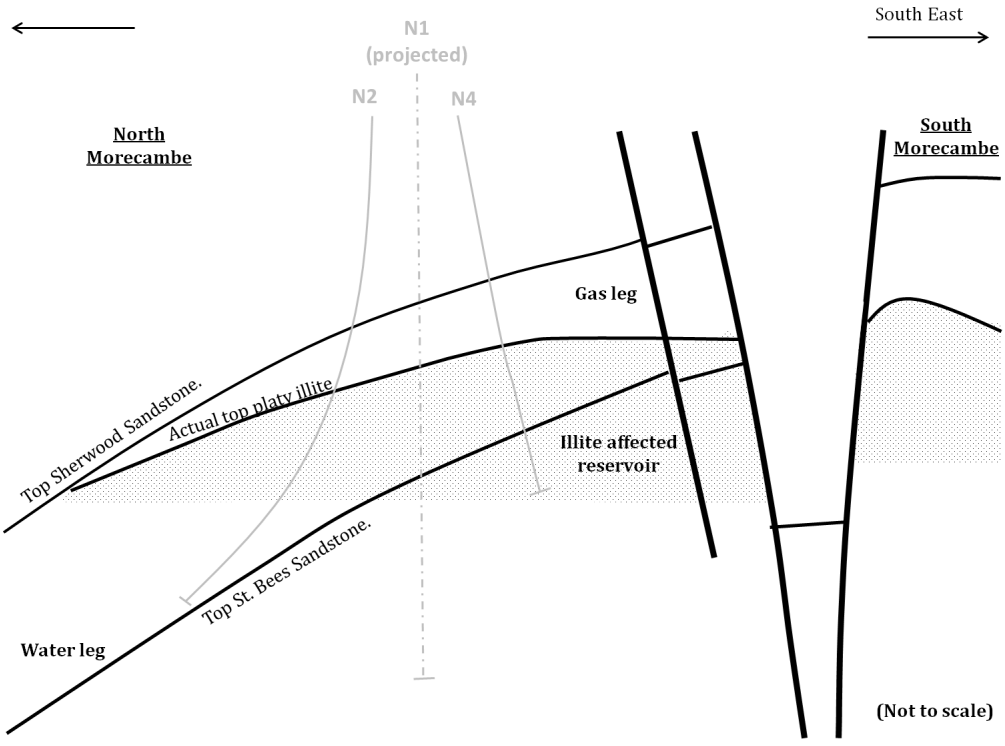

Figure 24: Schematic of the North Morecambe gas field (taken from Cowan & Brown (2003)), to be looked at in conjunction with Figure 25).

The aim of this chapter is therefore, to use numerical simulation to estimate the incremental gas recovery potential due to CO_2 injection and to investigate the economic feasibility of CO_2-EGR in this field.

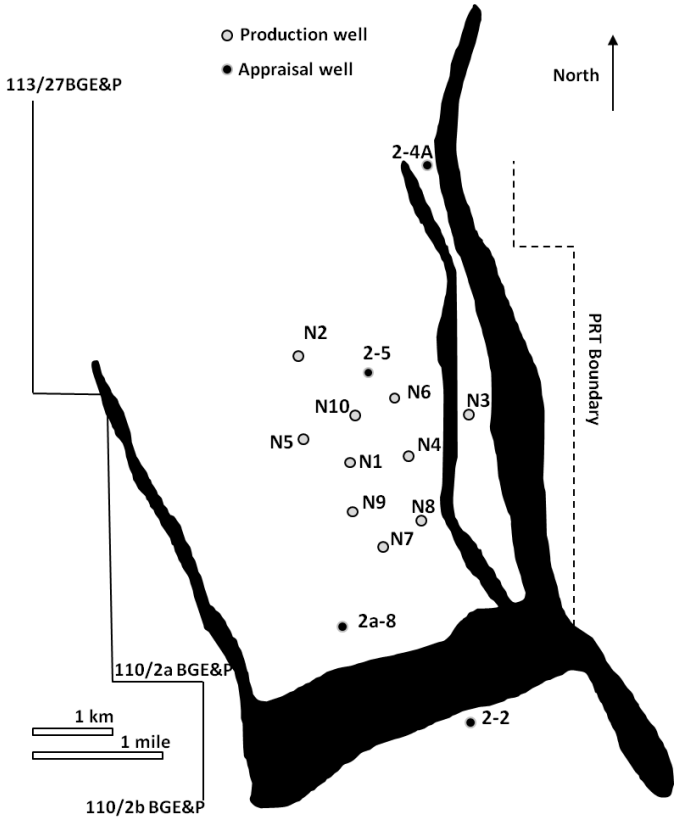

Figure 25: Plan view of the North Morecambe gas field (taken from Cowan & Brown (2003)), showing the existing well positioning relative to the faults locations.

7.3 PREVIOUS NUMERICAL SIMULATION WORK

The first published numerical simulation results regarding the application of CO_2-EGR was by Van der Burgt et al. (1992), where they considered injection into a five-layer dipping reservoir. Their results suggested only a limited gas recovery due to early breakthrough of CO_2. Later, Blok et al. (1997) simulated EGR in the context of hydrogen production, where the CH_4 is primarily used to produce hydrogen for fuel-cell applications, with CO_2 being a by-product of this process which can be re-injected into the reservoir. According to Blok et al. (1997), the incremental cost of produced hydrogen (i.e., for CO_2 compression, transport, injection and storage) would be about 7% compared with the case where CO_2 is vented to the atmosphere. However, their numerical results suggest that CO_2 injection leads to enhanced CH_4

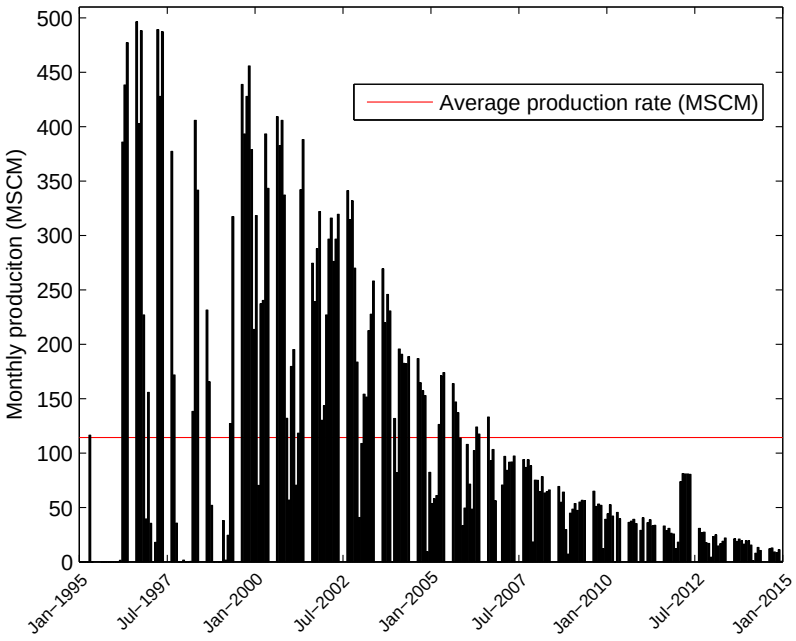

Figure 26: Production history of the North Morecambe gas field, taken from the website of the Department of Energy and Climate Change (DECC, 2016). MSCM: million standard cubic meters. A dramatic decline in the production rate can be observed which is due to significant pressure drop in this field. Field pressure has dropped to 0.82 MPa from the initial 12.41 MPa.

recovery, as a consequence of reservoir repressurisation, which in turn reduces the incremental cost to only 2%. Oldenburg et al. (2001) presented numerical simulation of CO_2-EGR in the Rio Vista gas field in California. They assumed a 2D reservoir and simple gas mixing relations. They forecasted that injection of CO_2 would produce approximately five times the projected amount of the primary-production over the next twenty years. Focusing on injection scenarios, Clemens & Witt (2002) numerically simulated five different injection strategies to investigate the effect on methane recovery in an example reservoir. Their injection scenarios included a Zero Emission Power Plant (ZEPP) at the surface, supplying the reservoir with a constant CO_2 rate over 25 years. CO_2 breakthrough occurred between 3-15 years from the start (depending on injection rate). The highest incremental gas recovery was obtained for the case of injection after conventional depletion of the reservoir. The maximum gas recovery was bout 10% of the Gas Initially In Place (GIIP). In

Parameter (unit)	Value
Age (-)	Triassic- Scythian (270 Ma)
Illite-free porosity range (%)	8-12
Illite-affected porosity range (%)	9-15
Illite-free permeability range (mD)	25-180
Illite-affected permeability range (mD)	0.02-0.1
Area (km^2)	24
H_f, gas column (m)	298
GRV, Gross Rock Volume (km^3)	3.5
Gas saturation (%)	65
Formation volume factor (-)	0.0070
P_0, initial pressure (MPa)	12.41
P, current pressure (MPa)	0.82
T, temperature (^{o}C)	33
GIIP, gas initially in place (BSCM)	36.5
Recovery factor (%)	80
Drive mechanism (-)	volumetric depletion
Number/type of well (-)	10 production
Number/type of well (-)	4 appraisal

Table 2: Summary of the North Morecambe field properties (taken from Cowan & Brown (2003)).

a similar approach, Jikich et al. (2003) studied, using numerical simulation, the effects of injection strategy and operational parameters in a thin sandstone reservoir in Northern West Virgina. Their results suggested that highest methane recovery would be obtained when the reservoir is produced under primary recovery until depletion, followed by CO_2 injection. The maximum amount of incremental CH_4 recovery was around 10% of the Gas Initially In Place (GIIP). In a more generic study, Al-Hasami et al. (2005) used a compositional reservoir simulator to study EGR processes, such as gas mixing and CO_2 solubility in formation water, and performed a sensitivity analysis of various design and operating parameters. They concluded that an incremental gas recovery of 8-11% of GIIP (close to the findings of Clemens & Witt (2002) and Jikich et al. (2003)) can be expected for reservoirs with primary recovery factor of around 85%.

Following the same trend, Seo & Mamora (2005) performed a 3D simulation for a five-spot pattern of wells to evaluate the injection of supercritical CO_2 under

typical reservoir condition. Their results suggested CO_2 sequestration potential of 1.2 million tonnes (Mt) in 29 years and 4.8 Mt in 56 years, corresponding to gas recoveries of 68% and 74% of the Gas Initially In Place (GIIP), respectively. They also provide a produced gas revenue estimation of $9.8 million based on a gas price of $2.0/MSCF (million standard cubic feet). In a different approach, Liu et al. (2013) used a dual-porosity dual-permeability model to investigate the possibility of CO_2 sequestration with EGR in the New Albany shale gas reservoir in the Illinois Basin, USA. They suggested that 40,000 tonnes of CO_2 can be injected in this reservoir within a five-year period, 95% of which will be effectively sequestrated. Also they forecasted an incremental CH_4 recovery of around 1% of the GIIP. Most recently, Zangeneh et al. (2013) performed numerical simulation of CO_2-EGR in the Gavarzin field in the Qesh Island, south of Iran. They found that early CO_2 injection, i.e., from the beginning of production, is likely to result in decreased Net Present Value (NPV) of the produced gas, due to excessive mixing with the injection gas, as also suggested by Clemens & Witt (2002), Jikich et al. (2003) and Hussen et al. (2012). Additionally, they propose that in a 5-spot well setting, the injection rate should be lower than the production rate to reduce undesired gas mixing.

Oldenburg et al. (2004) used numerical simulation to perform an economic feasibility study of the CO_2-EGR in the Rio Vista gas field in California. They found that the largest expenses are likely to be due to CO_2 capture, purification, compression and transport to the field. Moreover, they suggest that economic feasibility is most sensitive to the global CH_4 price, CO_2 supply cost and ultimately, to the ratio of CO_2 injected to incremental CH_4 produced. Assuming a gas price bracket of 3-5 US$/MCF (million cubic feet), they further recommend a CO_2 supply cost bracket of 4-12 US$/tonne, within which CO_2-EGR will be economically feasible. More recently, Hussen et al. (2012), using numerical simulation, performed an economic feasibility study of EGR in a high pressure reservoir case, which further emphasised the necessity of delaying CO_2 injection until the later stages of the gas field life.

The bulk of the numerical work discussed above suggests that EGR due to CO2 injection is likely to lead to an incremental recovery of around 10% of the Gas Initially In Place (GIIP). Furthermore, injection close to depletion stage seems to be the optimum injection strategy (as opposed to injection during the primary production period), which is favourable in our particular case study reservoir, which is currently close to depletion stage and at reservoir pressure of 0.82 MPa.

7.4 NUMERICAL MODEL AND ASSUMPTIONS

To simulate the EGR processes, a modified version of the reservoir simulator of Chapter 6 was used, which it is made two-dimensional for better spatial representation in this context. The simplifying assumptions are as follows. The gas composition in the North Morecambe field is as listed in Table 3. Our numerical model however, is only capable of simulating three components, namely CO_2, CH_4 and H_2O. Therefore, Methane and Ethane are lumped together and modelled as CH_4 and the rest of the impurities were modelled as CO_2. Consequently, the simulated in-situ gas composition is 87.13% CH_4+12.87% CO_2.

Specie	mol (%)
CH_4	81.02
C_2H_4	6.11
N_2	6.88
CO_2	5.89
H_2	0.08
He	0.02

Table 3: Dry gas composition in the north Morecambe field (Cowan & Brown, 2003).

The effect of gravity was investigated using numerical simulation in an injection-only scenario in a low-pressure reservoir case. For the length- and time-scales generally considered for EGR, gravity does not have enough time to make any considerable impact on the flow distribution in the reservoir, at least for the cases where pressure is low. This is expected since the reservoir under consideration is initially filled with

gas (water is present as immobile, residual droplets in the pore space), also, at the pressures and temperatures being modelled (i.e., 0.82 MPa and 33^{o}C), CH_4 and CO_2 are both in gaseous state, as opposed to super-critical state, and therefore the density contrast between the two species is not that significant. Therefore, vertical flow and gravity effects were neglected for the subsequent injection/production simulations.

As for incorporating gas production wells within the model, an idealised uniformly-spaced well-pattern is assumed, as shown schematically in Figure 27. This pattern is often referred to as five-spot pattern, where each production/injection well is surrounded by four injection/production wells. One advantage of the five-spot pattern is that, due to symmetry of the flow field, only a quarter of the five-spot group of wells needs to be simulated (the boxed region in Figure 28). Additionally, this pattern correlates relatively well with the existing well-positioning within the North Morecambe field, i.e., N_1, N_4, N_6, N_8 and N_9 (see Figure 25), where N_4 can be used as the production well and the other four as injection wells (the same applies to N_1, N_2, N_5, N_6 and N_{10}). Interestingly these wells are already CO_2 (corrosion) resistant, due to high CO_2 content of the in-situ gas in this reservoir (see Table 3).

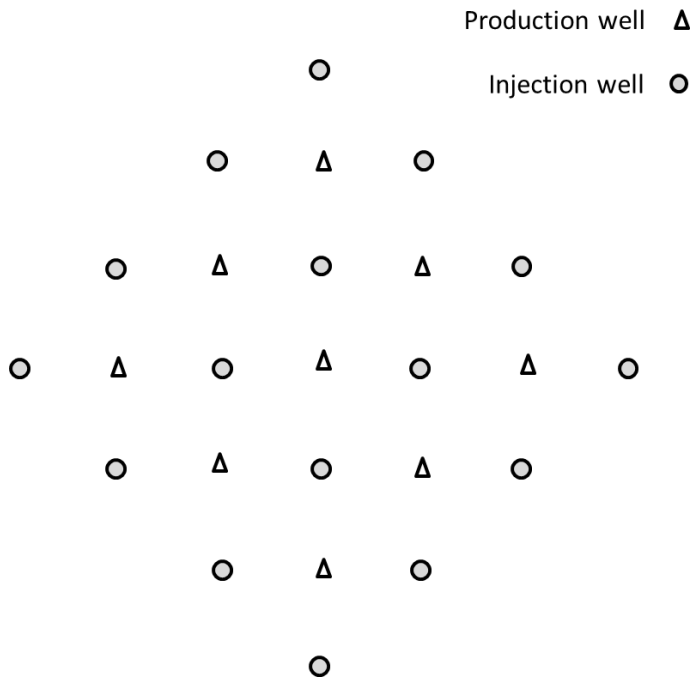

Figure 27: Schematic of five-spot equidistant well pattern.

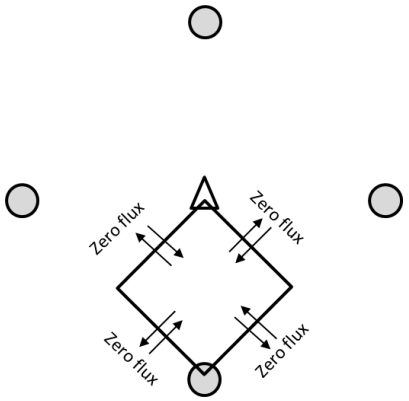

Figure 28: Zero-flux boundary due to five-spot well pattern.

Thus, the numerical model to simulate injection and production scenarios includes one injection well and one production well. A schematic diagram of the numerical grid is shown in Figure 29. The grid is clustered more finely close to the vertices (well locations) to capture the higher flow gradient in those regions.

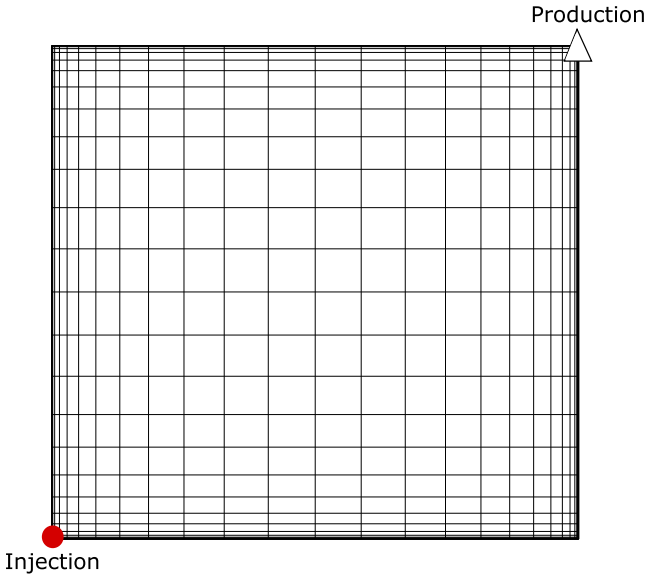

Figure 29: A schematic diagram of the 2D numerical grid for 30 grid cells in each direction, showing a finer grid clustering around the injection and production wells to capture the higher flow gradients in those regions. Note that this diagram is not to scale and the actual grid used comprised of 100 cells in each direction.

With reference to Table 2, there is a range of values provided for permeability and porosity for the North Morecambe field and yet there is no heterogeneity or permeability anisotropy data available. Furthermore, there is no information available in the literature regarding the relative permeability characteristics of the Sherwood Sandstone Group associated with the North Morecambe field. There is additional uncertainty concerning the formation thickness of the illite-free layer (note that the illite affected zone is not included within the model zone due to its exceptionally low permeability). Therefore, the parameters requiring calibration include, absolute permeability (k), porosity (ϕ), thickness of the illite-free layer (H) and relative permeability parameters.

The calibration procedure adopted can be described as follows. With reference to parameters in Table 2, an idealised cylindrical reservoir is assumed with an equivalent pore-volume of the North Morecambe field (Figure 30). The GRV (Gross Rock Volume) of this reservoir is estimated as 3.5 km^3. The radius of an equivalent cylindrical reservoir can be calculated from:

$$r = \sqrt{\frac{V}{\pi H_f}} \approx 1921 \text{ m} \tag{7.3}$$

Furthermore, according to the production data obtained from the website of the Department of Energy and Climate Change (DECC, 2016) (see Figure 26), in a 21-year production period, 28.8 billion standard cubic meters (BSCM) of gas has been produced from the permeable illite-free layer of the North Morecambe field, with an average rate of 114.3 MSCM/month, after which the reservoir pressure declined from the initial 12.41 MPa to the current value of 0.82 MPa. However, it should be noted that, ϕ and H dictate the volume that the illite-free layer should have in order for pressure to decline to 0.82 MPa after extraction of 28.8 BSCM of

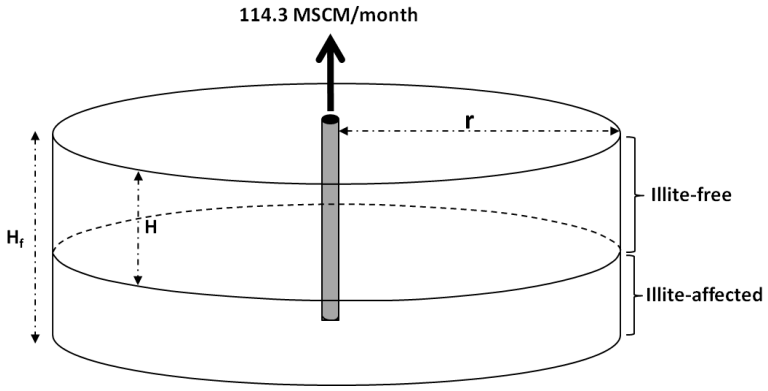

Figure 30: Morecambe field equivalent cylindrical reservoir. H_f(m) is formation thickness. H(m) is the thickness of the illite-free layer.

gas, and absolute+relative permeabilities control how fast/slow fluids move in the reservoir, dictating the time after which the reservoir reaches the current pressure of 0.82 MPa. Therefore, calibration is divided into two parts: (1) fitting the reservoir volume parameters, i.e., ϕ and H, to the gas production-pressure curve, (2) fitting the permeability and relative permeability parameters to the time-pressure curve.

The range of values selected for model calibration are listed in Table 4. The relative permeability parameters relate to Eqs. (5) and (6) in Goudarzi et al. (2016). Note that for relative permeability parameters, the simulations were found to be insensitive to the power law exponent of the gas and liquid phases and also the liquid phase end-point relative permeability. This is expected, as the water is only present as residual droplets and is immobile from the start. Thus, simulations were performed for all the combinations of ϕ and H, results of which are shown in Figure 31, and for all combinations of k and k_{rg_0}, the results of which are presented in Figure 32. Therefore, according to Figures 31 and 32, it can be concluded that our equivalent reservoir should have an average porosity of $\phi = 0.10$, an illite-free layer thickness of $H = 225$ m, an absolute-permeability of $k = 60$ mD and an end-point relative-permeability of $k_{rg_0} = 0.6$, in order for this equivalent reservoir to best represent the North Morecambe field.

Parameter (unit)	Values
H, illite-free layer thickness (m)	50, 75, 100, 125, 150, 175, 200, 225, 250
ϕ, porosity (%)	8, 9, 10, 11, 12
k, absolute-permeability (mD)	25, 60, 100, 140, 180
kr_{g_0}, gas end-point relative permeability (-)	0.2, 0.4, 0.6, 0.8, 1.0
kr_{l_0}, liquid end-point relative permeability (-)	Insensitive
n_g, gas relative permeability exponent (-)	Insensitive
n_l, liquid relative permeability exponent (-)	Insensitive

Table 4: Values tested for model calibration.

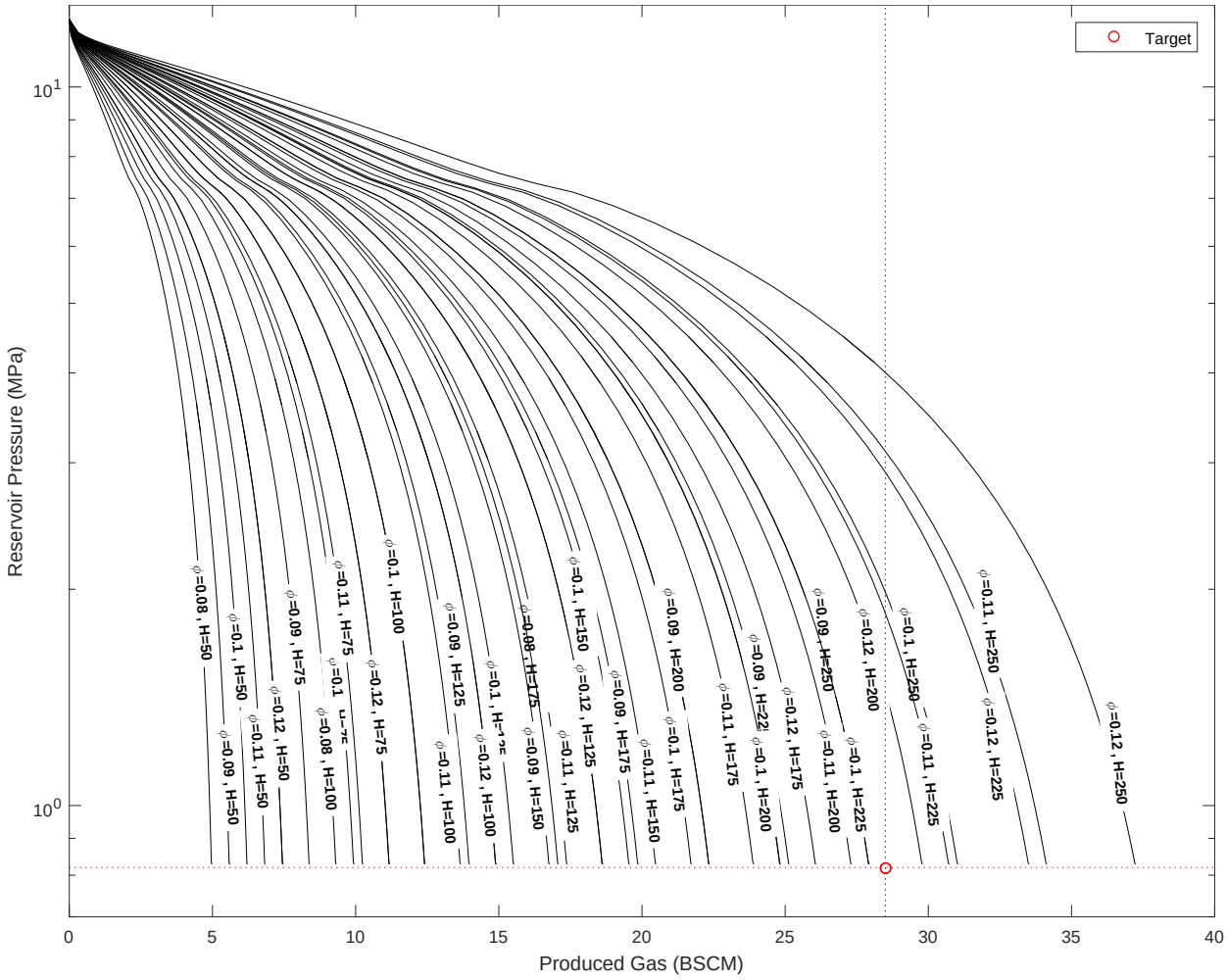

Figure 31: Model calibration: plot of reservoir pressure against gas production for different values of gas-layer thickness, H(m), and porosity, ϕ. It shows that a reservoir with $\phi = 0.10$ and $H = 225$ m will roughly contain the right volume of Gas Initially In Place (GIIP) at the initial pressure of 12.41 MPa, such that after production of 28.8 BSCM of gas the reservoir pressure declines to the current value of 0.82 MPa,, which is the "target" point here.

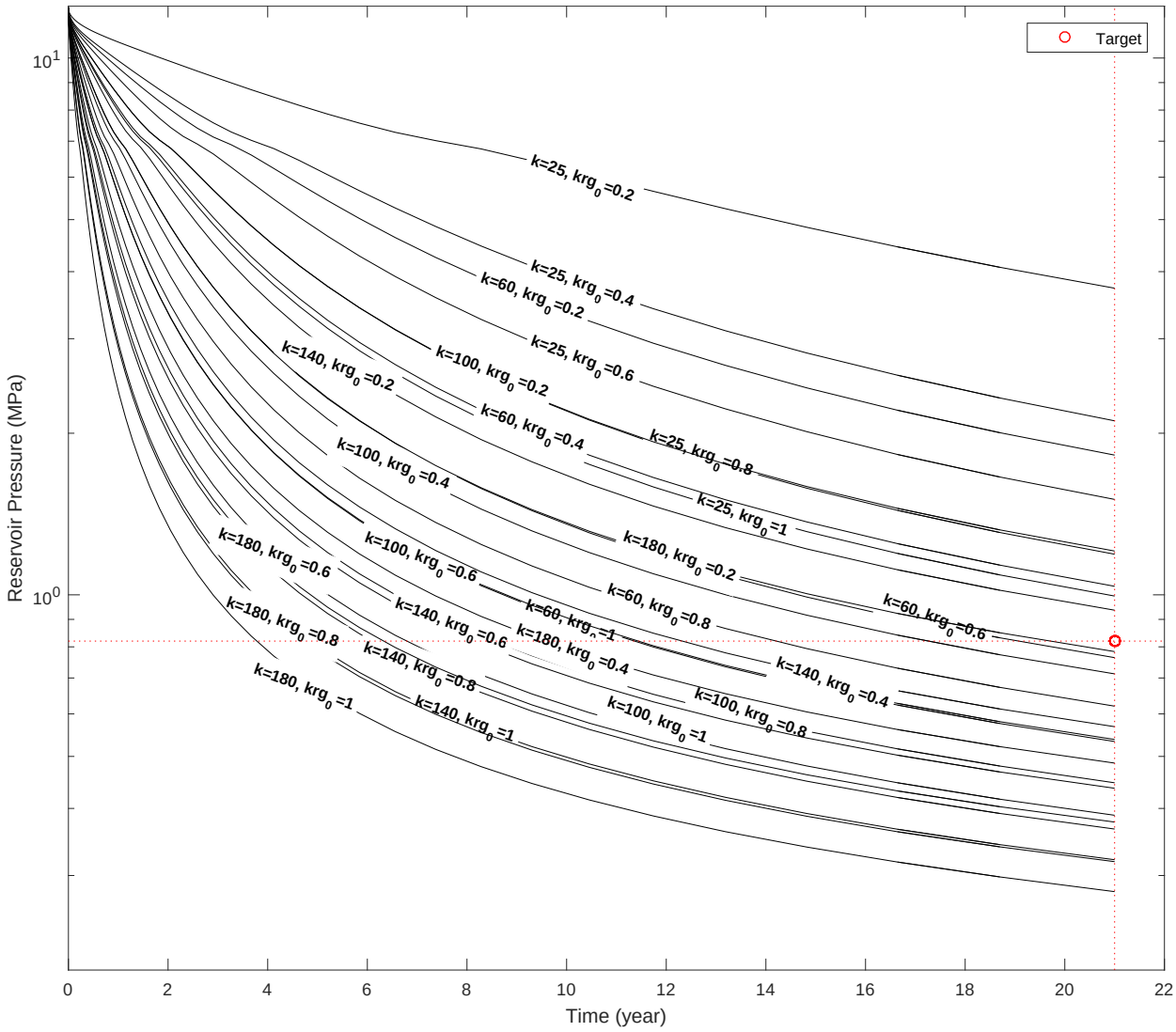

Figure 32: Model calibration: plot of reservoir pressure against time for different values of absolute-permeability, k (mD) and gas-phase end-point relative-permeability parameter, kr_{g_0}. It shows that a reservoir with $k = 60$ mD, and $kr_{g_0} = 0.6$ will roughly have the right level of permeability to allow production of 28.8 BSCM of gas in 21 years of production (with an average production rate of 114.3 MSCM/month), which is the "target" point here.

In Section 7.2, the remaining gas in the North Morecambe field (gas in illite-free + illite-affected) was estimated as 7.7 BSCM (21% of the GIIP). Based on the new estimation of porosity and formation thickness, the volume of the recoverable gas (i.e., the gas residing in the permeable illite-free layer only) would be around 2.04 BSCM (5.6% of the GIIP). In the next section, it will be shown using numerical simulation, how much of the 5.6% of the GIIP can be recovered using CO_2 injection.

7.6 SIMULATION RESULTS AND DISCUSSION

Numerical simulation of CO_2-EGR in the North Morecambe field was performed using the parameters in Table 5. Figs. 33 and 34 show contour plots of pressure and CH_4 mass fraction, respectively, with the injection well located at the bottom left corner and the production well is located at the top right corner, as shown in figure 29. Fig. 33 shows that, for 1 kg/s injection rate scenario, pressure is increasing around the injection well until the pressure wave reaches the production well and the gas production rate reaches its target rate of 1 kg/s. Following on from this, the reservoir pressure decreases. For higher injection rate scenarios, it is observed that the reservoir pressure increases monotonically with time. Nevertheless, although overall the reservoir pressure is declining, it can be seen in figure 34, that the CO_2 is sweeping the CH_4 towards the production well where it is being recovered.

Figure 35 shows plots of pressure, temperature and CH_4 mass fraction in the gas phase at different times, and on the diagonal connecting the injection to the production well, for the 1kg/s injection and production rates scenario. Slight pressure build-up can be observed around injection well and pressure decline around the production well, resulting in overall decrease in reservoir pressure for the chosen injection and production rates. There is a slight temperature decrease around both injection and production wells, due to Joule-Thomson cooling (JTC) effects (Mathias et al., 2014, **?**, Oldenburg, 2007). Note that the thermal front is generally behind the CO_2 plume (see temperature profiles in conjunction with the CH_4 mass fraction profiles) as a result of heat retardation associated with the high specific heat capacity of the host rock and the residual water (Mathias et al., 2014, **?**). Nevertheless, for the chosen injection/production rate, changes in temperature are negligible. Also, for higher injection rates (up to 4 kg/s), the maximum observed temperature drop is less than 3 ^{o}C.

Finally, the effect of injection rate on CO_2 break-through time is presented in figure 36. For very low injection rates CO_2 break-through does not occur in a 20-year injection and production period. However, as the injection rate is increased, break-through occurs and break-through times decrease with increasing rates. Break-through time is of particular importance for reservoirs at near-depletion stage, as it determines how much the field's life can be expected to be extended, by deferring field abandonment and the high costs associated with it (Pittard , 1997).

Figure 36 also shows that around 0.11 BSCM (0.3% of the GIIP) of incremental gas per five-spot unit is expected to be produced as a consequence CO_2 injection, also extending the fields life for up to around 5 years. Note that, given the efficiency of CO_2 in displacing CH_4, it can be said that, hypothetically, and assuming enough additional wells are drilled, almost all of the 2.04 BSCM of gas can be recovered, which sets the ultimate incremental EGR potential to around 5% of GIIP in the North Morecambe field. Of course, whether additional drilling is an economically sound idea, depends on many factors such as global wellhead CH_4 prices, drilling costs, CO_2 acquisition costs, etc., which will be discussed in the next section.

Parameter (unit)	Value
Initial Gas Molar Composition	87.13% CH_4+12.87% CO_2
L, Width of the quarter of the 5-spot well group (m)	550
H, Formation Thickness (m)	225
Porosity (%)	10
Absolute Permeability (mD)	60
Initial Petroleum Saturation (%)	65
P_0, Initial Pressure (MPa)	0.82
T_0, Initial Temperature (^{o}C)	33
GIIP, gas initially in place (BSCM)	2.04
CO_2 Injection Rate (kg/s)	1.0
Maximum Production Rate (kg/s)	1.0
kr_{g_0}, Gas end-point relative permeability (-)	0.6
kr_{l_0}, Liquid end-point relative permeability (-)	1.0
n_g, Gas relative permeability exponent (-)	3.0
n_l, Liquid relative permeability exponent (-)	3.0

Table 5: Modelling parameters used in simulation of the CO_2-EGR in the permeable illite-free layer of the North Morecambe gas field.

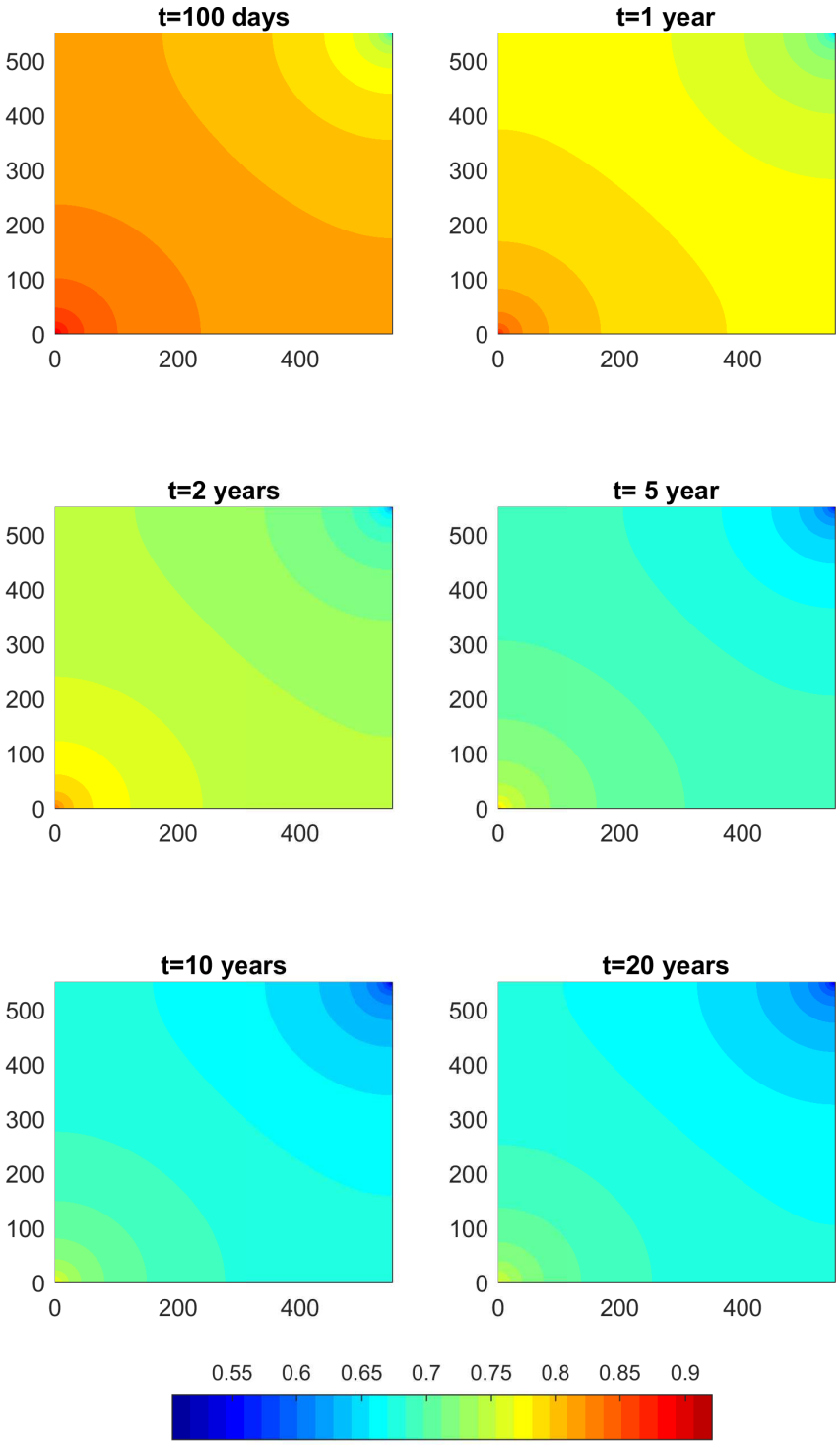

Figure 33: Contour plot of pressure at different times for a quarter-space of the five-spot group of wells. The injection well is located at the bottom left corner and the production well is located at the top right corner. For the chosen injection and production rates, i.e., 1 kg/s each, the reservoir pressure is decreasing with time. For higher injection rates (not shown here), the reservoir pressure increase with time. Pressures are in MPa.

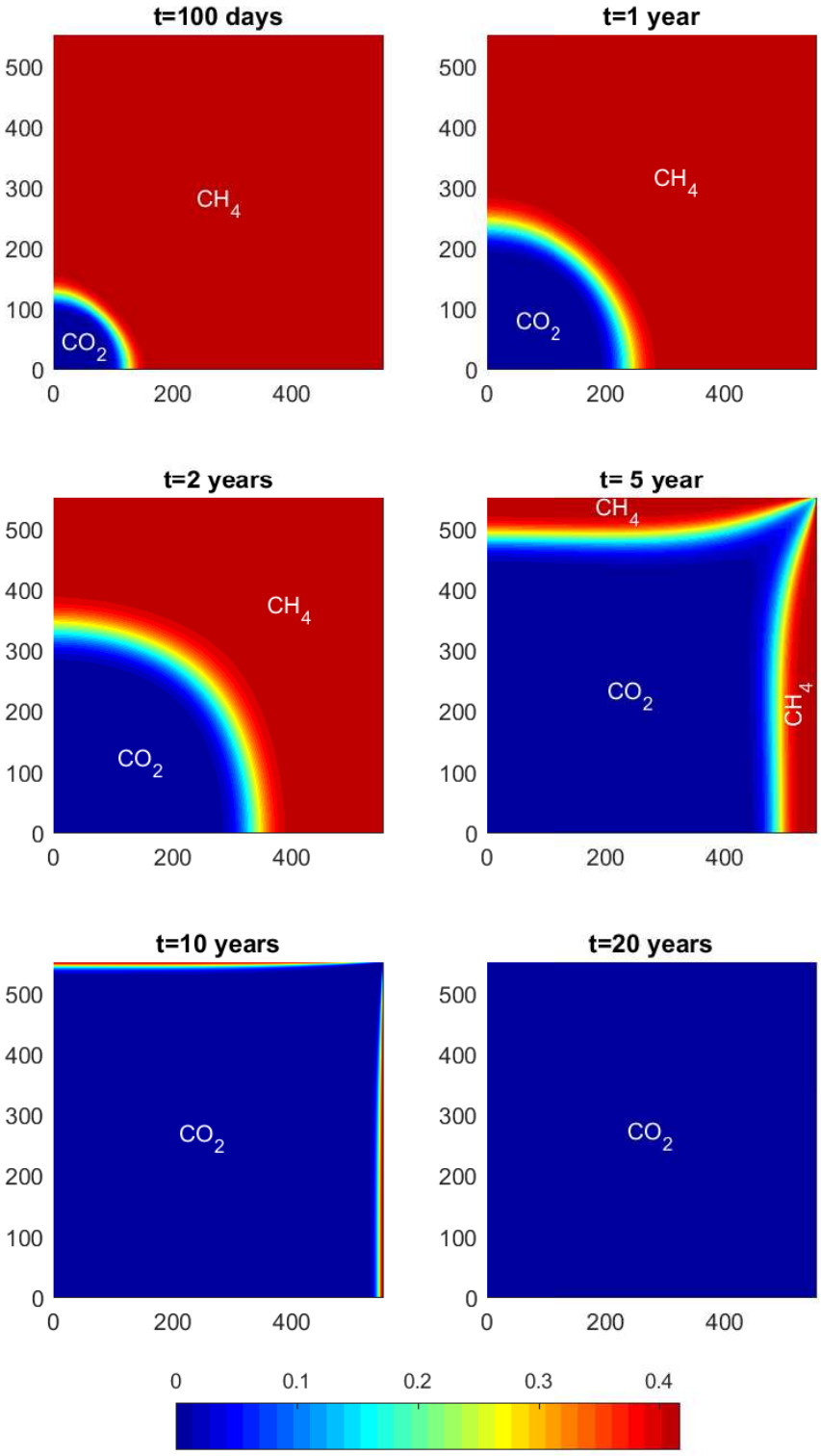

Figure 34: Contour plots of CH_4 mass-fraction in the gas-phase at different times for a quarter-space of the five-spot group of wells. The injection well is located at the bottom left corner and the production well is located at the top right corner. CO_2 sweeps the CH_4 from the injection point towards the production well where it is being recovered. The scale on the colorbar below the subplots is in terms of dimensionless CH_4 mass-fraction in the gas-phase.

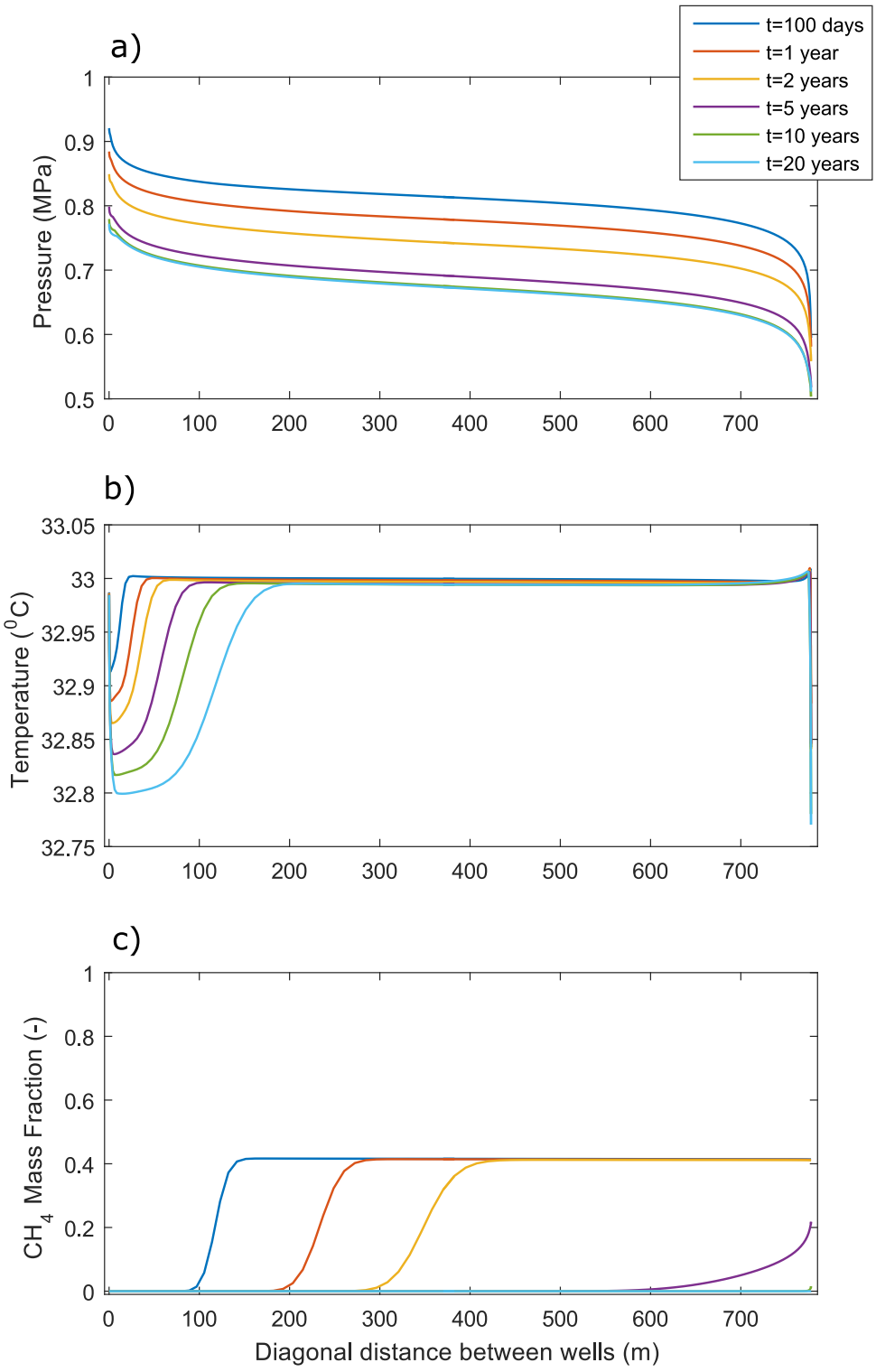

Figure 35: From a) to c) are plots of pressure, temperature and CH_4 mass-fraction in the gas-phase, respectively, at different times and on the diagonal connecting the injection to the production well in a five-spot well setting. In all cases, injection well is located at the left hand side of the plots and the production well is located at the right hand side.

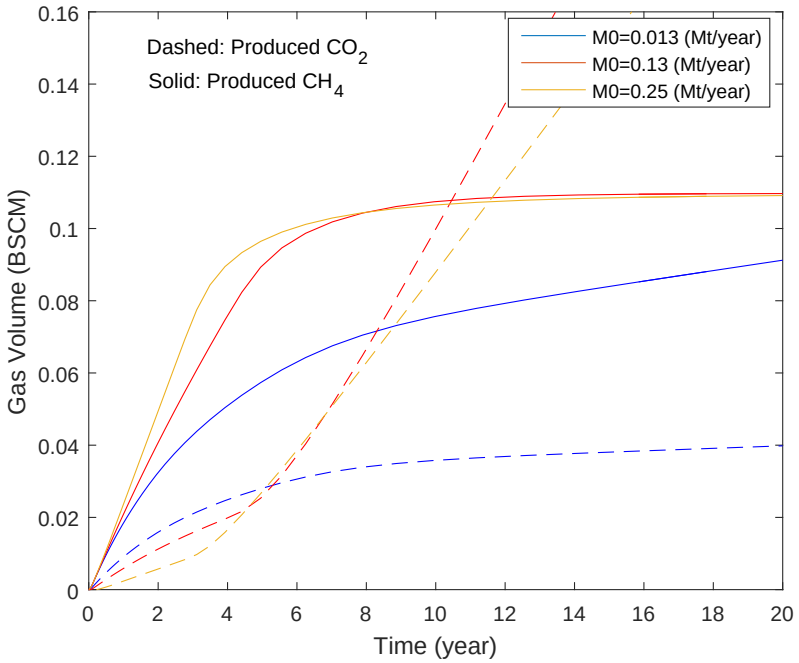

Figure 36: Plot of cumulative incremental volume of each gas specie produced over time and for different injection rates. Not that injection rates are per five-spot group of wells (injection rate per injection well is one-fourth of this value).

7.7 ECONOMIC FEASIBILITY OF CO_2-EGR IN NORTH MORECAMBE GAS FIELD

An economic feasibility study of CO_2-EGR in the North Morecambe field was conducted, based on the simulated incremental CH_4 recovery potential per five-spot group of wells, global well-head CH_4 prices, offshore drilling cost, CO_2 supply cost and UK's Carbon Price Floor (CPF). In this context, CO_2 supply cost refers to the cost of acquiring, transporting and injecting the CO_2. Oldenburg et al. (2004) estimates the CO_2 supply cost to be 10 US$/tonne from a relatively pure fertiliser or cement plant source, up to 50 US$/tonne from a power plant capture unit. Gresham et al. (2010) estimate CO_2 supply cost to vary from 20 US$/tonne using an Integrated Gasification Combined Cycle (IGCC) up to 75 US$/tonne using a Natural Gas Combined Cycle (NGCC), and Gozalpour et al. (2005) estimates the supply cost to vary from 14 US$/tonne from a naturally occuring CO_2 source up to 54 US$/tonne

from a pulverised coal-fired plant capture unit. Therefore, a CO_2 supply cost bracket of 10-75 US$/tonne is used in the cost estimations. On the other hand, Carbon Price Floor (CPF), refers to the amount tax penalty to be paid by a CO_2 emitter per tonne of emission. According to UK government's website (GOV.UK , 2016), UK's CPF is currently at 23 US$/tonne of CO_2 emitted (18 £/tonne) and is expected to rise to 37 US$/tonne (30 £/tonne) by 2020.

Different scenarios were considered which are shown in figure 37. In the first scenario, only the existing wells are utilised, to avoid additional drilling costs, which corresponds to two five-spot units. In the second scenario, four additional CO_2-resistant wells are drilled, corresponding to two more five-spot units (i.e., four in total). Using the inputs provided from our industry partners, the upper-bound cost of offshore drilling in the East Irish Sea Basin was estimated as 10 million US$ per CO_2 resistant well.

Figure 38 shows a plot of generated revenue (from the sales of the incremental CH_4 production + savings on CO_2 tax due to CPF) for different global CH_4 prices, versus, the costs (CO_2 supply + drilling) for different CO_2 supply-cost values, all in millions of US$. Note that in this figure, the UK's current Carbon Price Floor (CPF) of 23 US$/tonne is used for the estimations. Subplot a) is the scenario requiring no additional drilling (corresponding to 2 five-spot units) and its operational net worth. b) is the scenario requiring two additional wells to be drilled (corresponding to 3 five-spot units) and it operational net worth. c) is the scenario requiring four additional wells to be drilled (corresponding to 4 five-spot units) and its operational net worth. Also note that, based on the numerical simulation results, each five-spot unit is assumed to have a incremental gas recovery potential of 0.11 BSCM. In the "net worth" plots, any value below the zero contour line is considered uneconomic. Therefore, from figure 38, it can be concluded that, the no-drilling scenario is the most economically viable option in this case. This is mainly due to high offshore drilling costs and low current gas prices. In this case, with the current global CH_4

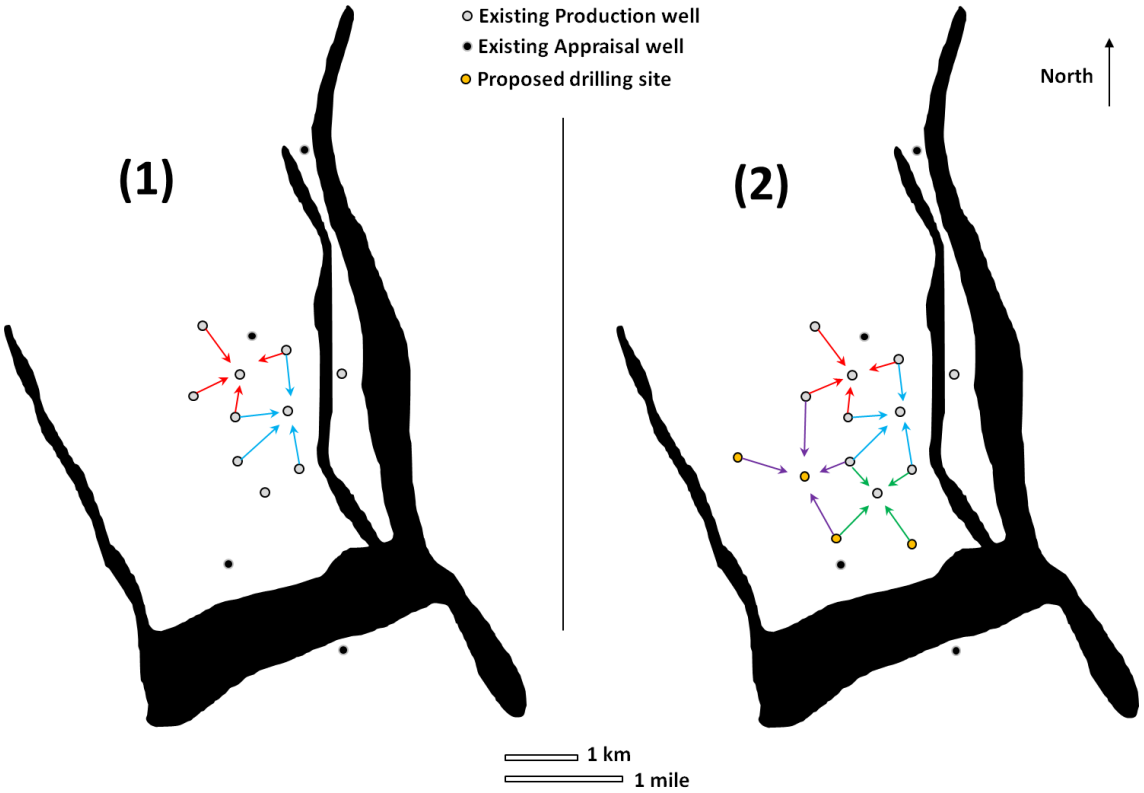

Figure 37: Simulation scenarios for the economic feasibility studies of CO_2-EGR in the North Morecambe gas field. In scenario (1), only the existing wells are utilised (to avoid high offshore drilling costs), corresponding to 2 five-spot units. In scenario (2), four additional CO_2-resistant wells are drilled, corresponding to 4 five-spot units in total. Each color set represents one five-spot group of wells.

price being 3.1 US$/MMBtu, the CO_2 supply cost needs to be less than 50 US$/tonne for such a scheme to break even (see figure 38).

Figure 39 is the same as figure38, except that here the projected value of the UK's CPF for 2020, i.e., 37 US$/tonne of emission, is used for revenue estimations. Therefore, from figure 39, it can be said that still the most economically viable option for the North Morecambe field is the "no drilling" scenario. From a) to c), and assuming the CH_4 sales price stays around the current value of of 3.1 US$/MMBtu, supply cost needs to be less than 63 US$/tonne, 52 US$/tonne and 47 US$/tonne, respectively, for such a scheme to break even.

7.8 SUMMARY AND CONCLUSIONS

The aim of this chapter has been to explore, using numerical simulation, the potential for Enhanced Gas Recovery (EGR) by CO_2 injection in the North Morecambe gas field. North Morecambe is located in the East Irish Sea basin and currently contains recoverable resources of around 2.04 BSCM. However, due to a currently excessively low field pressure of 0.82 MPa, it is not possible to recover the remaining gas at an economic rate, using a volumetric depletion method, therefore an Enhanced Gas Recovery application would be desirable for this.

Due to uncertainties regarding the field data, the numerical simulator was calibrated to obtain the uncertain parameters using previous gas production history data. Numerical simulation was then performed using the fitted parameters to explore a range of EGR by CO_2 injection scenarios in the context of the North Morecambe field. The results suggest an ultimate recovery potential of around 5% of the GIIP, assuming it will be economic to drill sufficient number of additional wells to fill the entire reservoir's volume with CO_2 and thus produce all of the recoverable CH_4. For more realistic scenarios, an economic feasibility study was performed, taking into account the simulated incremental recovery potential, global wellhead CH4 prices, offshore drilling costs, CO_2 supply cost and UK's Carbon Price Floor (CPF). It was assumed that CO_2 supply cost ranges from 10 US$/tonne to 75 US$/tonne and offshore drilling cost in the east Irish Sea Basin area is around 10 million US$ per well. Both current value of 23 US$/tonne of emission, and the 2020 projected value of 37 US$/tonne of emission, for UK's CPF were used in the revenue estimations.

Under these circumstances, the no-drilling scenario was found to be the most economically viable option. For such an option, incremental EGR potential is around 0.7% of GIIP, translating to 0.22 BSCM of gas volume can be expected. In this case, the revenue generated from the CH_4 sales plus the savings on CO_2 emission tax (due to CPF) breaks even with the operating costs when the CO_2 supply cost is less than

50 US$/tonne, using the current CPF value, and less than 63 US$/tonne, assuming the projected value of 2020 CPF in the UK. Nonetheless, assuming an average CO_2 supply cost of 50 US$/tonne, by 2020, CO_2-EGR in the North Morecambe field can generate a revenue of around 13 million US$ at no extra cost. However, if the future CO_2/CH_4 markets involve payments to operators willing to store the CO_2, an upwards shift in CH_4 prices, and/or a reduction in CO_2 supply cost due to advancements in capture technologies, etc., the economics of CO_2-EGR will improve dramatically, leading to an economically viable incremental EGR potential of 5% of the GIIP, equivalent to over 2 BSCM of CH_4 volume.

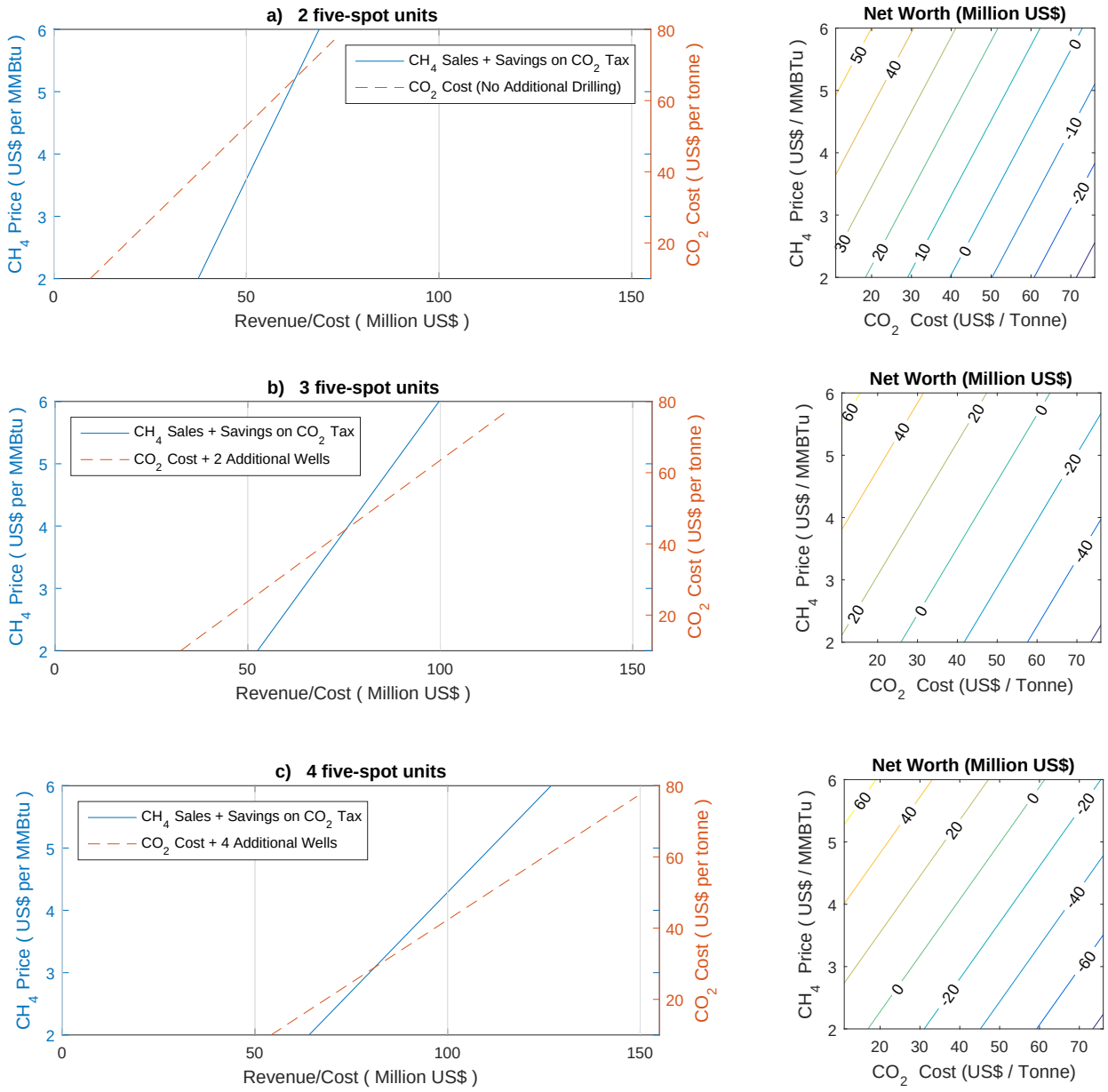

Figure 38: Economic feasibility of CO_2-EGR in the North Morecambe gas field based on UK's current Carbon Price Floor (CPF) of 23 US$/tonne. a) is the no-drilling scenario (corresponding to 2 five-spot units) and its operational net worth. b) is the scenario requiring two additional wells to be drilled (corresponding to 3 five-spot units) and its operational net worth. c) is the scenario requiring four additional wells to be drilled (corresponding to 4 five-spot units) and its operational net worth. The study assumes incremental gas recovery of 0.11 BSCM per five spot unit, which is based on our numerical simulations.

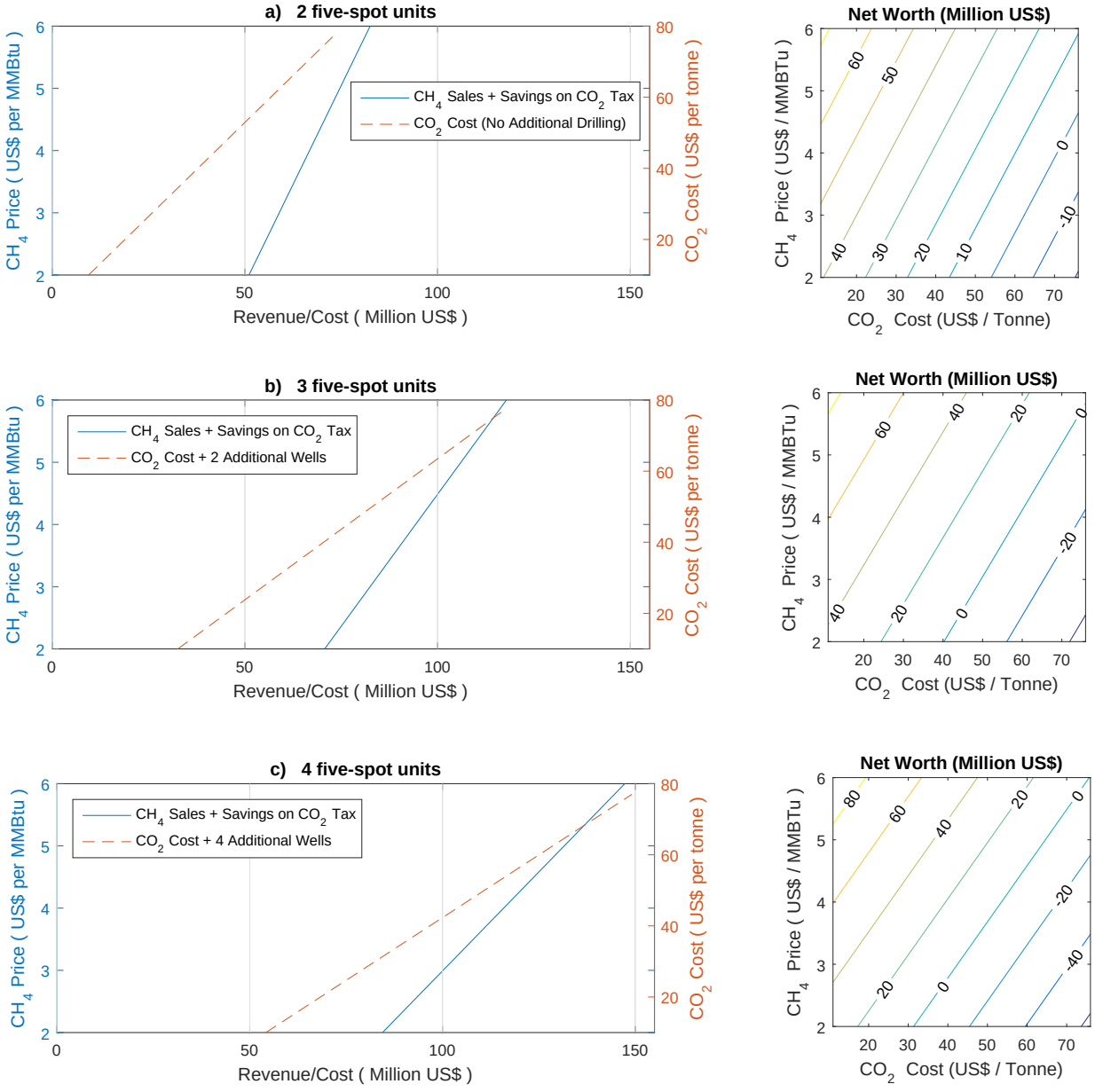

Figure 39: Economic feasibility of CO_2-EGR in the North Morecambe gas field, based on the projected value of the UK's Carbon Price Floor (CPF) for 2020, i.e., 37 US$/tonne. a) is the no-drilling scenario (corresponding to 2 five-spot units) and its operational net worth. b) is the scenario requiring two additional wells to be drilled (corresponding to 3 five-spot units) and its operational net worth. c) is the scenario requiring four additional wells to be drilled (corresponding to 4 five-spot units) and its operational net worth. The study assumes incremental gas recovery of 0.11 BSCM per five spot unit, which is based on our numerical simulations.

8

SUMMARY, FINDINGS AND FUTURE WORK

The objective of this project has been to develop a numerical model capable of modelling heat transport, pressure build-up and compositional changes in a multi-component multi-phase (MCMP) porous-media flow system, in the context of CO_2 injection into very low-pressure partially-depleted gas reservoirs; and ultimately, to simulate CO_2 injection in Centrica Plc's North Morecambe gas field (located in east Irish Sea) and estimate the gas recovery potential associated with CO_2-EGR in this field.

8.1 SUMMARY

In Chapter 2, we started by deriving the governing equations for flow of N_c number of components in N_p number of phases. It was shown that there will be at least $(N_c+1) \times N_p$ number of variables in the system, giving rise to the need for selecting N_c number of persistent Primary Dependent Variables (PDVs) to solve for. It was decided that solving for pressure, P, temperature, T, and component mass-fractions, z_i (as opposed to component mass-densities G_i), would be a reasonable choice. This was attributed to the fact that, for a given volume of fluid mixture, the z_i values will not change with P and T, making the selected set of PDVs truly independent of one another; whereas, the associated mass of each component per volume of rock, G_i, may change with P and T. Additionally, z_i were the variables used in the phase diagram, which determine the equilibrium properties of the multicomponent fluid mixture.

Solution of the governing equations of MCMP flow problem requires calculation of component mass fractions in each of the present phases, at the pressures and temperatures being modelled. In Chapter 3, in a new approach, the mutual solubility correlations for mixtures of CO_2-H_2O and CH_4-H_2O, available in the literature, were joined together to form a ternary CO_2-CH_4-H_2O equilibrium model. The predictions of the resulting ternary equilibrium model matched well with the available experimental solubility data from the literature. Hence, this model was used to evaluate the component mass fractions, X_{ij} [-], that appear in the mass conservation statement of each of the components.

Method of Lines (MOL) is a numerical solution technique for solving PDEs, in which all but one dimension are discretised and the resulting system of ODEs are solved using an ODE-solver of choice; in our case MATLAB's ode-solver ode15s. When using ODE-solvers to solve for the aforementioned PDVs, the user must construct an ODE function. Within this function, a scalar value of time is provided as an input along with an associated vector of the PDVs. The user must define the ODE function such that it calculates the derivatives of the PDVs with respect to time, meaning that the the governing equations of the MCMP problem must be re-casted in terms of the selected set of PDVs; this generally involves a combination of chain- product-rule differentiation, resulting in appearance of partial derivative terms of some of the flow properties with respect to the PDVs. For conventional first-order time-stepping methods, it is arguably acceptable to evaluate these derivatives using first- or second-order finite differencing. However, given the high accuracy associated with the use of MATLAB's ODE solvers, it was pertinent to obtain these derivatives as accurately as possible. Hence, a method of analytical evaluation of the partial derivative terms was developed in Chapter 4, for improved accuracy and computational efficiency.

Thus, a numerical model was developed to solve the two-phase three-component flow problem, in the context of CO_2 injection into deep (P=32 MPa, T=85 ^oC) and

shallow (P=10 MPa, T=45 ^{o}C) water-leg of a reservoir, initially only containing CH_4+H_2O; the reason for choosing this P-T range was to be able to compare the results to the analytical solution, which is no valid for low pressures.

After verifying the model using the analytical solution, we used this numerical model to simulate the EGR potential in the North Morecambe gas field; where, due to uncertainties associated with the available data, in particular permeability anisotropy, heterogeneity and relative permeability characteristic of the reservoir rock, a sensitivity analysis was carried out to try and fit these parameters using a kind of history matching method. The results suggested that, $k = 60$ (mD), $\phi = 10\%$ (-) and $kr_{g0} = 0.6$ (-) provided the best fit. Later on, ignoring gravity enabled us to use a so-called five-spot well-pattern; having the advantage of being symmetrical, this pattern allowed for simulation of only a quarter of the physical domain for reduced computational time.

8.2 FINDINGS

The results of simulating CO_2 injection into the water-leg of a deep (P=32 MPa, T=85 ^{o}C) and a shallow (P=10 MPa, T=45 ^{o}C) reservoir, were in excellent agreement with the analytical solution, predicting accumulation of a CH_4 bank ahead of the CO_2 plume and accurately locating the associated shock fronts while considering the partial miscibility of both CO_2 and CH_4 in H_2O. We explained the formation of a methane bank as follows: as CO_2 is injected, it partitions into the gas phase and the aqueous phase. The initially dissolved CH_4 exsolves immediately, which is then pushed ahead of the growing CO_2 plume, leading to development of a CH_4 bank. Mathematically, the system is constrained to constantly enter and leave the two-phase region along the tie-lines representing the injection and initial compositions; therefore, the leading CH_4 bank is free from the injected gas, CO_2. Moreover, in a series of numerical simulations for different initial gas saturations (everything else being the

same), it was found that the level of CH_4 bank saturation is independent of the initial CH_4 saturation.

Non-isothermal simulations showed that the thermal front is generally behind the CO_2 plume, as a result of heat retardation associated with the high specific heat capacity of the host rock and residually trapped water. In both cases of deep and shallow reservoirs, near the injection point, temperature declined with increasing distance and some distance away it recovered back to its initial value. The temperature decline was attributed to the expansion of the CO_2 as it migrates away from the injection well and experiences continuously decreasing pressures. However, the very small magnitude of the temperature change suggested that, at least for the pressures considered here (>10 MPa), temperature can safely be assumed constant for future simulations.

Moreover, to investigate the significance of gravity in this context, a 2D radial model was developed. The 2D results suggested that as CO_2 is injected, it evaporates all the water around the well, thus mobilising the initially dissolved and residually-trapped methane. Owing to it being the lightest component, CH_4 then travels faster and accumulates ahead of the CO_2. However, due to significant density differences, CH_4 quickly rises to the top of the formation. During this process, it is replaced by the fresh reservoir water from below, which residually traps some of the mobilised gas. In other words, CH_4 is being mobilised due to injection of CO_2, and at the same time being trapped due to upward/downward motion of the gas/liquid phases, which could have significant adverse effects on the gas recovery in the case of injection into the water-leg. Furthermore, comparison of the vertically-averaged 2D results to the 1D analytical solution suggested that, gravity tends to smear-out the sharp fronts in a diffusion-like manner, which is expected as vertical-averaging in presence of gravitational forces introduces an additional diffusive term into the Darcy's flux of each of the phases.

Next was to simulate EGR in the low-pressure gas-leg of a partially-depleted reservoir, in particular the North Morecambe gas field. Effects of gravity on the gas recovery were investigated by monitoring the volume of the mobile methane throughout the simulations. It was found that the volume of mobile methane is almost constant at all times; the slight decrease in the mobile methane was attributed to the mobilised water which traps a small amount of gas on its way to the bottom of the reservoir (due to buoyancy). However, given the magnitude of this decrease in the volume of mobile CH_4, it was concluded that in the case of injection into the gas-leg of a reservoir, the gravity effects can be ignored. Neglecting gravity enabled us to use the so-called five-spot well-pattern for the rest of the simulations; accordingly, simulations were carried out using the five-spot pattern for a period of 20 years of injection+production. Unlike injection into the high-pressure water-leg, in the case of injection into the low-pressure gas-leg, temperature was found to decrease a few degrees around the injection and production wells (up to 3 ^oC).

The results suggest an ultimate recovery potential of around 5% of the GIIP, assuming it will be economic to drill sufficient number of additional wells to fill the entire reservoir's volume with CO_2 and thus produce all of the recoverable CH_4. For more realistic scenarios, an economic feasibility study was performed, taking into account the simulated incremental recovery potential, global wellhead CH4 prices, offshore drilling costs, CO_2 supply cost and UK's Carbon Price Floor (CPF). It was assumed that CO_2 supply cost ranges from 10 US$/tonne to 75 US$/tonne and offshore drilling cost in the east Irish Sea Basin area is around 10 million US$ per well. Both current value of 23 US$/tonne of emission, and the 2020 projected value of 37 US$/tonne of emission, for UK's CPF were used in the revenue estimations. Under these circumstances, the no-drilling scenario was found to be the most economically viable option. For such an option, incremental EGR potential is around 0.7% of GIIP, translating to 0.22 BSCM of gas volume can be expected. In this case, the revenue generated from the CH_4 sales plus the savings on CO_2 emission tax (due to

CPF) breaks even with the operating costs when the CO_2 supply cost is less than 50 US$/tonne, using the current CPF value, and less than 63 US$/tonne, assuming the projected value of 2020 CPF in the UK. Nonetheless, assuming an average CO_2 supply cost of 50 US$/tonne, by 2020, CO_2-EGR in the North Morecambe field can generate a revenue of around 13 million US$ at no extra cost. However, if the future CO_2/CH_4 markets involve payments to operators willing to store the CO_2, an upwards shift in CH_4 prices, and/or a reduction in CO_2 supply cost due to advancements in capture technologies, etc., the economics of CO_2-EGR will improve dramatically, leading to an economically viable incremental EGR potential of 5% of the GIIP, equivalent to over 2 BSCM of CH_4 volume.

8.3 FUTURE WORK

Our numerical model is only capable of modelling three components. However, real hydrocarbon displacement by gas injection, involves many more than the three components. For instance, any crude oil contains at least hundreds of components, and injection gases often contain more than four. Consequently, for a comprehensive compositional model, one that captures all the effects that influence gas injection processes, one must deal with multicomponent systems. It is unlikely however, that numerical calculations of the displacement processes will be performed with hundreds of components, nor is there a need to do so, since, currently there seems to be a considerable computational experience suggesting that phase behavior can be calculated for most gas/oil systems with acceptable accuracy with somewhere between five and fifteen components (Orr, 2007, p. 161).

Therefore, the natural extension to this work would be to construct numerical solutions for systems with a modest but arbitrary number of components. To do this, the equilibrium model of Chapter 3 needs to be extended to multi-components. The author believes that no matter how many components are present, the elements that

are combined to construct the equilibrium models are all generalisations of the key results of the two- and three-component ones, i.e., a series of binary-mixture models + linear interpolations between the key tie-lines (this is assuming constant-K values, which is often the case in hydrocarbon systems). Other than that, the framework of our numerical MOL code is already such that it easily allows for multicomponent set-up, i.e., only one more equation needs to be solved per extra component added.

9

APPENDIX(1) - THERMODYNAMICS OF PHASE EQUILIBRIUM

9.1 INTRODUCTION

In multicomponent flow systems, for a given pressure and temperature, there exists an equilibrium composition for each component, that defines the maximum concentration of each component and controls appearance/disappearance of a multiphase state. For instance, consider a single phase mixture of water containing dissolved CO_2. Continuous addition of CO_2 to this mixture will result in increased concentration of the dissolved CO_2, to the point where the partial pressure of the dissolved gas exceeds the liquid pressure. This concentration threshold is the equilibrium concentration. At this concentration, a gas bubble forms which in turn leads to appearance of a separate gas phase. As equilibrium is re-established and the gas phase is saturated with evaporated water, the initially single phase mixture has turned into two phases in equilibrium with one another. Equilibrium phase calculations are often carried out using the concept of "thermodynamic potential".

A thermodynamic potential is a state-variable which is minimised at equilibrium, subject to certain constraints. This means that if we want to compare two thermodynamic-states, S^I and S^{II}, of the same system to see which is the more stable one, i.e. in which direction the spontaneous change will go, the two state-variables must be the same in both S^I and S^{II}, and these two variables are called the constraints on the system (Anderson, 2009, p. 66).

For example, in a multiphase multicomponent mixture, one may want to know the equilibrium compositions of all the phases at temperature T and pressure P. In this case, there is a range of values for the thermodynamic potential (precisely one for every possible composition of the phases involved), and we need to find the minimum value of the potential. For any other value greater than this minimum, some change in composition (phases will dissolve, precipitate, etc.) will take place until the minimum value is achieved. Therefore, on the path to reaching the equilibrium state, one would speak of minimising the thermodynamic potential at constraints T and P.

9.1.1 *Gibbs energy and chemical potential*

The Gibbs free energy, G [M L^2 T^{-2}], has units of Joules and is a thermodynamic potential. Just as in mechanics, where potential energy is defined as the capacity to do work, G is the maximum amount of non-expansion (non-mechanical) work that can be extracted from a thermodynamic system, e.g., the amount of energy available for things like chemical reactions or phase transitions.

For a multi-component mixture:

$$G = \sum_{i=1}^{N_c} N_i \overline{g}_i \tag{9.1}$$

where N_c [-] is the number of components, N_i [N] is the number of moles for component i present and $\overline{g}_i$ is the Gibbs energy per mole (molar Gibbs energy) of component i. The total derivative of Eq. (9.1) with P and T held constant (as these are the constraints on the system), takes the form:

$$dG]_{T,P} = \sum_{i=1}^{N_c} \overline{g}_i dN_i \tag{9.2}$$

Note that the $\overline{g}_i$ terms are independent of composition.

The molar Gibbs energy term, $\overline{g}_i$ is often referred to as the chemical potential of component i and symbolised by μ_i (Cengel & Boles, 2002, p. 698) (i.e., $\mu_i \equiv \overline{g}_i$; not to be confused with viscosity). Therefore:

$$dG]_{T,P} = \sum_{i=1}^{N_c} \mu_i dN_i \tag{9.3}$$

The chemical potential is of particular importance when it comes to equilibrium calculations. Because the requirements for chemical equilibrium can be stated concisely in terms of the chemical potential.

9.1.2 *Criterion for chemical equilibrium*

Consider a simple compressible system of fixed mass at fixed temperature T and pressure P. Combining the 1^{st} and the 2^{nd} law of thermodynamics for this system gives (Cengel & Boles, 2002, p. 794):

$$\left.\begin{array}{c} dQ - PdV = dU \\ dS \geq \frac{dQ}{T} \end{array}\right\} \quad \Rightarrow \quad dU + PdV - TdS \leq 0 \tag{9.4}$$

where Q [$\mathrm{ML^2T^{-2}}$] is the heat added to the system, U [$\mathrm{ML^2T^{-2}}$] is internal energy, S [$\mathrm{L^2T^{-2}}$] is the entropy and V [$\mathrm{L^3}$] is the volume.

The Gibbs free energy for this system is then given by:

$$G = U - TS + PV \tag{9.5}$$

On differentiation at constant pressure and temperature thus yields:

$$dG]_{T,P} = dU + PdV - TdS \tag{9.6}$$

From Eqs. (9.4) and (9.6) it can be understood that:

$$dG]_{T,P} \leq 0 \tag{9.7}$$

and for multi-component systems according to Eq. (9.3):

$$dG]_{T,P} = \sum_{i=1}^{N_c} \mu_i dN_i \leq 0 \tag{9.8}$$

Eq. (9.8) states that a chemical reaction at a specified temperature and pressure proceeds in the direction of a decreasing Gibbs energy. Therefore, chemical equilibrium is established when the Gibbs function reaches the absolute minimum value i.e. zero. Thus, for multicomponent mixtures, the criterion for chemical equilibrium is expressed as (Cengel & Boles, 2002, p. 795):

$$dG]_{T,P} = \sum_{i=1}^{N_c} \mu_i dN_i = 0 \tag{9.9}$$

9.1.3 *Criterion for phase equilibrium*

A special case of chemical equilibrium is in non-reacting multiphase systems which is of particular interest to this work. Consider a single component mixture of a saturated liquid in equilibrium with its vapour. The total Gibbs energy of this mixture is given by:

$$G = \bar{g}_v N_v + \bar{g}_l N_l \tag{9.10}$$

where subscripts v and l denote the vapour and liquid phases respectively. N_j [N] is the number of moles of phase j and $\bar{g}_j$ is the molar Gibbs energy which is analogous to the as chemical potential (μ_j). It follows:

$$G = \mu_v N_v + \mu_l N_l \tag{9.11}$$

Note that $\bar{g}_j$ and μ_j are independent of changes in mass (or number of moles).

Now consider a disturbance during which dN_l amount of liquid evaporates into the vapour phase at constant pressure and temperature. Then the change in the total Gibbs energy is given by:

$$dG]_{T,P} = \mu_v dN_v + \mu_l dN_l \tag{9.12}$$

At equilibrium $dG = 0$ and also from conservation of mass, $dN_v = -dN_l$. It then follows:

$$dG]_{T,P} = (\mu_l - \mu_v) dN_l = 0 \tag{9.13}$$

which yields:

$$\mu_l = \mu_v \tag{9.14}$$

Therefore, the two phases of a pure substance are in equilibrium when the chemical potential of the phases are the same. For a mixture of N_c number of components in N_p number of phases, using the same logic, it can be shown that the requirement for phase equilibrium can be stated as (Cengel & Boles, 2002, p. 810):

$$\mu_{ij} = \mu_{ik} \quad i \in [1, ..., N_c] \quad , \quad j \in [1, ..., N_p], \quad , \quad k \in [1, ..., N_p] \quad , \quad j \neq k \tag{9.15}$$

9.1.4 *Chemical potential in terms of molar volume*

To derive useful expressions for calculating the chemical potentials, μ_i, it is useful to derive a relationship between μ_i and the corresponding molar enthalpies and entropies, $\overline{h}_i$ and $\overline{s}_i$, respectively. The Gibbs energy can also be defined in terms of enthalpy per unit volume, H [$\mathrm{ML^{-1}T^{-2}}$], and entropy per unit volume, S [$\mathrm{L^{-1}T^{-2}}$]:

$$G = H - TS \tag{9.16}$$

where for a multi-component system:

$$H = \sum_{i=1}^{N_c} N_i \overline{h}_i \tag{9.17}$$

$$S = \sum_{i=1}^{N_c} N_i \overline{s}_i \tag{9.18}$$

Inspection of Eq. (9.1) reveals that:

$$\mu_i \equiv \overline{g}_i = \overline{h}_i - T\overline{s}_i \tag{9.19}$$

The total derivative of Eq. (9.19) takes the form:

$$d\mu_i = d\overline{h}_i - Td\overline{s}_i - \overline{s}_i dT \tag{9.20}$$

and it happens that:

$$d\overline{h}_i = Td\overline{s}_i + \overline{v}_i dP_i \tag{9.21}$$

which on substitution into Eq. (9.20) leads to:

$$d\mu_i = \overline{v}_i dP_i - \overline{s}_i dT \tag{9.22}$$

from which it can be seen that:

$$\left(\frac{\partial \mu_i}{\partial P_i}\right)_T = \overline{v}_i \tag{9.23}$$

The above equation is important because it enables the possibility of acquiring chemical potential values directly from PVT data.

9.1.5 *Chemical potential for ideal gas mixtures*

Here we will derive expressions for μ_i in term of corresponding partial pressure, P_i, under the assumption that the components of a mixture conform to that associated with an ideal gas. The molar volume of an ideal gas for component i, $\overline{v}_i$ [$\mathrm{L^3N^{-1}}$], can be found from:

$$\overline{v}_i = \frac{\overline{R}T}{P_i} \tag{9.24}$$

where P_i is the partial pressure of component i and $\overline{R}$ [$\mathrm{L^2T^{-2}K^{-1}N^{-1}}$] is the ideal gas constant in molar form.

Substituting Eq. (9.24) into Eq. (9.23) and integrating with respect to P_i leads to:

$$\mu_i = \mu_i^0 + \overline{R}T \ln\left(\frac{P_i}{P_{\mathrm{ref}}}\right) \tag{9.25}$$

where P_{ref} is a reference pressure at which $\mu_i = \mu_i^0$.

9.1.6 *Chemical potentials for non-ideal gas mixtures*

The definition for μ_i in Eq. (9.25) only applies to ideal gases. However, let us define the term "fugacity" for component i, f_i, such that for a non-ideal gas:

$$\mu_i = \mu_i^0 + \overline{R}T \ln\left(\frac{f_i}{P_{\text{ref}}}\right) \tag{9.26}$$

where f_i [M L^{-1} T^{-2}] is the fugacity of component i and has the same units as pressure. f_i is essentially the partial pressure of component i in a non-ideal gas mixture. Fugacity can be related to the partial pressure of an ideal mixture. For an ideal gas mixture, partial pressure of each gas species, P_i [M L^{-1} T^{-2}], can be calculated using Dalton's law:

$$P_i = n_i P \tag{9.27}$$

where n_i [-] is the mole fraction of the i^{th} component.
To account for non-ideality, a term fugacity coefficient, ϕ_i [-], is often defined such that:

$$f_i = \phi_i P_i \tag{9.28}$$

The fugacity coefficient, ϕ_i [-], is a measure of deviation from ideality, in such a way that:

$$\phi_i = \frac{f_i}{P_i} \to 1 \qquad as \qquad P_i \to 0 \tag{9.29}$$

Substituting Eq. (9.27)in Eq. (9.28):

$$f_i = \phi_i n_i P \tag{9.30}$$

9.1.7 *Chemical potential for solutions*

The expression for the chemical potential for an ideal gas mixture, Eq. (9.25), can also be used to derive an expression for chemical potential in an ideal solution.

An ideal solution is a solution where the total vapour pressure, P, is given by Raoult's Law:

$$P = \sum_{i=1}^{N_c} n_i P_i^* \tag{9.31}$$

where n_i is the mole fractions of component i and P_i^* is the vapour pressure of the pure component i. The partial pressure, P_i, is found from:

$$P_i = n_i P_i^* \tag{9.32}$$

If the vapour behaves as an ideal gas, the chemical potential of component i in the vapour phase will accord to Eq. (9.25). At equilibrium, the chemical potential of component i in the vapour phase will be equal to that in the liquid phase. Therefore Eq. (9.25) can be said to apply to the liquid phase as well.
Substituting Eq. (9.32) into Eq. (9.25) leads to:

$$\mu_i = \mu_i^0 + \overline{R}T \ln\left(\frac{P_i^*}{P_{\text{ref}}}\right) + \overline{R}T \ln n_i \tag{9.33}$$

from which it can be said that:

$$\mu_i = \mu_i^* + \overline{R}T \ln n_i \tag{9.34}$$

where $\mu_i = \mu_i^*$ when $n_i = 1$.

9.1.8 *Chemical potential for non-ideal solutions*

The definition for μ_i in Eq. (9.34) above only applies to ideal solutions. However, let us define the term "activity" for component i, a_i, such that for a non-ideal solution:

$$\mu_i = \mu_i^* + \overline{R}T \ln a_i \tag{9.35}$$

where

$$a_i = \gamma_i n_i \tag{9.36}$$

a_i [-] is activity of component i and is a measure of effective concentration of species i in the non-ideal mixture such that:

$$\gamma_i = \frac{a_i}{n_i} \to 1 \qquad as \qquad n_i \to 0 \ or \ 1 \tag{9.37}$$

In other words, the behaviour of component i in a real solution approaches ideal, either when $n_i \to 1$ for pure component i, or when $n_i \to 0$ for infinite dilution of component i.

9.1.9 *Equilibrium constants*

An equilibrium constant, K_i (also known as K-value), is a measure of reactivity. Note that reaction does not necessarily have to be a chemical one, e.g., phase-transition is considered as a non-chemical reaction. If K_i is very large, it indicates that a reaction will tend to go to completion, and if K_i is small, it indicates that the reaction hardly occurs (Anderson, 2005, p. 240). The equilibrium constants are important because they can be used to calculate the mole fraction of each chemical species at equilibrium. This section provides an expression relating K-values to pressure and temperature.

Consider a multi-component mixture of non-ideal gas and non-ideal solution. Let f_i denote the fugacities of each component in the gas phase and a_i the activities of each component in the liquid phase. K_i is defined by:

$$K_i = \frac{f_i}{P_{\text{ref}} a_i} \tag{9.38}$$

The chemical potentials of each component in the gas and liquid phases can be calculated from Eqs. (9.26) and (9.35), respectively. According to Eq. (9.15), when the phases are in equilibrium, their chemical potentials should be equal. Therefore it can be said that:

$$\mu_i^0 + \overline{R}T \ln\left(\frac{f_i}{P_{\text{ref}}}\right) = \mu_i^* + \overline{R}T \ln a_i \tag{9.39}$$

from which it follows:

$$\ln K_i = \frac{\mu_i^* - \mu_i^0}{\overline{R}T} \tag{9.40}$$

Recall that μ_i^* is the chemical potential of pure component i when $P_i = P_i^*$, where P_i^* is the vapour pressure of the pure component i.

Considering Eq. (9.23), differentiating Eq. (9.40) with respect to pressure and noting that μ_i^0 is the chemical potential at $P = P_{ref}$ and therefore does not vary with pressure:

$$\left[\frac{\partial}{\partial P}(\ln K_i)\right]_T = \frac{\overline{v}_i^*}{\overline{R}T} \tag{9.41}$$

from which it follows that:

$$K_i = K_i^0 \exp\left(\int_{P_{\text{ref}}}^{P_i^*} \frac{\overline{v}_i^*}{\overline{R}T} dP\right) \tag{9.42}$$

which is often written in the form:

$$K_i = K_i^0 \exp\left[\frac{(P_i^* - P_{\text{ref}})\overline{V_i}}{\overline{R}T}\right] \tag{9.43}$$

where:

$$\overline{V_i} = \frac{1}{P_i^* - P_{\text{ref}}} \int_{P_{\text{ref}}}^{P_i^*} \overline{v}_i^* dP_i^* \tag{9.44}$$

Next is to calculate equilibrium mole fractions using Eq. (9.43) for binary mixtures of CO_2-H_2O and CH_4-H_2O.

9.2 BINARY CO_2-H_2O EQUILIBRIUM

This section describes the binary equilibrium model for CO_2-H_2O mixture, proposed by Spycher et al. (2003). Using the information provided in previous sections, the aim is to obtain expressions for calculation of the n_{ij} terms, which are the mole fractions of component i in phase j at equilibrium, such that:

$$\sum_{i=1}^{N_c} n_{ij} = 1 \tag{9.45}$$

We start by substituting the expressions for Fugacity and Activity, Eqs. (9.30) and (9.36), into Eq. (9.43). After some rearrangement:

$$n_{H_2O(g)} = \frac{K^0_{H_2O} a_{H_2O}}{\phi_{H_2O} P} \exp\left(\frac{\overline{V}_{H_2O(l)}}{\overline{R}T}[P^*_{H_2O} - P_{\text{ref}}]\right) \tag{9.46}$$

Spycher et al. (2003) argue that CO_2 solubility in water is sufficiently small (infinite dilution assumption) that Raoult's law can be used to set the water activity, a_{H_2O}, equal to its mole fraction in the water phase, $n_{H_2O(l)}$. Applying this assumption and using Eq. (9.45), then Eq. (9.46) becomes:

$$n_{H_2O(g)} = \frac{K^0_{H_2O}(1 - n_{CO_2(l)})}{\phi_{H_2O} P} \exp\left(\frac{\overline{V}_{H_2O(g)}}{\overline{R}T}[P^*_{H_2O} - P_{\text{ref}}]\right) \tag{9.47}$$

Spycher et al. (2003) calculate the activity coefficient of CO_2 on a molality scale as opposed to mole-fraction scale, with the convention that:

$$a_{CO_2} = \gamma_{CO_2} m_{CO_2} \tag{9.48}$$

where m_{CO_2} [NM^{-1}] is the molality of CO_2, which is moles of CO_2 per kg of water and is given by:

$$m_{CO_2} = \frac{n_{CO_2(l)}}{M_{H_2O}} \tag{9.49}$$

where $M_{H_2O} = 0.018015$ [MN^{-1}] is the molar mass of water. Substituting Eq. (9.49) in Eq. (9.48), gives the activity of CO_2 on a mole-fraction scale:

$$a_{CO_2} = 55.508 n_{CO_2(l)} \tag{9.50}$$

To obtain mole fraction of CO_2 in the liquid phase, $n_{CO_2(l)}$, we substitute fugacity and activity expressions, Eqs.(9.30) and (9.50) in Eq. (9.43). After rearrangement:

$$n_{CO_2(l)} = \frac{\phi_{CO_2}(1 - n_{H_2O(g)})P}{55.508 K^0_{CO_2}} \exp\left(-\frac{\overline{V}_{CO_2(l)}}{\overline{R}T}[P^*_{CO_2} - P_{\mathrm{ref}}]\right) \tag{9.51}$$

Eqs. (9.47) and (9.51) provide the two equations to obtain the two unknowns, $n_{H_2O(g)}$ and $n_{CO_2(l)}$:

$$n_{H_2O(g)} = \frac{1 - W}{1/Q - W} \qquad \& \qquad n_{CO_2(l)} = W(1 - n_{H_2O(g)}) \tag{9.52}$$

where Q and W are:

$$Q = \frac{K^0_{H_2O}}{\phi_{H_2O} P} \exp\left(\frac{\overline{V}_{H_2O(g)}}{\overline{R}T}[P^*_{H_2O} - P_{\mathrm{ref}}]\right) \tag{9.53}$$

$$W = \frac{\phi_{CO_2} P}{55.508 K^0_{CO_2}} \exp\left(-\frac{\overline{V}_{CO_2(l)}}{\overline{R}T}[P^*_{CO_2} - P_{\text{ref}}]\right) \tag{9.54}$$

$n_{H_2O(l)}$ and $n_{CO_2(g)}$ can then be calculated using Eq. (9.45).

The fugacity coefficients, ϕ_i [-], are calculated using the empirical correlation below:

$$\ln(\phi_i) = \ln\left(\frac{V_i}{V_i - B_{mix}}\right) + \left(\frac{B_i}{V_i - B_{mix}}\right) - 2\ln\left(\frac{V_i + B_{mix}}{V_i}\right)\sum_{k=1}^{N_c} n_i A_i \Big/ (RT^{1.5} B_{mix})$$

$$+ \frac{A_{mix} B_i}{RT^{1.5} B^2_{mix}}\left[\ln\left(\frac{V_i + B_i}{V_i}\right) - \left(\frac{B_{mix}}{V_i + B_{mix}}\right)\right] - \ln\left(\frac{PV_i}{RT}\right) \tag{9.55}$$

where A_i and B_i are the intermolecular attraction and repulsion parameters for component i and are given in Table 6. For the gas mixture, they are calculated using:

$$A_{mix} = n^2_{H_2O(g)} A_{H_2O} + 2 n_{H_2O(g)} n_{CO_2(g)} A_{H_2O-CO_2} + n^2_{CO_2(g)} A_{CO_2} \tag{9.56}$$

$$B_{mix} = n_{H_2O(g)} B_{H_2O} + n_{CO_2(g)} B_{CO_2} \tag{9.57}$$

It is apparent from Eq. (9.55) that ϕ_i depends on the mixture composition, n_{ij}. Therefore, Eq. (9.55) needs to be solved simultaneously with Eqs. (9.47) and (9.51) to compute the mutual solubilities of CO_2 and H_2O. This requires an iterative scheme that can add significant burden for implementation into an already computationally intensive fluid flow/transport model. However, Spycher et al. (2003) suggests to assume that $n_{H_2O(g)} = 0$ and $n_{CO_2(g)} = 1$ (i.e., assumption of infinite H_2O dilution in the CO_2-rich phase), for fugacity coefficients to be computed directly, in a non-iterative manner.

Parameter	Value
a_{CO_2}	6.21×10e7
b_{CO_2}	27.80
b_{H_2O}	18.18
$a_{H_2O-CO_2}$	7.89×10e7

Table 6: Attraction and repulsion parameters for CO_2-H_2O mixture.

Component	D_1	D_2	D_3	D_4
H_2O	-2.209	3.097 ×10e-2	-1.098 ×10e-4	2.048 ×10e-7
$CO_{2(g)}$	1.189	1.304 ×10e-2	-5.446 ×10e-4	0.0
$CO_{2(l)}$	1.169	1.368 ×10e-2	-5.380 ×10e-4	0.0

Table 7: Parameters of the empirical equation for evaluation of the equilibrium constant, K^0, for CO_2-H_2O mixture.

Finally, the K_i^0 values are calculated using the empirical correlation below:

$$\log(K_i^0) = D_1 + D_2T + D_3T^2 + D_4T^3 \tag{9.58}$$

Values for D_1 to D_4 are listed in Table 7 for CO_2 and H_2O.

9.3 BINARY CH_4-H_2O EQUILIBRIUM

This section describes the binary equilibrium model for CH_4-H_2O mixture, proposed by Duan & Mao (2006). Their approach is almost identical to that of Spycher et al. (2003) which was described in previous section. Here again capillary forces are assumed negligible:

$$P_g = P_l = P \tag{9.59}$$

Subscripts g and l denote the gas and liquid phases respectively.

The aim is to obtain expressions for calculation of the n_{ij} terms, which are the mole fractions of component i in phase j at equilibrium, such that:

$$\sum_{i=1}^{N_c} n_{ij} = 1 \tag{9.60}$$

We start by substituting the expressions for Fugacity and Activity, Eqs. (9.30) and (9.36), for H_2O into Eq. (9.43). After some rearrangement:

$$n_{H_2O(g)} = \frac{K^0_{H_2O} a_{H_2O}}{\phi_{H_2O} P} \exp\left(\frac{\overline{V}_{H_2O(l)}}{\overline{R}T}[P^*_{H_2O} - P_{\text{ref}}]\right) \tag{9.61}$$

Where again the CH_4 solubility in water is so small that Raoult's law can be used to set the water activity, a_{H_2O}, equal to its mole fraction in the water phase, $n_{H_2O(l)}$. Applying this assumption and using Eq. (9.60), then Eq. (9.61) becomes:

$$n_{H_2O(g)} = \frac{K^0_{H_2O}(1 - n_{CH_4(l)})}{\phi_{H_2O} P} \exp\left(\frac{\overline{V}_{H_2O(l)}}{\overline{R}T}[P^*_{H_2O} - P_{\text{ref}}]\right) \tag{9.62}$$

For evaluation of $K^0_{H_2O} = \frac{f_{H_2O}}{a_{H_2O}}$, due to infinite dilution of CH_4 in H_2O phase, $a_{H_2O} = 1$ and therefore $K^0_{H_2O}$ is equal to the fugacity (partial pressure) of water in the gas phase. Furthermore, the partial pressure of water in vapour is approximated as the saturated pressure of pure water, such that:

$$K^0_{H_2O} = f_{H_2O} = P^*_{H_2O} \tag{9.63}$$

Substituting Eq. (9.63) in Eq. (9.62) leads to:

$$n_{H_2O(g)} = \frac{P^*_{H_2O}(1 - n_{CH_4(l)})}{\phi_{H_2O} P} \exp\left(\frac{\overline{V}_{H_2O(l)}}{\overline{R}T}[P^*_{H_2O} - P_{\text{ref}}]\right) \tag{9.64}$$

Parameter	Value
C_1	-1.42006707 $\times 10^{-2}$
C_2	1.08369910 $\times$ 10^{-2}
C_3	-1.59213160 $\times$ 10^{-6}
C_4	-1.10804676 $\times$ 10^{-5}
C_5	-3.14287155 $\times$ 10^{0}
C_6	1.06338095$\times$ 10^{-3}

Table 8: Parameters of empirical equation for water fugacity.

On the other hand, since there is little water in the vapour phase, the fugacity coefficient of CH_4 in gas phase differs little from that of pure CH_4 at the pressure and temperature ranges of interest. Therefore:

$$n_{CH_4(g)} = 1 - n_{H_2O(g)} = \frac{P - P^*_{H_2O}}{P} \tag{9.65}$$

The only remaining parameter to be evaluated is the fugacity coefficient of water, which can be calculated from the following equation:

$$\phi_{H_2O} = \exp\left(C_1 + C_2 P + C_3^2 + C_4 PT + C_5 \frac{P}{T} + C_6 \frac{P^2}{T}\right) \tag{9.66}$$

Where C_1 to C_6 are listed in Table 8.

Eqs. (9.64), (9.65) and (9.60) provide the necessary information to calculate all of the n_{ij} terms for the CH_4-H_2O mixture.

BIBLIOGRAPHY

Afanasyev, A. A. (2013). Multiphase compositional modelling of CO2 injection under subcritical conditions: the impact of dissolution and phase transitions between liquid and gaseous CO2 on reservoir temperature. International Journal of Greenhouse Gas Control, 19, 731-742.

Al-Hasami, A., Ren, S., & Tohidi, B. (2005). CO2 injection for enhanced gas recovery and geo-storage: reservoir simulation and economics. In SPE Europec/EAGE Annual Conference. Society of Petroleum Engineers.

Anderson, G.M., 2009. Thermodynamics of natural systems. Cambridge University Press.

Amaziane, B., Jurak, M., & Zgaljic-Keko, A. (2012, September). Modeling compositional compressible two-phase flow in porous media by the concept of the global pressure. Computational Geosciences, 18, 297-309.

Andre, L., Azaroual, M., & Menjoz, A. (2010). Numerical simulations of the thermal impact of supercritical CO2 injection on chemical reactivity in a carbonate saline reservoir. Transport in porous media, 82(1), 247-274.

Anderson, G. M. (2005). Thermodynamics of natural systems. Cambridge University Press.

Ashino, R., Nagase, M. and Vaillancourt, R., 2000. Behind and beyond the MATLAB ODE suite. Computers & Mathematics with Applications, 40(4), pp.491-512.

Bajura, R. A. (2001). The role of carbon dioxide sequestration in the long term energy future. Greenhouse Gas Control Technologies-GHGT, 5, 52-58.

Barrufet, M. A., Bacquet, A., & Falcone, G. (2010). Analysis of the storage capacity for CO2 sequestration of a depleted gas condensate reservoir and a saline aquifer. Journal of Canadian Petroleum Technology, 49(08), 23-31.

Battistelli, A., & Marcolini, M. (2009). TMGAS: a new TOUGH2 EOS module for the numerical simulation of gas mixtures injection in geological structures. International Journal of Greenhouse Gas Control, 3, 481-493.

Bear, J., 2013. Dynamics of fluids in porous media. Courier Corporation.

Bentham, M., & Kirby, M. (2005). CO2 storage in saline aquifers. Oil & gas science and technology, 60(3), 559-567.

Bergman, P. D., Winter, E. M., & Chen, Z. Y. (1997). Disposal of power plant CO2 in depleted oil and gas reservoirs in Texas. Energy Conversion and Management, 38, S211-S216.

Blok, K., Williams, R. H., Katofsky, R. E.,& Hendriks, C. A. (1997). Hydrogen production from natural gas, sequestration of recovered CO 2 in depleted gas wells and enhanced natural gas recovery. Energy, 22(2), 161-168.

Bourgeat, A., Jurak, M., & Smai, F. (2013). On persistent primary variables for numerical modeling of gas migration in a nuclear waste repository. Computational Geosciences, 17, 287-305.

Bryant, E. (1997). Climate process and change. Cambridge University Press.

Buckley, S. E., & Leverett, M. (1942). Mechanism of fluid displacement in sands. Transactions of the AIME, 146(01), 107-116.

Cengel, Y. A., & Boles, M. A. (2002). Thermodynamics: an engineering approach (Vol. 5). M. Kanoglu (Ed.). New York: McGraw-Hill.

Chen, Z., Huan, G., & Ma, Y. (2006). Computational methods for multiphase flows in porous media. SIAM.

Clemens, T., & Wit, K. (2002). CO2 enhanced gas recovery studied for an example gas reservoir. In SPE Annual Technical Conference and Exhibition. Society of Petroleum Engineers.

Connell, L. D., & Detournay, C. (2009). Coupled flow and geomechanical processes during enhanced coal seam methane recovery through CO 2 sequestration. International Journal of Coal Geology, 77(1), 222-233.

Corey, A. T. (1954). The interrelation between gas and oil relative permeabilities. Producers monthly, 19(1), 38-41.

Cowan, G., & Boycott-Brown, T. (2003). The North Morecambe Field, Block 110/2a, East Irish Sea. Geological Society, London, Memoirs, 20(1), 97-105.

Damen, K., Faaij, A., & Turkenburg, W. (2006). Health, safety and environmental risks of underground CO2 storage - overview of mechanisms and current knowledge. Climatic Change, 74(1-3), 289-318.

David, J., & Herzog, H. (2000, August). The cost of carbon capture. In fifth international conference on greenhouse gas control technologies, Cairns, Australia (pp. 13-16).

Department of Energy and Climate Change (DECC). Dry Gas Production by Field - Morecambe North. Accessible from: https://itportal.decc.gov.uk/pprs/full_production.htm [Accessed:03/10/2016]

Duan, Z. and Mao, S., 2006. A thermodynamic model for calculating methane solubility, density and gas phase composition of methane-bearing aqueous fluids from 273 to 523K and from 1 to 2000bar. Geochimica et Cosmochimica Acta, 70(13), pp.3369-3386.

Goudarzi S. and Mathias S.A. & Gluyas J.G. (2016). Simulation of three-component two-phase flow in porous media using method of lines. Transport in Porous Media, 112(1), 1-19.

UK Government's Website. Carbon price floor: reform. Accessible from: https://www.gov.uk/government/publications/carbon-price-floor-reform [Accessed:21/11/2016]

Gozalpour, F., Ren, S. R., & Tohidi, B. (2005). CO2-EOR and storage in oil reservoir. Oil & gas science and technology, 60(3), 537-546.

Gresham, R. L., McCoy, S. T., Apt, J., & Morgan, M. G. (2010). Implications of compensating property owners for geologic sequestration of CO2. Environmental science & technology, 44(8), 2897-2903.

Haszeldine, R.S., (2009). Carbon capture and storage: how green can black be?. Science, 325(5948), pp.1647-1652.

Han, W. S., Stillman, G. A., Lu, M., Lu, C., McPherson, B. J., & Park, E. (2010). Evaluation of potential nonisothermal processes and heat transport during CO2 sequestration. Journal of Geophysical Research: Solid Earth (1978-2012), 115(B7).

Han, W. S., Kim, K. Y., Park, E., McPherson, B. J., Lee, S. Y., & Park, M. H. (2012). Modeling of spatiotemporal thermal response to CO2 injection in saline formations: interpretation for monitoring. Transport in porous media, 93(3), 381-399.

Hosseini, S. A., Mathias, S. A., & Javadpour, F. (2012). Analytical model for CO2 injection into brine aquifers-containing residual CH4. Transport in porous media, 94(3), 795-815.

Hubbert, M. K. (1956). Darcy's law and the field equations of the flow of underground fluids. Shell Development Company, Exploration and Production Research Division.

Hussen, C., Amin, R., Madden, G., & Evans, B. (2012). Reservoir simulation for enhanced gas recovery: an economic evaluation. Journal of Natural Gas Science and Engineering, 5, 42-50.

Ireson, A. M., Mathias, S. A., Wheater, H. S., Butler, A. P., & Finch, J. (2009). A model for flow in the chalk unsaturated zone incorporating progressive weathering. Journal of Hydrology, 365(3), 244-260.

Jepma, C. J., & Munasinghe, M. (1998). Climate change policy: Facts, issues and analyses. Cambridge University Press.

Jikich, S. A., Smith, D. H., Sams, W. N., & Bromhal, G. S. (2003). Enhanced Gas Recovery (EGR) with carbon dioxide sequestration: A simulation study of effects of injection strategy and operational parameters. In SPE Eastern Regional Meeting. Society of Petroleum Engineers.

Juanes, R. (2008). A robust negative flash based on a parameterization of the tie-line field. Fluid Phase Equilibria, 267(1), 6-17.

Juanes, R., 2008, January. A globally-convergent flash calculation for constant K-values based on a parameterization of the tie-line field. In SPE Symposium on Improved Oil Recovery. Society of Petroleum Engineers.

Khan, S., Han, H., Ansari, S. A., & Khosravi, N. (2010, January). An integrated geomechanics workflow for Caprock-integrity analysis of a potential carbon storage. In SPE International Conference on CO2 Capture, Storage, and Utilization. Society of Petroleum Engineers.

Kuhn, M., Tesmer, M., Pilz, P., Meyer, R., Reinicke, K., Faurster, A., ... & Schadfer, D. (2012). CLEAN: project overview on CO2 large-scale enhanced gas recovery in the Altmark natural gas field (Germany). Environmental Earth Sciences, 67(2), 311-321.

Laney, C. B. (1998). Computational gasdynamics. Cambridge University Press.

Lemmon, E. W., McLinden, M. O., & Friend, D. G. (2011). Thermophysical Properties of Fluid Systems In NIST Chemistry WebBook, NIST Standard Reference Database Number 69, Linstrom, P. J., Mallard, WG, Eds.

LeVeque, R. J., & Randall. J. (1992). Numerical methods for conservation laws (Vol. 132). Basel: BirkhÃďuser.

Li, H., & Li, G. (2010, January). Modeling surface heave induced by hydraulic fracturing stimulation and CO2 injection into coal seams. In 44th US Rock Mechanics Symposium and 5th US-Canada Rock Mechanics Symposium. American Rock Mechanics Association.

Li, Y., Johns, R.T. and Ahmadi, K., 2012. A rapid and robust alternative to RachfordâĂŞRice in flash calculations. Fluid Phase Equilibria, 316, pp.85-97.

Liu, F., Ellett, K., Xiao, Y., & Rupp, J. A. (2013). Assessing the feasibility of CO2 storage in the New Albany Shale (Devonian-Mississippian) with potential enhanced gas recovery using reservoir simulation. International Journal of Greenhouse Gas Control, 17, 111-126.

Loizzo, M., Lecampion, B., Berard, T., Harichandran, A., & Jammes, L. (2010). Reusing O&G-Depleted Reservoirs for CO2 Storage: Pros and Cons. SPE Projects, Facilities & Construction, 5(03), 166-172.

Mallison, B. T., Gerritsen, M. G., Jessen, K., & Orr, F. M. (2005). High order upwind schemes for two-phase multicomponent flow. SPE Journal, 10, 297-311.

Marle, C. (1981). Multiphase flow in porous media. Editions technip.

Martens, S., Kempka, T., Liebscher, A., Luth, S., Moller, F., Myrttinen, A., ... & Kuhn, M. (2012). Europe's longest-operating on-shore CO2 storage site at Ketzin, Germany: a progress report after three years of injection. Environmental Earth Sciences, 67(2), 323-334.

Mathias, S. A., Butler, A. P., Jackson, B. M., & Wheater, H. S. (2006). Transient simulations of flow and transport in the Chalk unsaturated zone. Journal of Hydrology, 330, 10-28.

Mathias, S. A., Butler, A. P., & Zhan, H. (2008). Approximate solutions for Forchheimer flow to a well. Journal of Hydraulic Engineering, 134, 1318-1325.

Mathias, S. A., Butler, A. P., & Wheater, H. S. (2008). Modelling radioiodine transport across a capillary fringe. Journal of Environmental Radioactivity, 99, 716-729.

Mathias, S. A., Hardisty, P. E., Trudell, M. R., & Zimmerman, R. W. (2009). Approximate solutions for pressure buildup during CO2 injection in brine aquifers. Transport in Porous Media, 79(2), 265-284.

Mathias, S. A., Gluyas, J. G., Oldenburg, C. M., & Tsang, C. F. (2010). Analytical solution for Joule-Thomson cooling during CO2 geo-sequestration in depleted oil and gas reservoirs. International Journal of Greenhouse Gas Control, 4(5), 806-810.

Mathias, S. A., de Miguel, G. J. G. M., Thatcher, K. E., & Zimmerman, R. W. (2011a). Pressure buildup during CO2 injection into a closed brine aquifer. Transport in porous media, 89(3), 383-397.

Mathias, S. A., Gluyas, J. G., Gonzalez Martinez de Miguel, G. J., & Hosseini, S. A. (2011b). Role of partial miscibility on pressure buildup due to constant rate injection of CO2 into closed and open brine aquifers. Water Resources Research, 47(12).

Mathias, S. A., Gluyas, J. G., de Miguel, G. J. G. M., Bryant, S. L., & Wilson, D. (2013). On relative permeability data uncertainty and CO2 injectivity estimation for brine aquifers. International Journal of Greenhouse Gas Control, 12, 200-212.

Mathias, S. A., McElwaine, J. N., & Gluyas, J. G. (2014). Heat transport and pressure buildup during carbon dioxide injection into depleted gas reservoirs. Journal of Fluid Mechanics, 756, 89-109.

Mavor, M. J., Gunter, W. D., & Robinson, J. R. (2004). Alberta multiwell micro-pilot testing for CBM properties, enhanced methane recovery and CO2 storage potential. In SPE Annual Technical Conference and Exhibition. Society of Petroleum Engineers.

Metz, B., Davidson, O., de Coninck, H., Loos, M., & Meyer, L. (2005). Carbon dioxide capture and storage.

Metz, B., Davidson, O., De Coninck, H. C., Loos, M., & Meyer, L. A. (2005). IPCC special report on carbon dioxide capture and storage. Prepared by Working Group III of the Intergovernmental Panel on Climate Change. IPCC, Cambridge University Press: Cambridge, United Kingdom and New York, USA, 4.

Mukhopadhyay, S., Yang, S. Y., & Yeh, H. D. (2012). Pressure buildup during supercritical carbon dioxide injection from a partially penetrating borehole into gas reservoirs. Transport in porous media, 91(3), 889-911.

Nordbotten, J.M. and Celia, M.A., 2006. Similarity solutions for fluid injection into confined aquifers. Journal of Fluid Mechanics, 561, pp.307-327.

Oldenburg, C. M. (2007). Joule-Thomson cooling due to CO2 injection into natural gas reservoirs. Energy Conversion and Management, 48(6), 1808-1815.

Oldenburg, C. M. (2003). Carbon sequestration in natural gas reservoirs: enhanced gas recovery and natural gas storage. Lawrence Berkeley National Laboratory.

Oldenburg, C. M., Pruess, K., & Benson, S. M. (2001). Process modeling of CO2 injection into natural gas reservoirs for carbon sequestration and enhanced gas recovery. Energy & Fuels, 15(2), 293-298.

Oldenburg, C. M., Stevens, S. H., & Benson, S. M. (2004). Economic feasibility of carbon sequestration with enhanced gas recovery (CSEGR). Energy, 29(9), 1413-1422.

Oldenburg, C. M., & Doughty, C. (2011). Injection, flow, and mixing of CO_2 in porous media with residual gas. Transport in Porous Media, 90, 201-218.

Orr, F. M. (2007). Theory of gas injection processes. Copenhagen: Tie-Line Publications.

Pittard, A. (1997). Field abandonment costs vary widely worldwide. Oil and Gas Journal, 95(11).

Pope, G. A. (1980). The application of fractional flow theory to enhanced oil recovery. Society of Petroleum Engineers Journal, 20, 191-205.

Press, W. H. (2007). Numerical recipes 3rd edition: The art of scientific computing. Cambridge university press.

Qin, J., Rosenbauer, R. J., & Duan, Z. (2008). Experimental measurements of vapor-liquid equilibria of the H2O+ CO2+ CH4 ternary system. Journal of Chemical & Engineering Data, 53(6), 1246-1249.

Ouellet, A., Berard, T., Desroches, J., Frykman, P., Welsh, P., Minton, J., ... & Schmidt-Hattenberger, C. (2011). Reservoir geomechanics for assessing containment in CO 2 storage: a case study at Ketzin, Germany. Energy Procedia, 4, 3298-3305.

Quintella, C. M., Dino, R., & Santana Musse, A. P. (2010, January). CO2 enhanced oil recovery and geologic storage: an overview with technology assessment based on patents and articles. In SPE International Conference on Health, Safety and Environment in Oil and Gas Exploration and Production. Society of Petroleum Engineers.

Rutqvist, J., Wu, Y. S., Tsang, C. F., & Bodvarsson, G. (2002). A modeling approach for analysis of coupled multiphase fluid flow, heat transfer, and deformation in fractured porous rock. International Journal of Rock Mechanics and Mining Sciences, 39(4), 429-442.

Rutqvist, J., & Tsang, C. F. (2002). A study of caprock hydromechanical changes associated with CO2-injection into a brine formation. Environmental Geology, 42(2-3), 296-305.

Rutqvist, J., Barr, D., Birkholzer, J. T., Chijimatsu, M., Kolditz, O., Liu, Q., ... & Zhang, C. (2008). Results from an international simulation study on coupled thermal, hydrological, and mechanical processes near geological nuclear waste repositories. Nuclear Technology, 163(1), 101-109.

Seo, J. G., & Mamora, D. D. (2005). Experimental and simulation studies of sequestration of supercritical carbon dioxide in depleted gas reservoirs. Journal of energy resources technology, 127(1), 1-6.

Shampine, L. F., & Reichelt, M. W. (1997). The matlab ode suite. SIAM Journal on Scientific Computing, 18, 1-22.

Singh, A. K., Goerke, U. J., & Kolditz, O. (2011). Numerical simulation of non-isothermal compositional gas flow: application to carbon dioxide injection into gas reservoirs. Energy, 36(5), 3446-3458.

Singh, A. K., Baumann, G., Henninges, J., Gorke, U. J., & Kolditz, O. (2012). Numerical analysis of thermal effects during carbon dioxide injection with enhanced gas recovery: a theoretical case study for the Altmark gas field. Environmental Earth Sciences, 67(2), 497-509.

Slattery, J. C. (1972). Momentum, energy, and mass transfer in continua (p. 235). New York: McGraw-Hill.

Spycher, N., Pruess, K., & Ennis-King, J. (2003). CO_2-H_2O mixtures in the geological sequestration of CO_2. I. Assessment and calculation of mutual solubilities from 12 to 100^{o}C and up to 600 bar. Geochimica et Cosmochimica Acta, 67, 3015-3031.

Stevens, S. H., Kuuskraa, V. A., Gale, J., & Beecy, D. (2001). CO2 injection and sequestration in depleted oil and gas fields and deep coal seams: worldwide potential and costs. Environmental Geosciences, 8(3), 200-209.

Stroud, K. A., & Booth, D. J. (2007). Engineering Mathematics, Sixth Edition. Palgrave Macmillan.

Sweatman, R. E., Crookshank, S., & Edman, S. (2011, January). Outlook and technologies for offshore CO2 EOR/CCS projects. In Offshore Technology Conference. Offshore Technology Conference.

Taggart, I. J. (2010). Extraction of dissolved methane in brines by CO_2 injection: implication for CO_2 sequestration. SPE Reservoir Evaluation & Engineering, 13, 791-804.

Taron, J., Elsworth, D., & Min, K. B. (2009). Numerical simulation of thermal-hydrologic-mechanical-chemical processes in deformable, fractured porous media. International Journal of Rock Mechanics and Mining Sciences, 46(5), 842-854.

Temam, R. (2001). Navier-Stokes equations: theory and numerical analysis (Vol. 343). American Mathematical Soc..

Van der Burgt, M. J., Cantle, J., & Boutkan, V. K. (1992). Carbon dioxide disposal from coal-based IGCC's in depleted gas fields. Energy Conversion and Management, 33(5), 603-610.

Van der Meer, L. G. H., Kreft, E., Geel, C., & Hartman, J. (2005, June). K12-B a Test Site for CO2 Storage and Enhanced Gas Recovery (SPE94128). In 67th EAGE Conference & Exhibition.

Van Genuchten, M. T. (1980). A closed-form equation for predicting the hydraulic conductivity of unsaturated soils. Soil science society of America journal, 44(5), 892-898.

Vohralik, M., & Wheeler, M. F. (2013). A posteriori error estimates, stopping criteria, and adaptivity for two-phase flows. Computational Geosciences, 17, 789-812.

Wen, Z., Huang, G., & Zhan, H. (2009). A numerical solution for non-Darcian flow to a well in a confined aquifer using the power law function. Journal of Hydrology, 364(1), 99-106.

Wouwer, A. V., Saucez, P., Schiesser, W. E., & Thompson, S. (2005). A MATLAB implementation of upwind finite differences and adaptive grids in the method of lines. Journal of Computational and Applied Mathematics, 183, 245-258.

Yan, W. and Stenby, E.H., 2014. On solving the Rachford-Rice equation with higher order methods. Fluid Phase Equilibria, 363, pp.290-292.

Yan, W., Michelsen, M.L. and Stenby, E.H., 2014. Negative Flash for Calculating the Intersecting Key Tielines in Multicomponent Gas Injection. Industrial & Engineering Chemistry Research, 53(36), pp.14094-14112.

Zangeneh, H., Jamshidi, S., & Soltanieh, M. (2013). Coupled optimization of enhanced gas recovery and carbon dioxide sequestration in natural gas reservoirs: case study in a real gas field in the south of Iran. International Journal of Greenhouse Gas Control, 17, 515-522.

Zeidouni, M., Pooladi-Darvish, M., & Keith, D. (2009). Analytical solution to evaluate salt precipitation during CO 2 injection in saline aquifers. International Journal of Greenhouse Gas Control, 3(5), 600-611.

Ziabakhsh-Ganji, Z., & Kooi, H. (2014). Sensitivity of Joule-Thomson cooling to impure CO 2 injection in depleted gas reservoirs. Applied Energy, 113, 434-451.